Report

The 5th Annual WAMIT Consortium Meeting

October 6-7, 2004

Woods Hole, Massachusetts

Agenda for 5th Annual WAMIT Meeting
Room 310, Marine Resource Center, Swope Center, Woods Hole, MA

October 6:

9:00AM: Welcome

9:20AM: "WAMIT V6.2"
C.-H. Lee, WAMIT
10:00AM: "Extension of WAMIT for linear coupling with internal tanks"
J. N. Newman, WAMIT

10:40AM: Break

11:00AM: "Evaluation of hyper-singular integrals in the higher-order method
- for fluid velocity and dipole patches"
C.-H., WAMIT
11:30AM: "Comparison of Iterative solvers – ITRCC and GMRES
for the higher-order method"
C.-H. Lee, WAMIT

12:00PM: Lunch

1:30PM: "Nonlinear local loads on a fixed structure"
P. Teigen, Statoil

2:15PM: "Visualization and Interpretation of Offshore Platform Response"
J.M. Niedzwecki, OTRC

3:00 PM: Break

3:30 PM: "Modelling problems related to the Snoehvit in-docking operation"
P. Teigen, Statoil

5:30PM: Mixer and Dinner

October 7:

9:00AM: Technical discussion

10:30AM: Break

10:50AM: Business meeting

12:00AM: Lunch

Contents

1. WAMIT V6.2

2. Extension of WAMIT for linear coupling with internal tanks

3. Evaluation of hyper-singular integrals in the higher-order method

4 Comparison of Iterative methods – ITRCC and GMRES.

5 Current Participants

6 Appendices

Second-order diffraction in short waves – J. N. Newman
Wave effects on vessels with internal tanks –J. N. Newman
Progress in wave load computations on offshore structures – J. N. Newman
Note on the geometry of projection – C.-H. Lee

WAMIT V6.2

Recent updates

- Internal tanks with free surfaces can be analyzed either separately or coupled with the dynamics of vessels.
- Arbitrary tank shape
- Variable fluid density in the tanks

Mean drift forces on the rigid bodies can be evaluated in the presence of other bodies with generalized modes.

This update allows to calculate mean forces on each ship with the lid in-between which is used to damp excessive resonance.

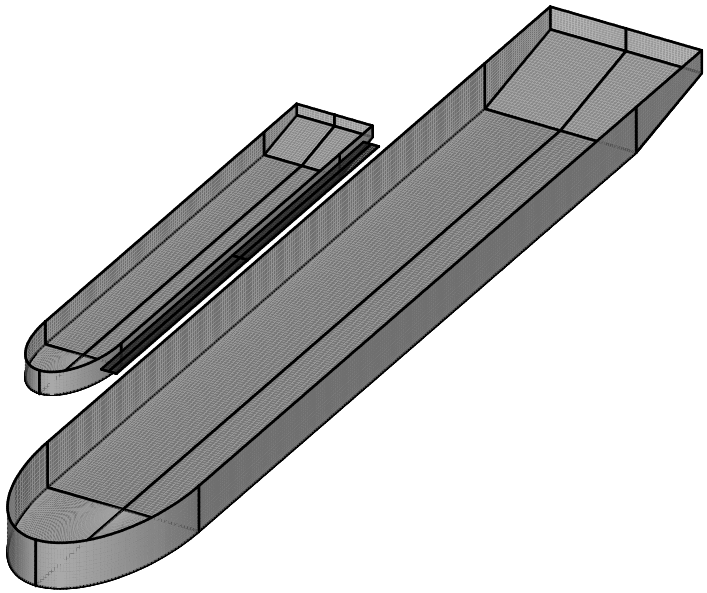

- The domain of u and v parameters for B-Splines representing the body surface is no longer limited to (-1,1). B-Splines defined over arbitrary domain can be accepted.

  Note: Subroutines in GEOMXACT keeps the same convention and u and v should be in (-1,1).

- A new output file wamitlog.txt is created during the WAMIT run to provide an archival record of the run, including copies of the principal input files, and various auxiliary information.

1) All contents of input files, except geometry files (first 10 lines of each GDF are recorded).

2) Geometric Information of the field and source points when subdivision exceeds MAXSQR specified in the program.

3) Dimensional body Inertia matrix for each of freely floating body (Alternative 1 format of FRC).

Earlier updates

- Impulse response functions (IRFs) in the time domain can be evaluated for the output options 1-7 using a utility program F2T. F2T is provided as a separate program along with WAMIT V6.2. F2T converts the outputs of WAMIT into IRFs using Fourier transforms.

- Zero and infinite frequencies can be specified with other frequencies when IRR >0. IRR>0 is ignored for these 2 frequencies. This update enables users to run these frequencies with other frequencies in one execution of WAMIT.

- The subroutine FGR0I1, is extended to calculate double derivatives and renamed as FGR0I2. This extension is necessary to evaluate the fluid velocity at zero and infinite frequencies when IOPTION(7)=1.

- In addition to the added mass and damping, the pressure and the fluid velocity on the body surface (Option 5) and at the field points (Options 6 and 7) can be evaluated for zero and infinite wave frequencies.

- In the higher-order method, some or all of the body surface can be defined to represent thin structures.

- The separate components of the hydrodynamic pressure and the fluid velocity at the field points due to each of the radiation modes and due to the diffraction field can be output separately. This extension is useful for post-processing when the dynamics of the body are modified.

Recent updates

- Internal tanks with free surfaces can be analyzed either separately or coupled with the dynamics of vessels.
- Arbitrary tank shape
- Variable fluid density in the tanks

Extension of WAMIT for linear coupling with internal tanks

by J. N. Newman

October 2004

OUTLINE

- Motivation: tanks have important effects on vessel motions, and vice versa)
- Previous work (Rognebakke & Faltinsen, Kim, Molin et al, Malenica et al)
- Methodology (use WAMIT for entire solution)
- Examples of applications (Molin barge, spheroid, generic FPSO, MultiSurf FPSO)
- How to use WAMIT with tanks (V62)

Modifications in WAMIT

- Input tank geometry in same manner as hull geometry (but identify it as one or more internal tanks)
- Free surface elevation of each tank and density of fluid are arbitrary
- Solve for potential with extended boundary surface, but impose conditions (a) no interactions between different domains, and (b) no diffraction solution in tanks
- Trivial changes to FORCE (e.g. density, height of free surface, etc)
- Tank effects are included in all output options (1-9)

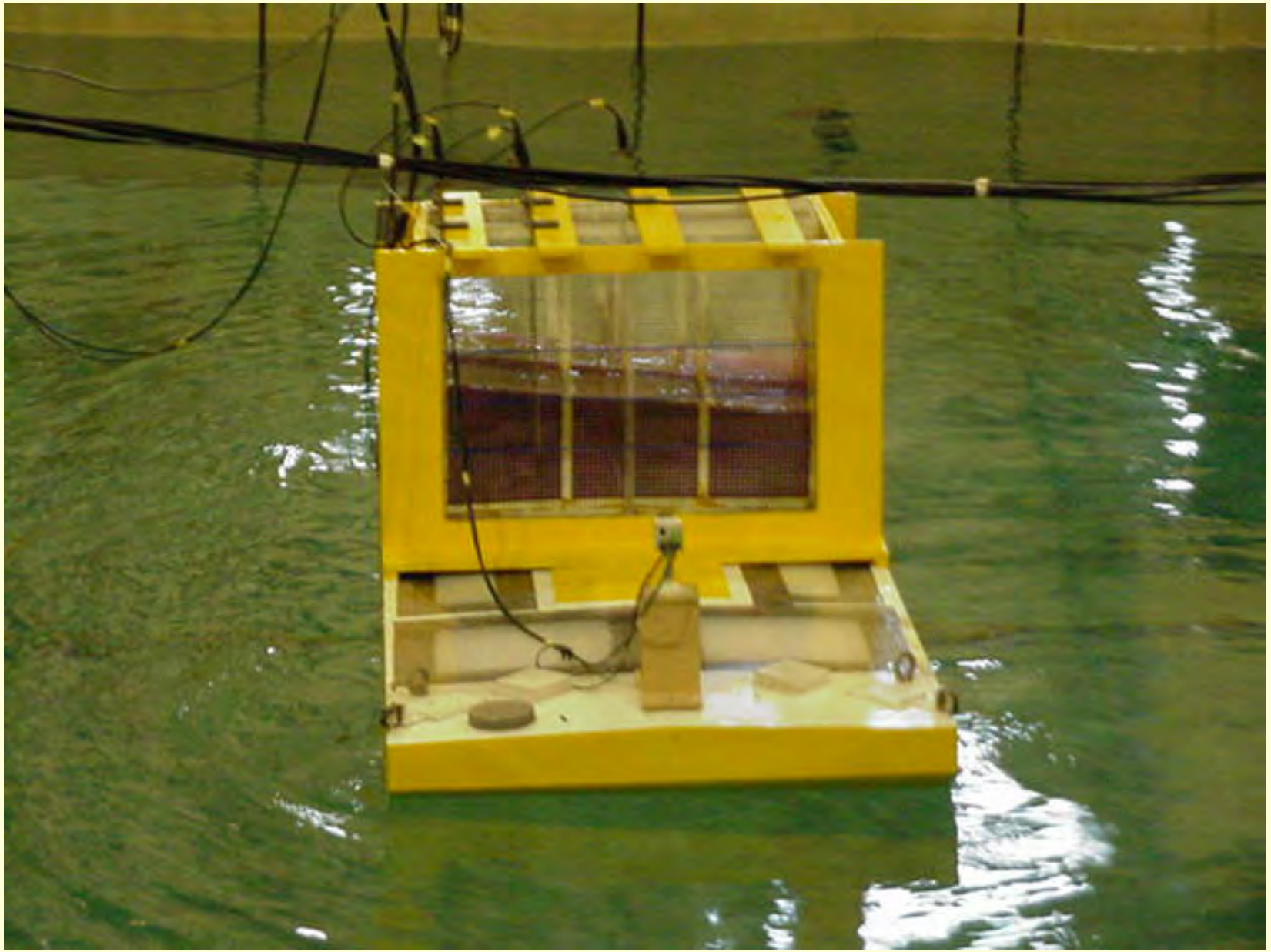

Free surface elevation in one tank near upwave wall (or two tanks, both 19cm depth)

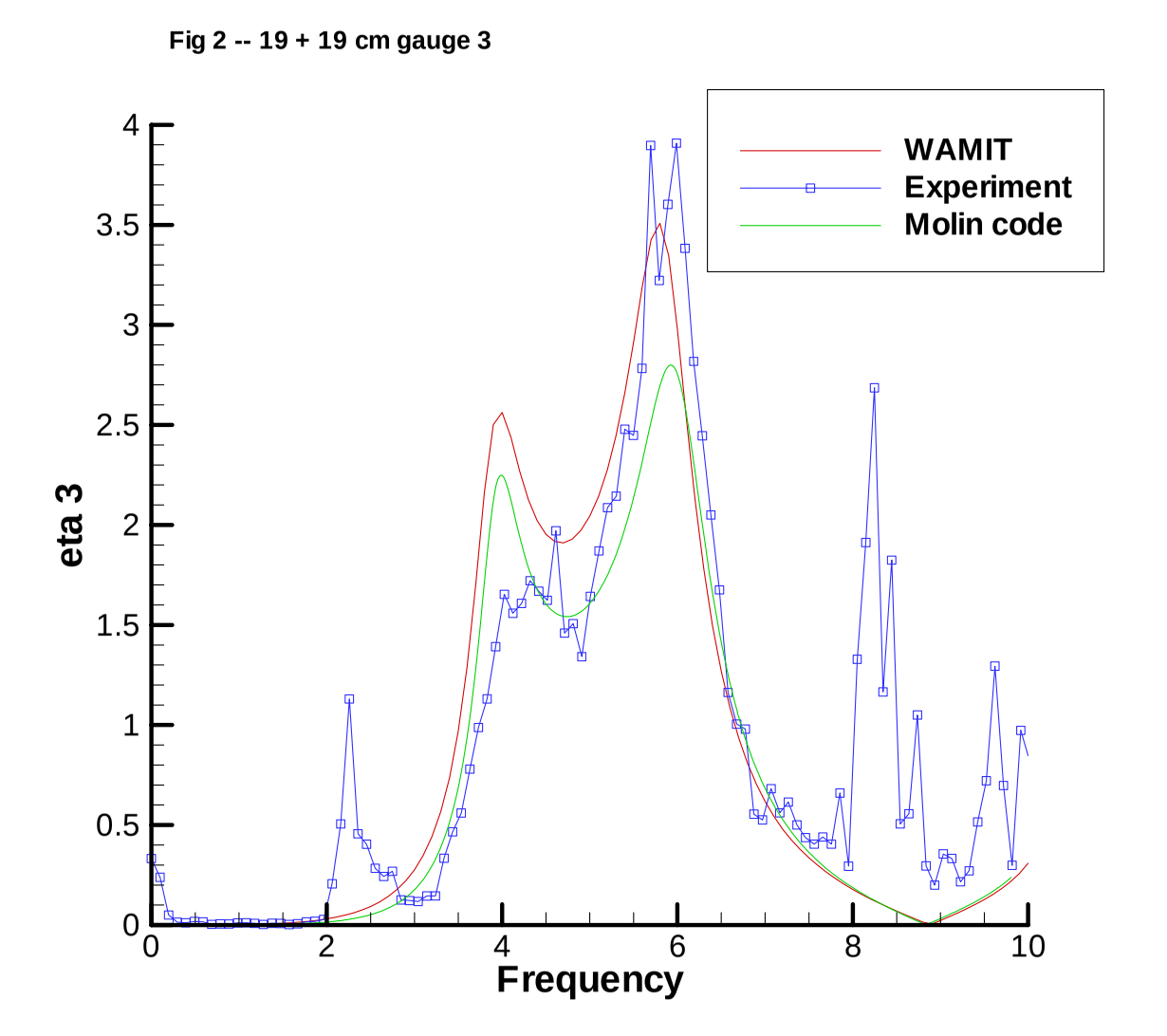

Roll RAO (beam seas)

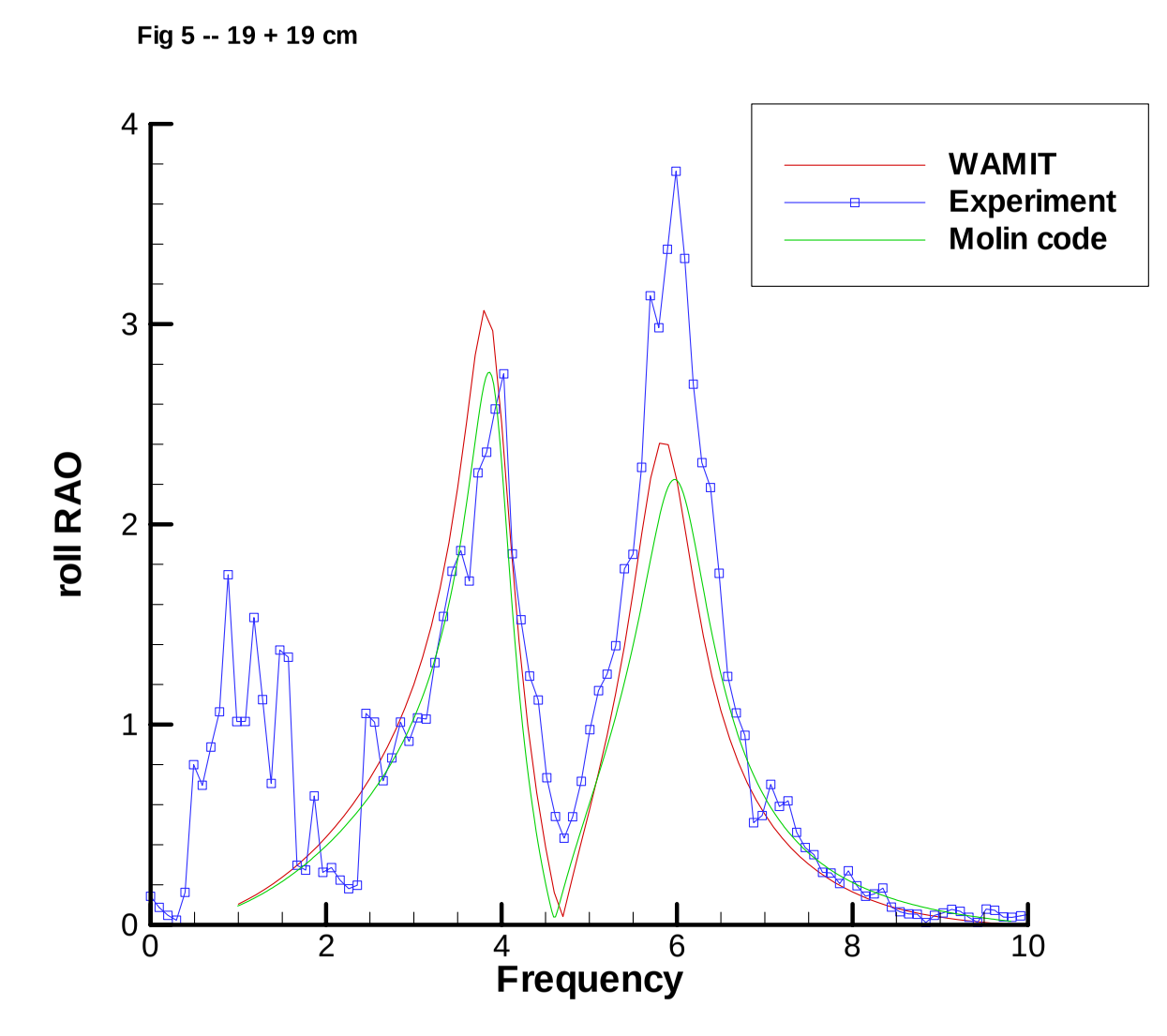

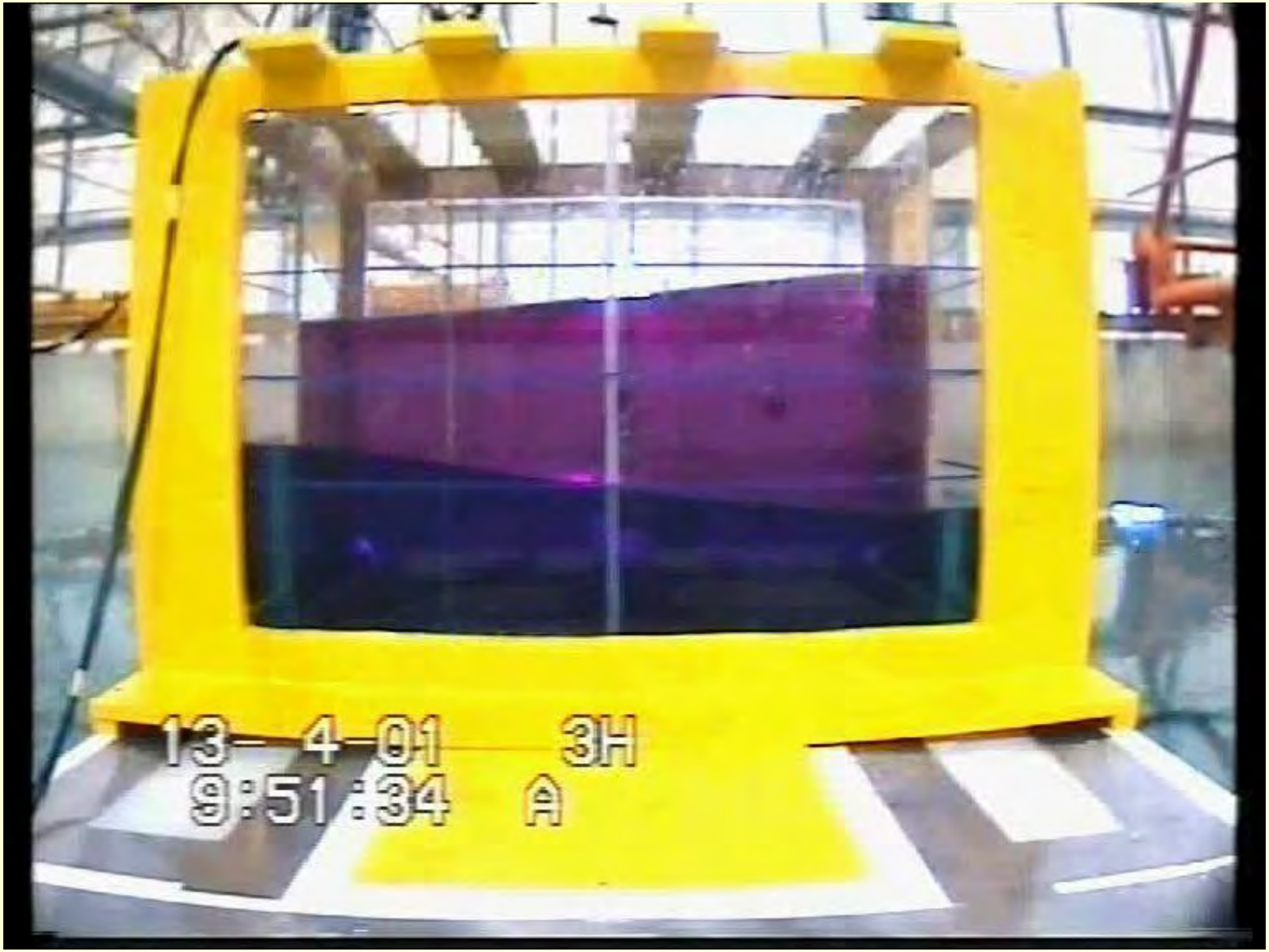
13- 4-01 3H
9:51:34 A

Free surface elevation in deeper tank near upwave wall

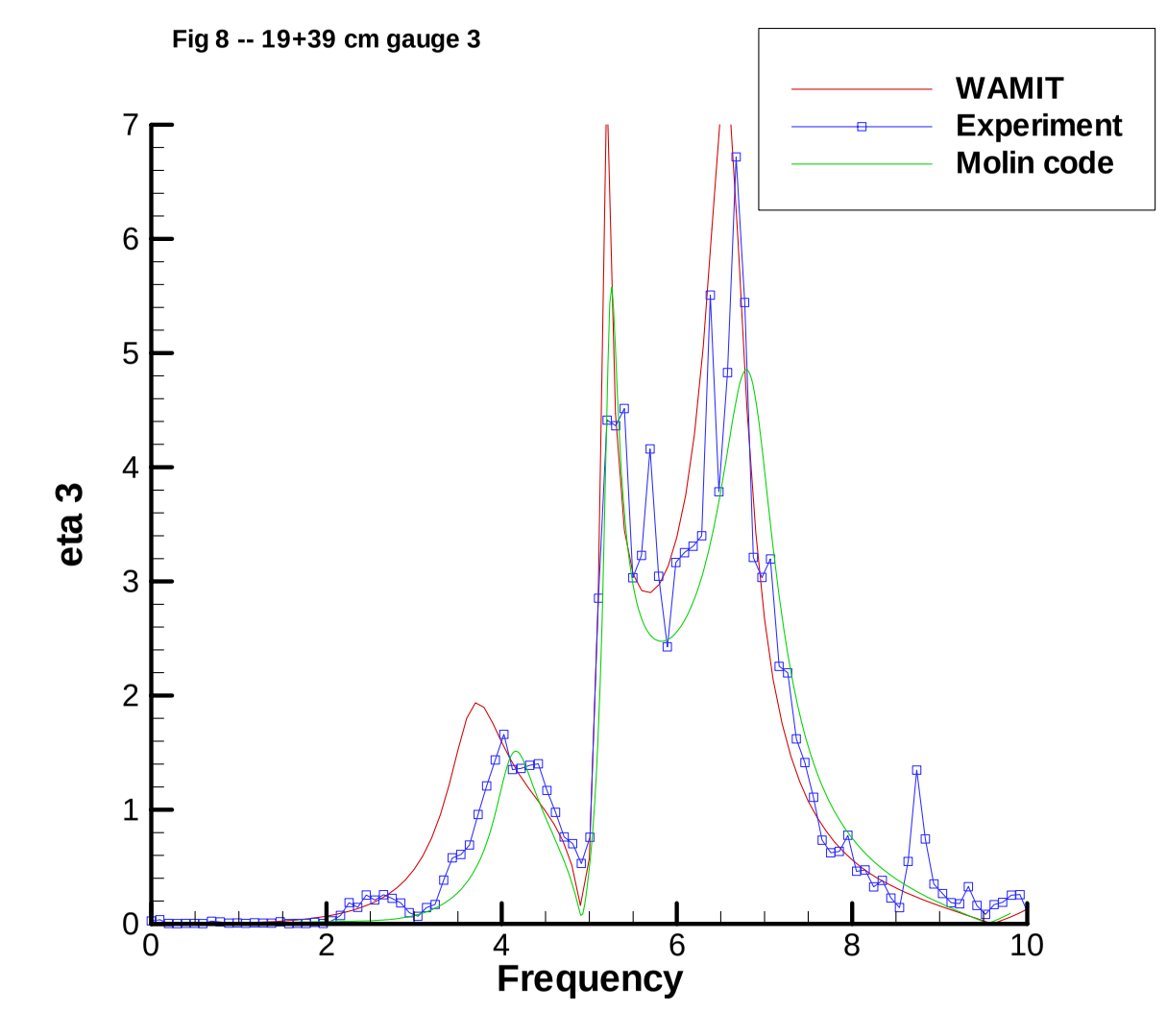

Experimental validation for a barge with two internal tanks
Barge 3m x 1m x .108m, tanks .25 x .8 x 19cm, 39cm deep
Experiments and Computations by Molin et al, IMAM 2002

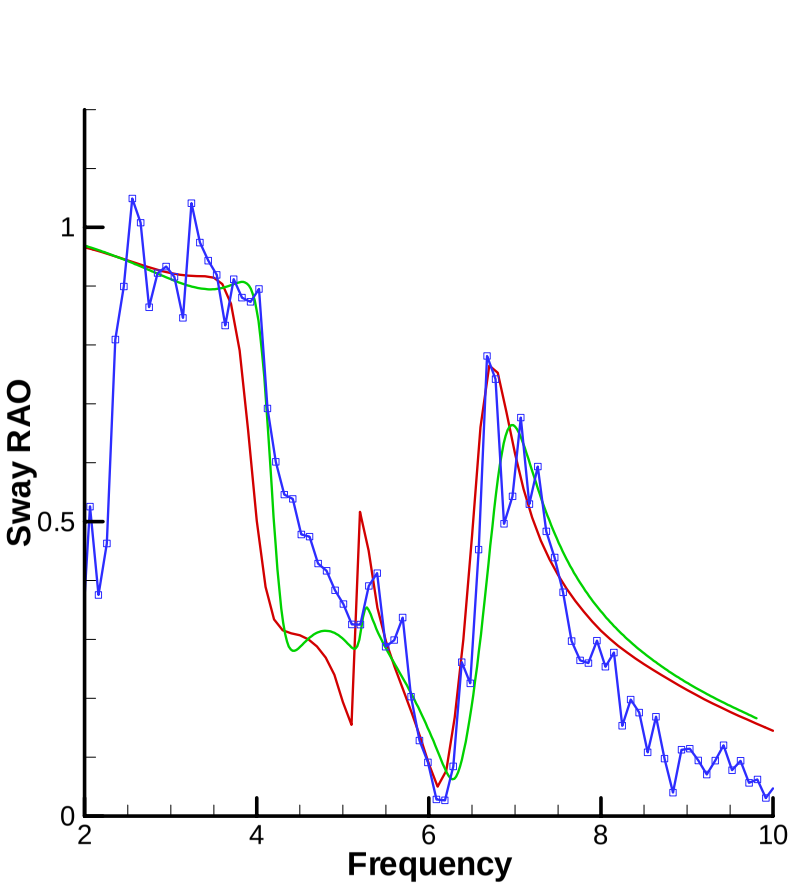

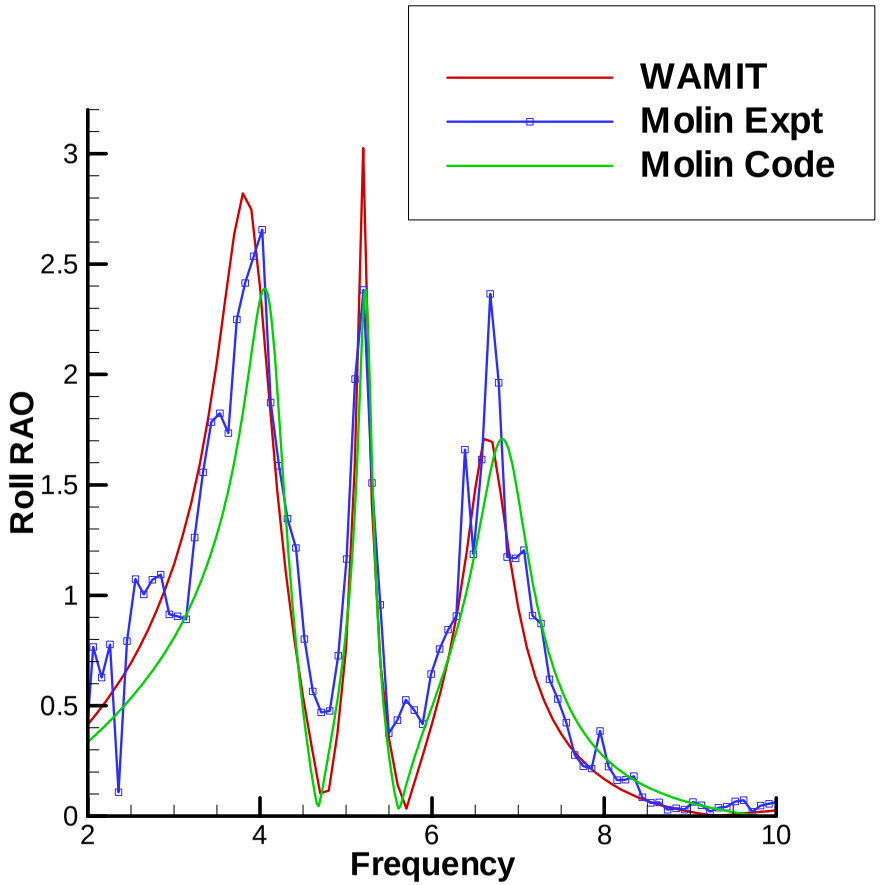

Spheroid with four tanks

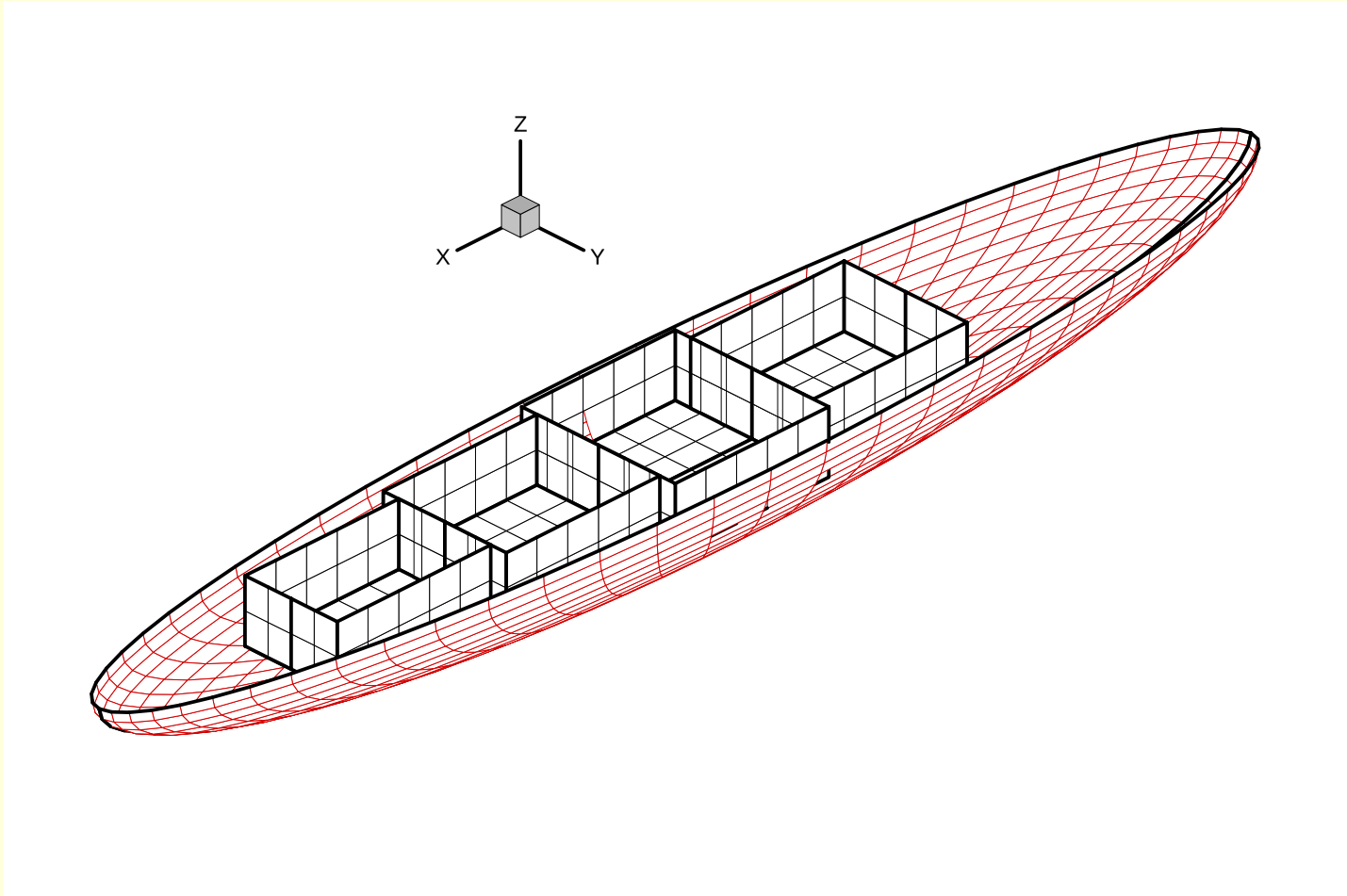

RAO's in head seas, beam seas, 135 degrees tank density= 0, .5, 1.0

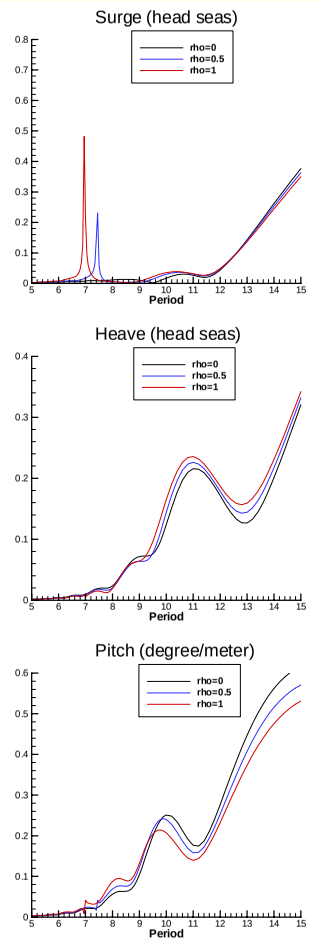

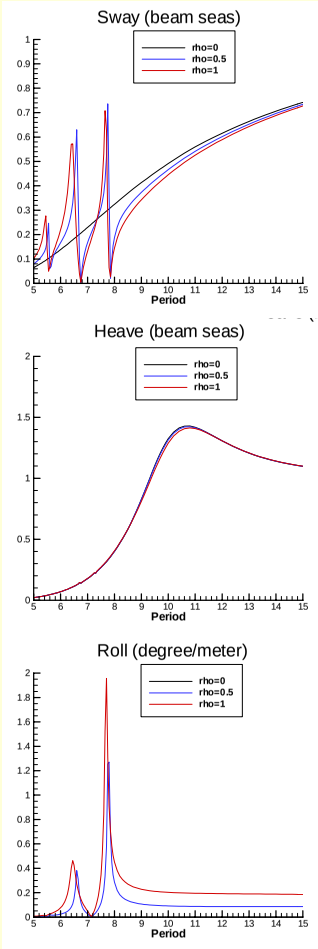

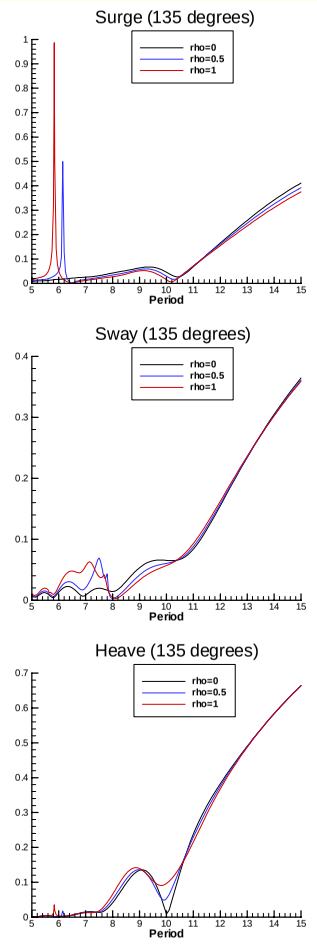

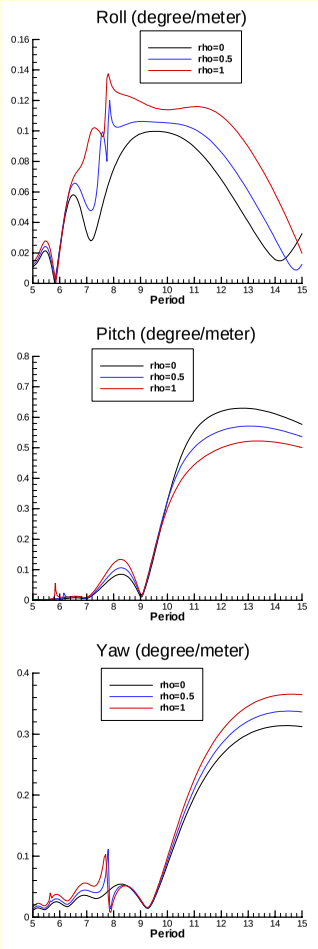

Mean drift forces (solid=momentum, dashed=pressure)

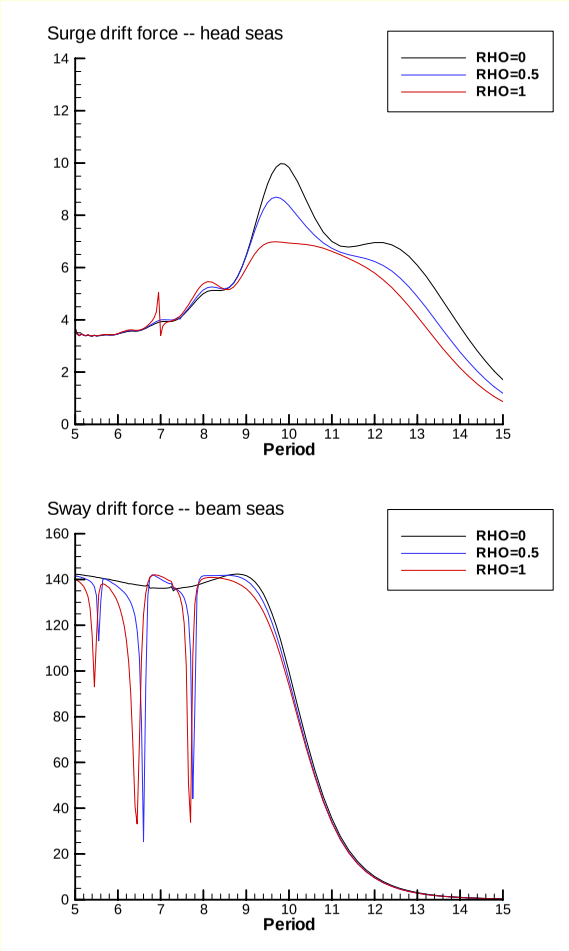

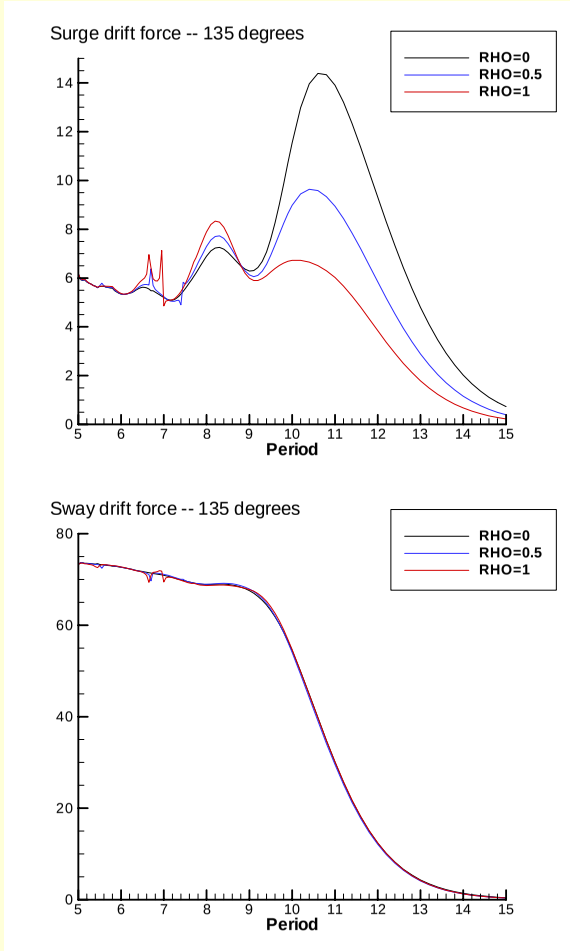

Generic FPSO (GEOMXACT) 300x50x15m
Tanks 40x40x15m, 3m above hull

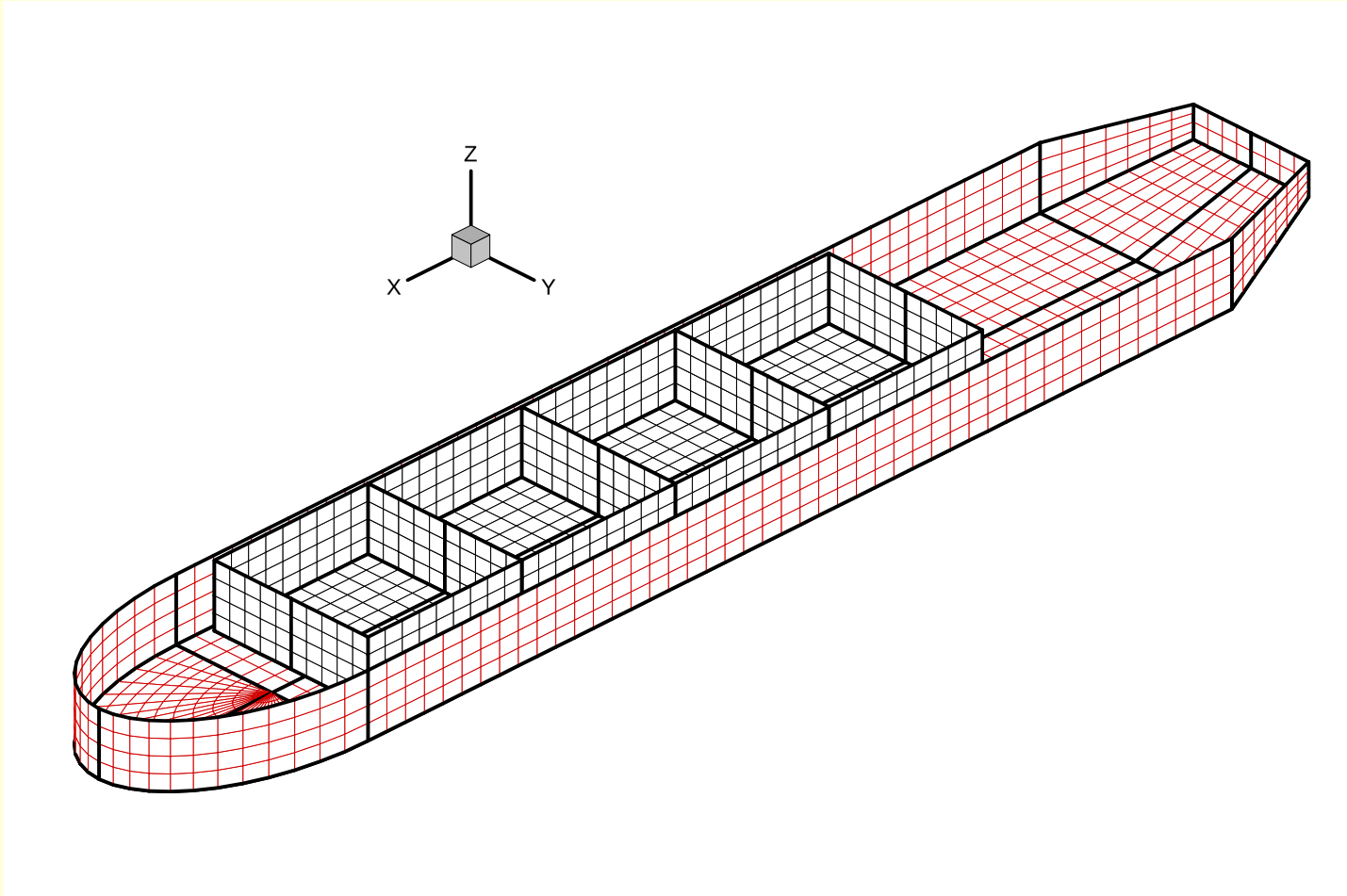

RAO’s and drift forces in head/beam waves

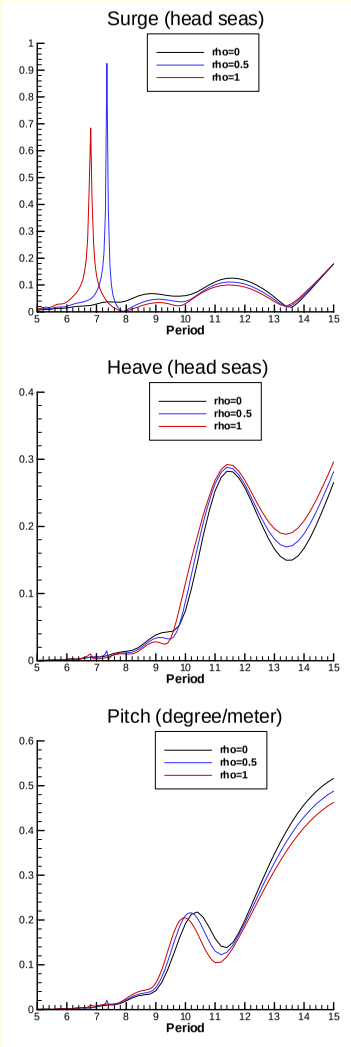

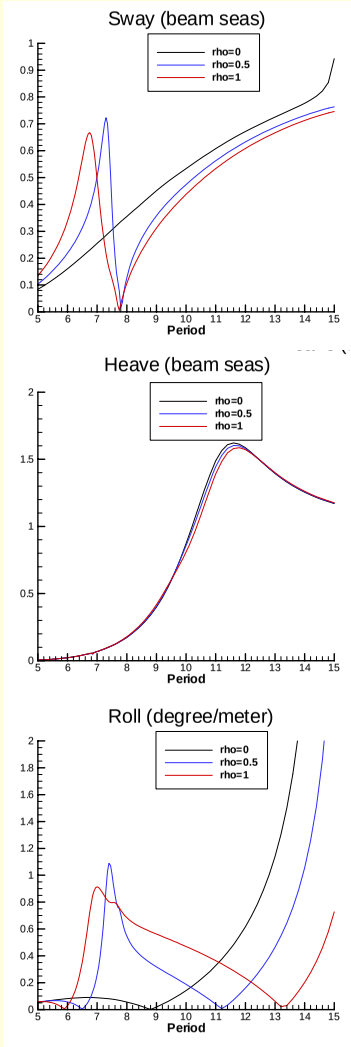

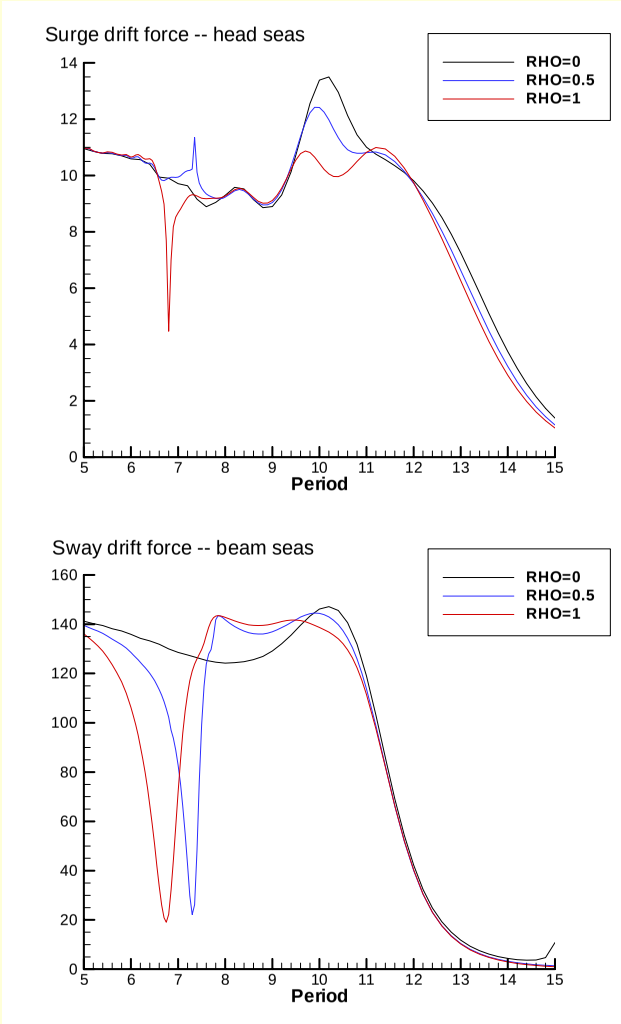

MultiSurf generated FPSO (IGDEF=2)

FPSO 300 x 50 x 15m
tanks 30 x 40 x 15m

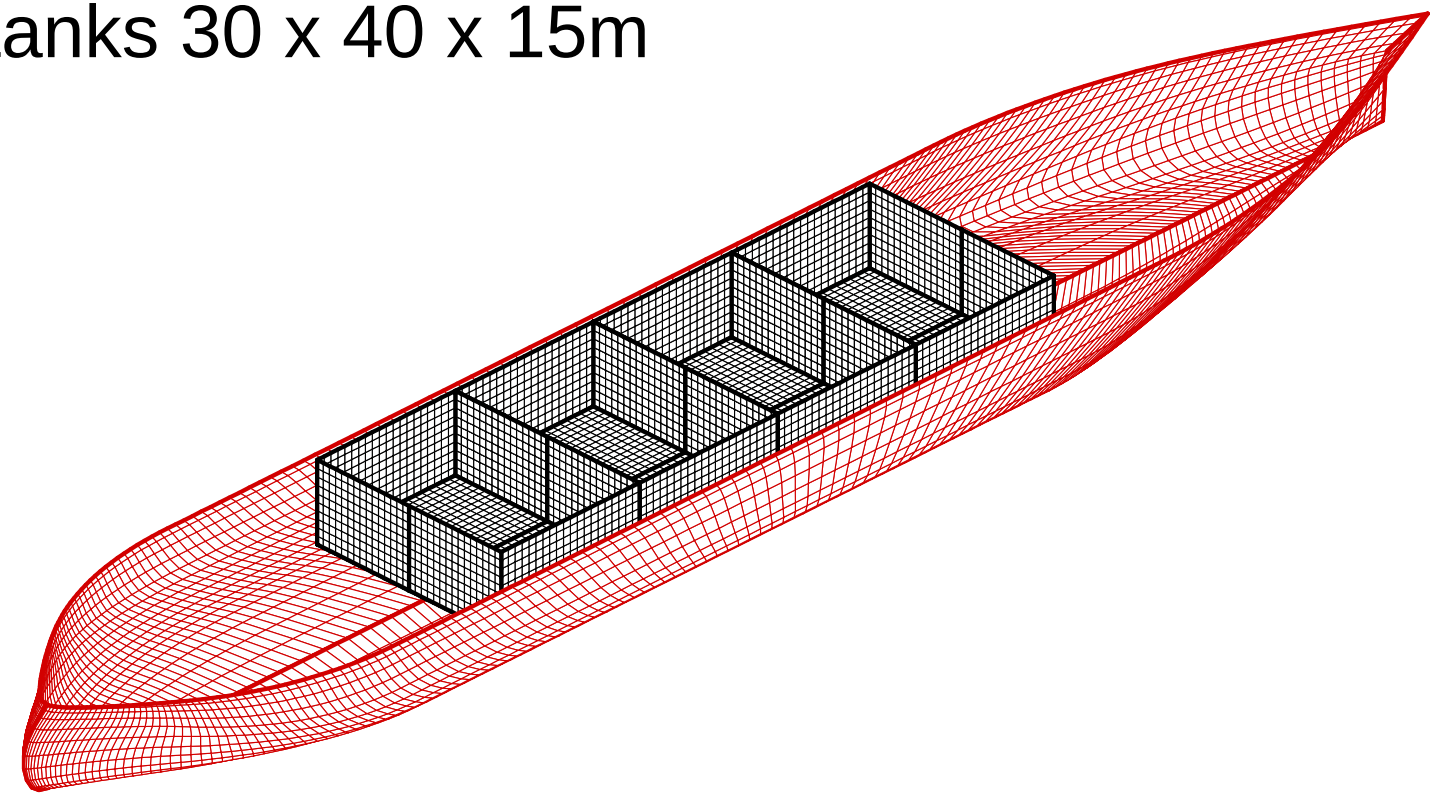

Sway/Roll RAO's in beam seas

rho = relative density of fluid in tanks

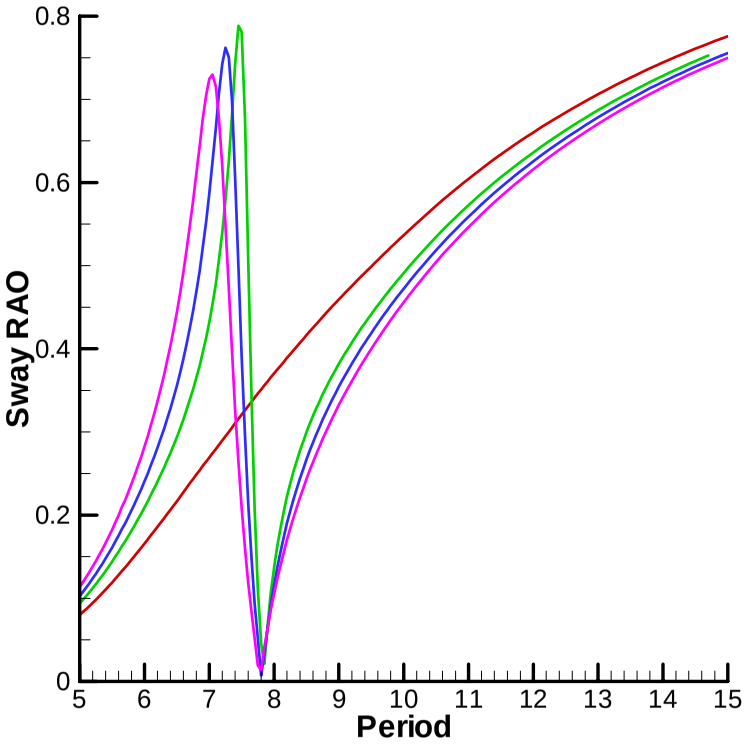

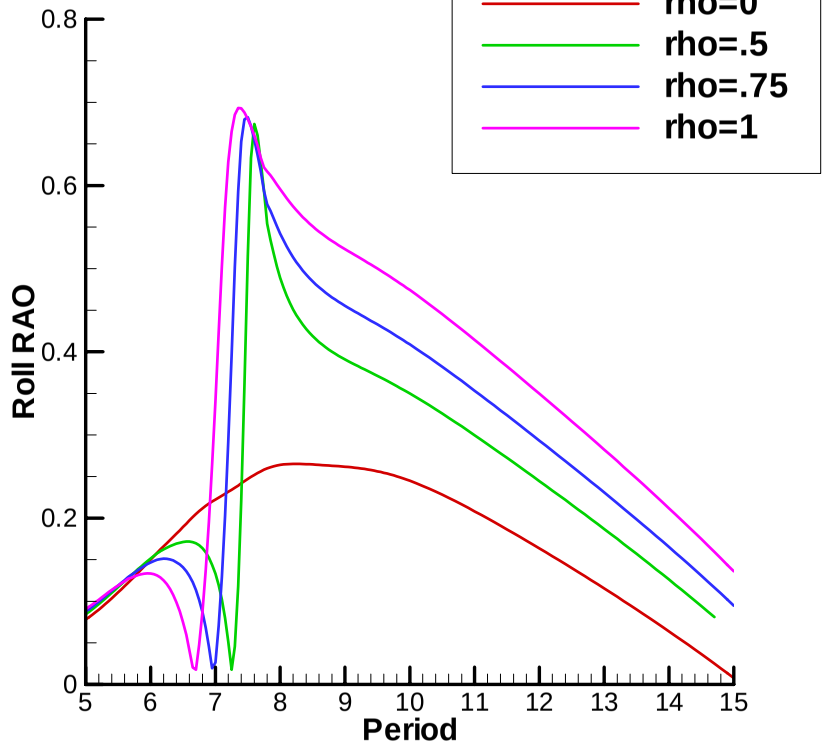

Free-surface elevation in tanks near forward corner
Solid lines: head seas – Dashed lines: beam seas
Arrows: natural periods of 1st sloshing modes in tanks

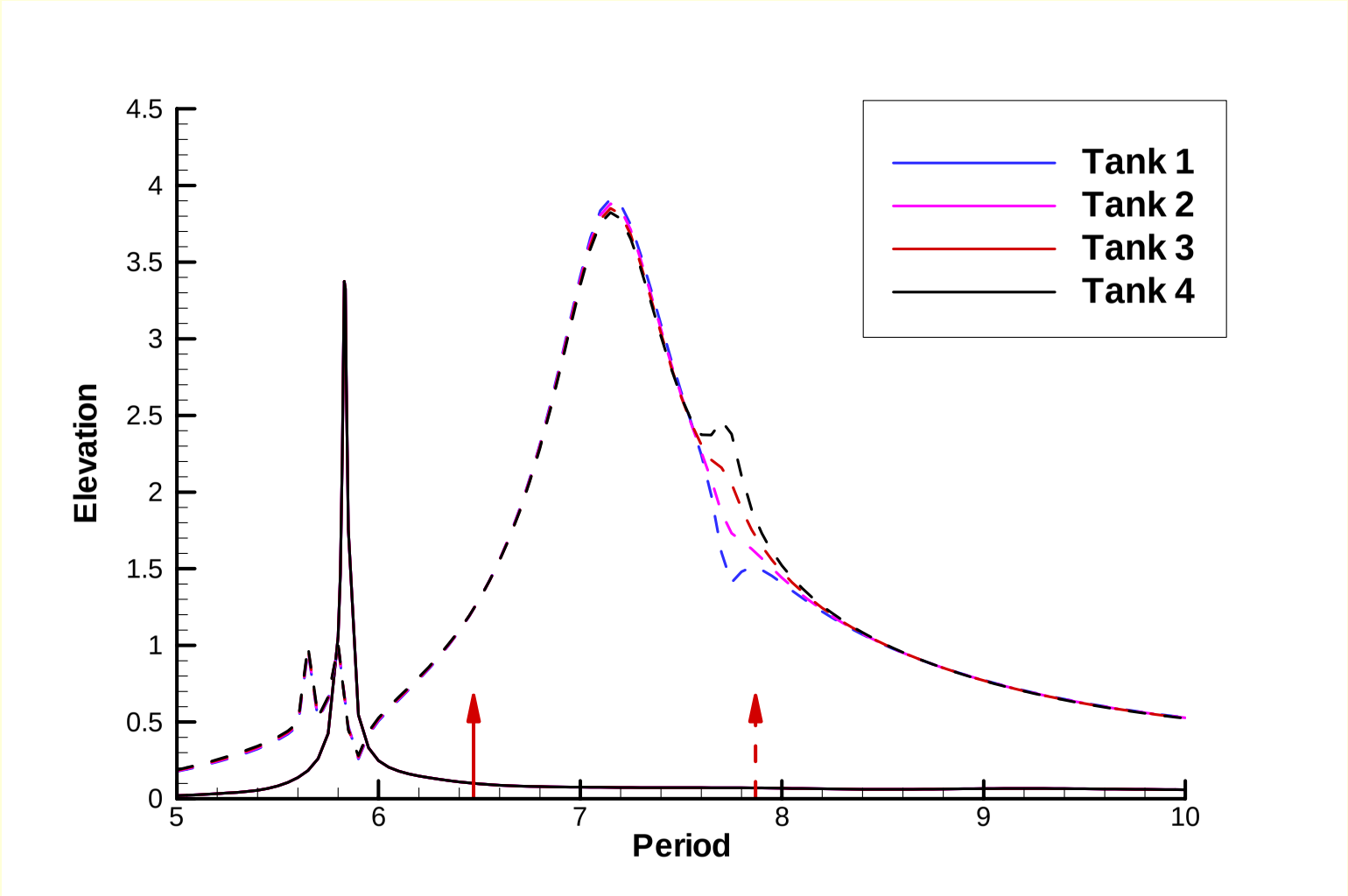

Inputs to WAMIT -- Geometry

- GDF file: the tank surfaces are represented by low order panels or by one of the higher-order methods with appropriate patches. Normal is out of the (tank) fluid domain.
- Modify GEOMXACT or MultiSurf .ms2 file to include descriptions of the tank geometry together with hull geometry.
- Tanks are reflected about planes of symmetry (!)
- The height of the tank free surface(s) are derived from the highest vertex.
- For Irregular-frequency removal the interior free surface is independent of the tanks (covers the entire domain)
- Since solutions in different domains are independent, tanks can be arbitrarily close to each other or to the hull (small or zero gaps are OK)

Tank Inputs to WAMIT – Configuration file (CFG)

- NPTANK – specifies the panel or patch indices of each tank by two integers for first and last indices
- RHOTANK – specifies the (relative) density in each tank
- ITANKFPT – specifies that the tank index is included with field point coordinates in the FRC file (required only when some or all field points are inside tanks)

Tank Inputs to WAMIT – Force control file (FRC)

- If ITANKFPT=0 is input in the CFG file (default), field point data in the FRC file is in the usual format (X, Y, Z) and all field points are assumed to be in the exterior domain
- If ITANKFPT=1 is input in the CFG file, field point data in the FRC file must be in the special format (J, X, Y, Z) where J is the tank index and J=0 corresponds to the exterior domain.
- Body mass: when IALTFRC=1 (default) the body mass is derived from the displaced volume and the mass of the tanks is subtracted. When IALTFRC=2 the body inertia matrix should be input without including the inertia of the tank fluid.

Further Information:

“Wave effects on vessels with internal tanks”
(preliminary draft -- see appendix)

Evaluation of hyper-singular integrals in the higher-order method - for fluid velocity and dipole patches.

- Dipole patches are acceptable in the higher-order method of WAMIT V6.2 to represent submerged thin elements (Test Run 21)

  On the dipole patches, the evaluation of the influence coefficients involves the hyper-singular integral - normal derivative due to the distribution of normal dipole.

- The tangential derivatives can be evaluated in the same manner. This may be used for an alternative method to calculate fluid velocity on the body.

The tangential fluid velocity on the body is calculated efficiently from analytic derivative in the higher-order method in the form

$$\nabla_{\mathbf{x}}\phi = \frac{\partial\phi(\mathbf{u})}{\partial\mathbf{u}} \cdot \frac{\partial\mathbf{u}}{\partial\mathbf{x}}$$

It is product of the derivatives of B-spline solution and mapping function.

Inside the patches, the computed velocity is very accurate.

Close to the boundary of the patches, the computed velocity can be inaccurate, when the mapping and the fluid flow are not consistent.

Examples are the use of uniform mapping toward the corner and the use of cosine spacing toward the waterline.

Finding appropriate mappings can be complicated in practice.

Alternative to the analytic derivatives the velocity is evaluated from the derivatives of the potential formulation.

$$2\pi\nabla_s\phi(\mathbf{x}) + \int\int_{S_b} \phi\nabla_s G_{n_\xi} dS_\xi = \int\int_{S_b} \phi_{n_\xi}\nabla_s G dS_\xi \qquad \text{(tangetial)}$$

$$+$$

$$4\pi\phi_n(\mathbf{x}) + \int\int_{S_b} \phi G_{n_\xi n_x} dS_\xi = 2\pi\phi_n(\mathbf{x}) + \int\int_{S_b} \phi_{n_\xi} G_{n_x} dS_\xi \qquad \text{(normal)}$$

$$||$$

$$2\pi\nabla\phi(\mathbf{x}) + \int\int_{S_b} \phi\nabla G_{n_\xi} dS_\xi = \int\int_{S_b} \phi_{n_\xi}\nabla G dS_\xi$$

As in the pervious report, the evaluation of the hyper-singular integral is made using a tangent plane at the collocation point as shown below.

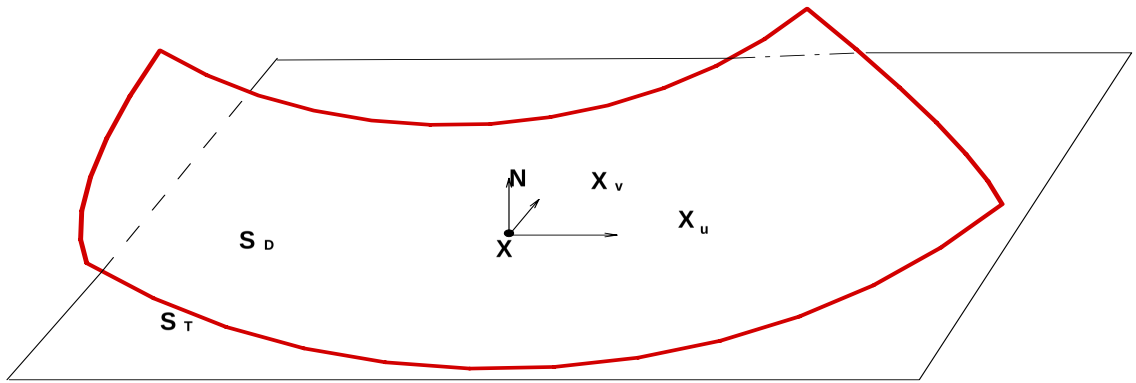

The projection of the actual body surface on the tangent plane is made. This minimizes the difference between two surfaces and results in smaller cancellation error.

The line integral on the tangent plane along the projection of the panel boundary is carried out by successive subdivision.

The geometric parameters necessary for the numerical quadrature on the tangent plane are listed in the note.

Computational example

- Surge mean drift force on a freely floating cylinder , R=1 and T=0.5.
- A) 4 different levels of panel subdivisions from 2 x1 (NEQN=24) to 16x8 (360) on each of two patches on a quadrant
- B) 4 levels from 2 x 1 on the side and 2 x 2 on the bottom (28) to 16 x 8 and 16 x 16 (504)

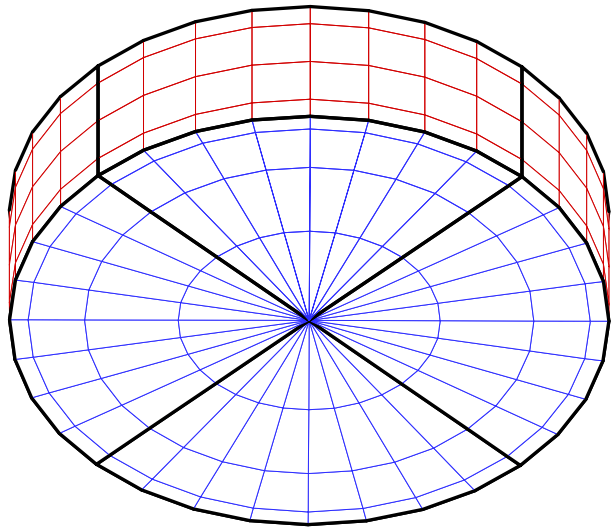

It shows the subdivision 8 x 4 of A

A) Discretization

Triangle : V6.1 (Analytic derivative) with uniform spacing

Rectangle: Present method with uniform spacing

Circle: V6.1 (Analytic derivative) with non-uniform spacing

N: Present method with non-uniform spacing

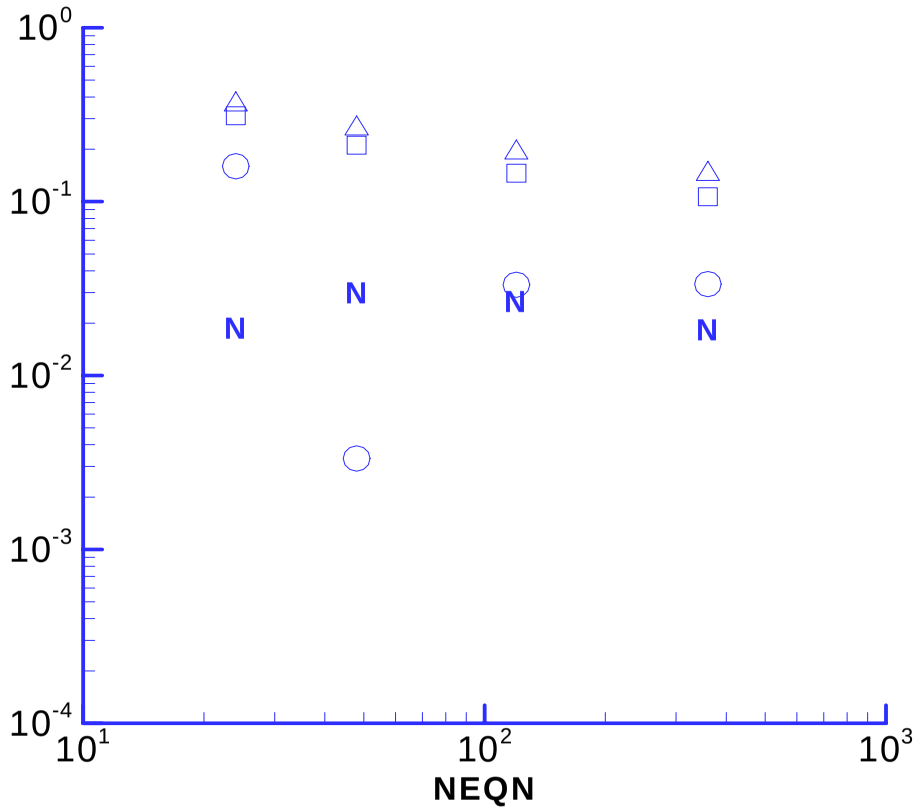

B) Discretization

Triangles : V6.1 (Analytic derivative) with uniform spacing

Rectangles: From hyper-singular integral with uniform spacing

Circle: V6.1 (Analytic derivative) with non-uniform spacing

N: From hyper-singular integral with non-uniform spacing

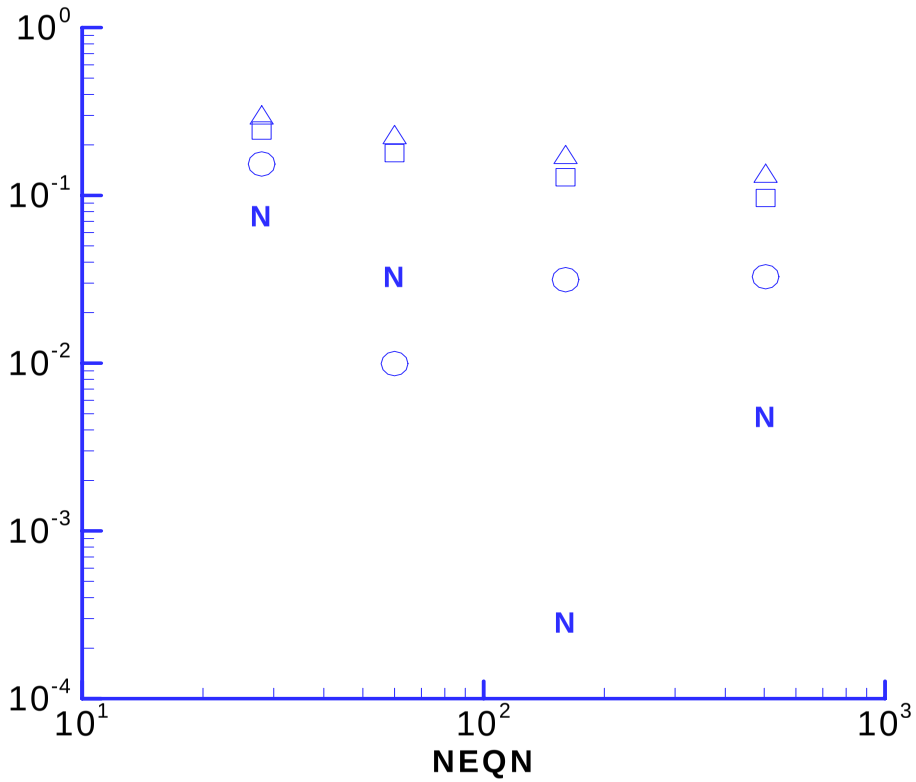

A) + B)

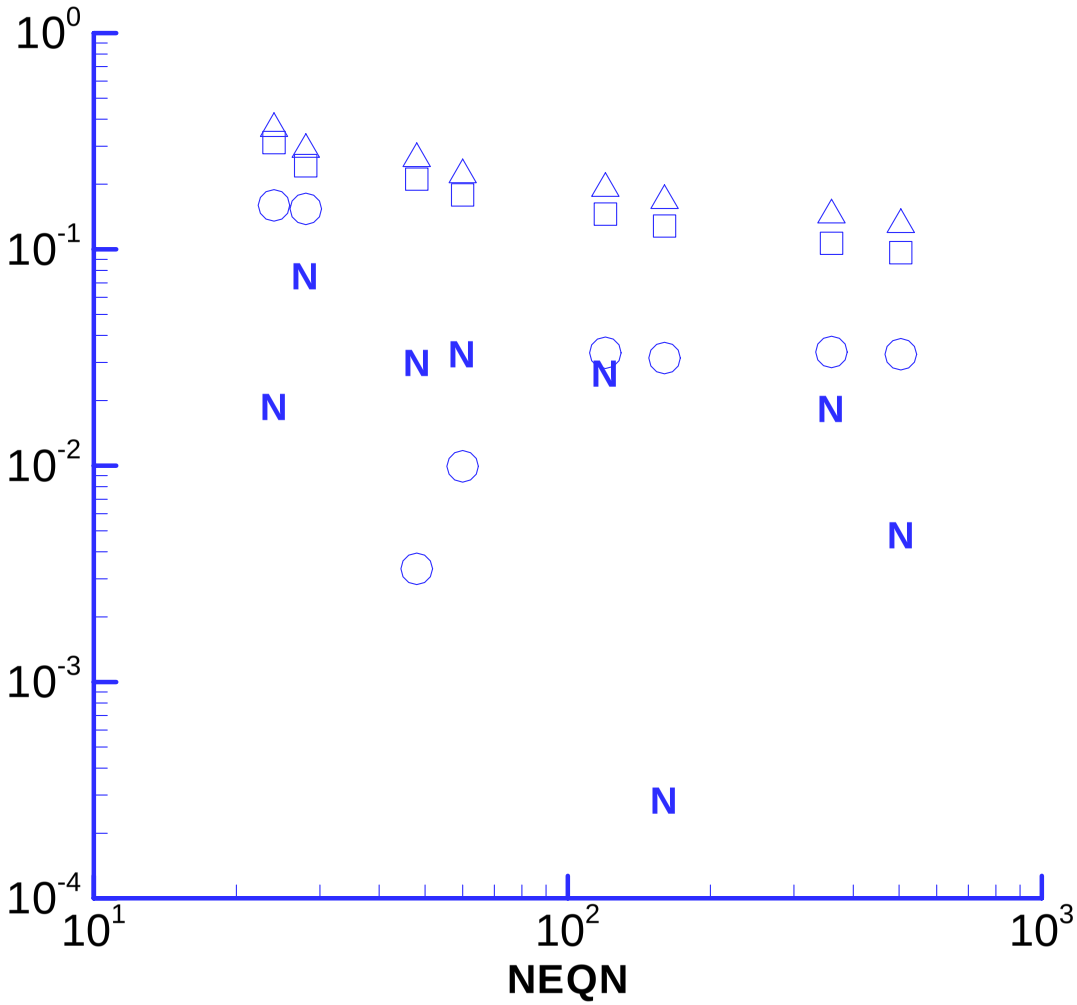

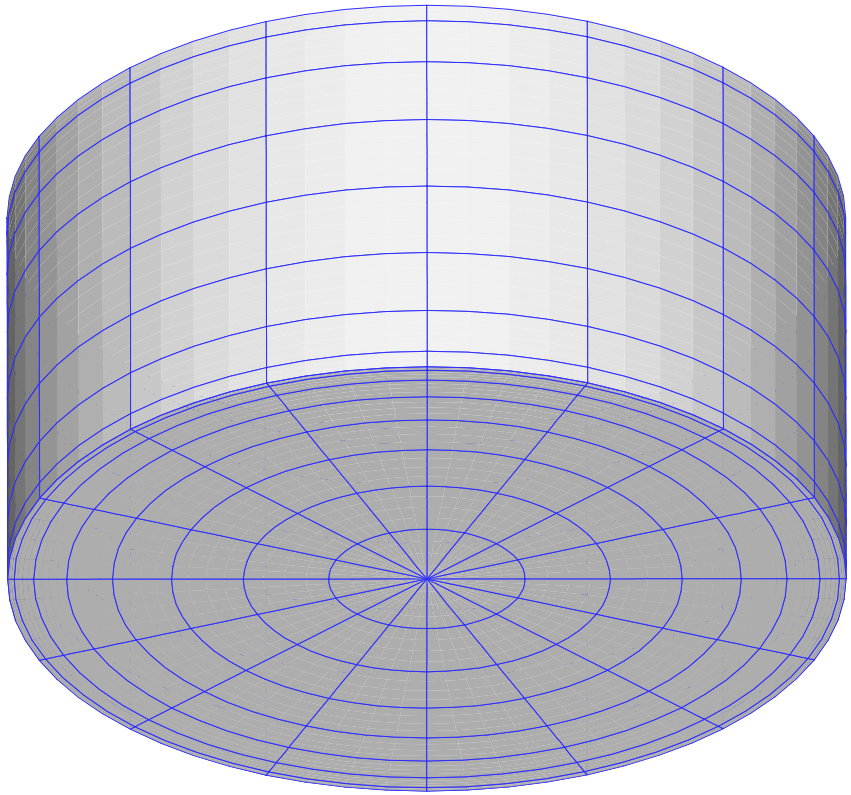

R=1, T=1

panel	unknowns
2 x 4	48
3 x 6	80
4 x 8	120
6 x 12	224
8 x 16	320

Surge mean drift force

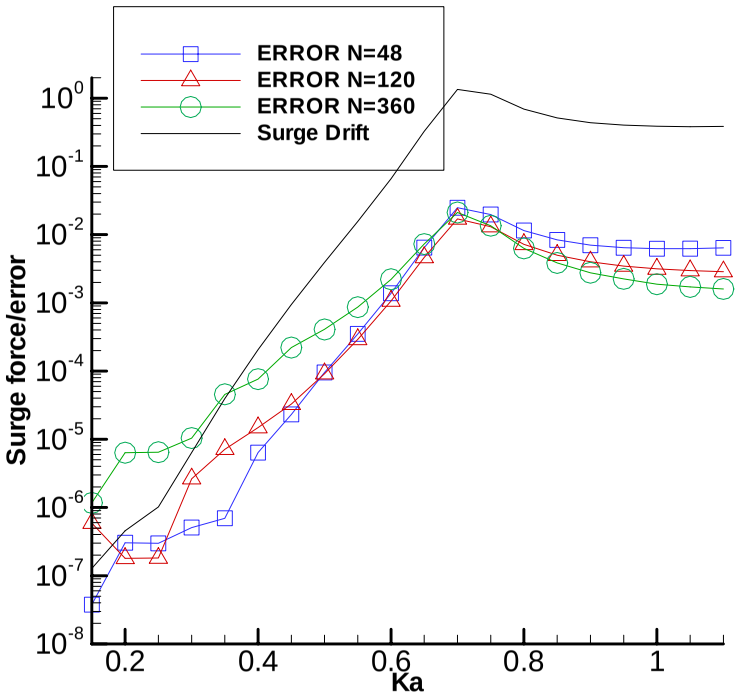

Present method

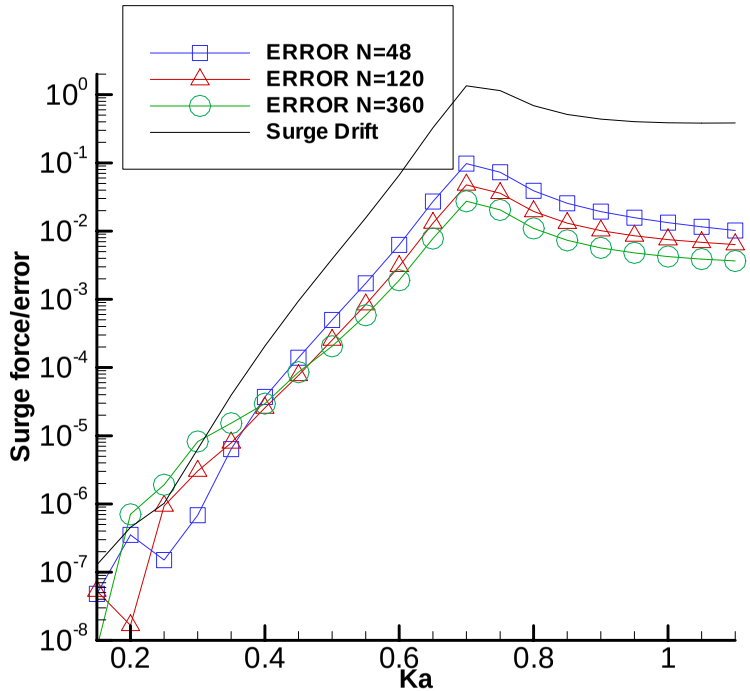

Analytic derivative

Heave mean drift force

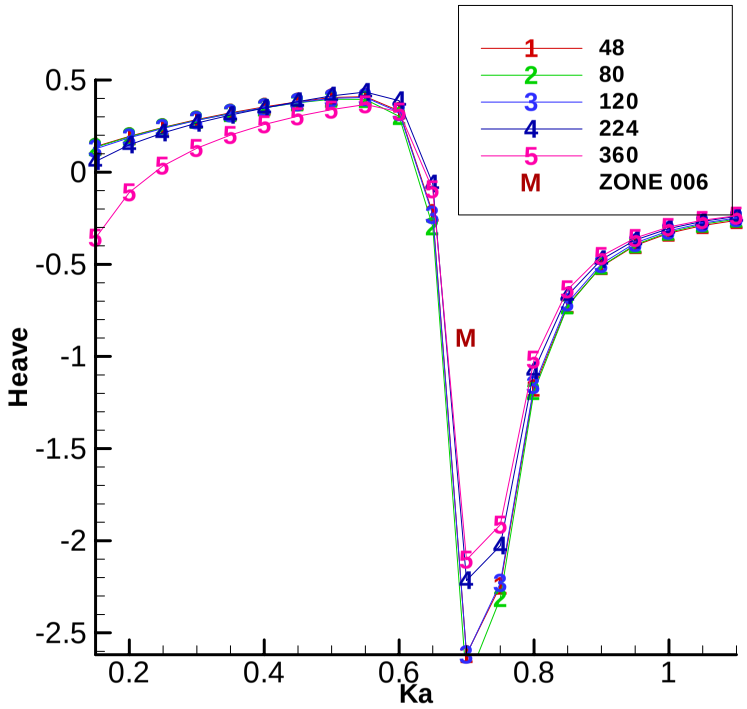

Present method

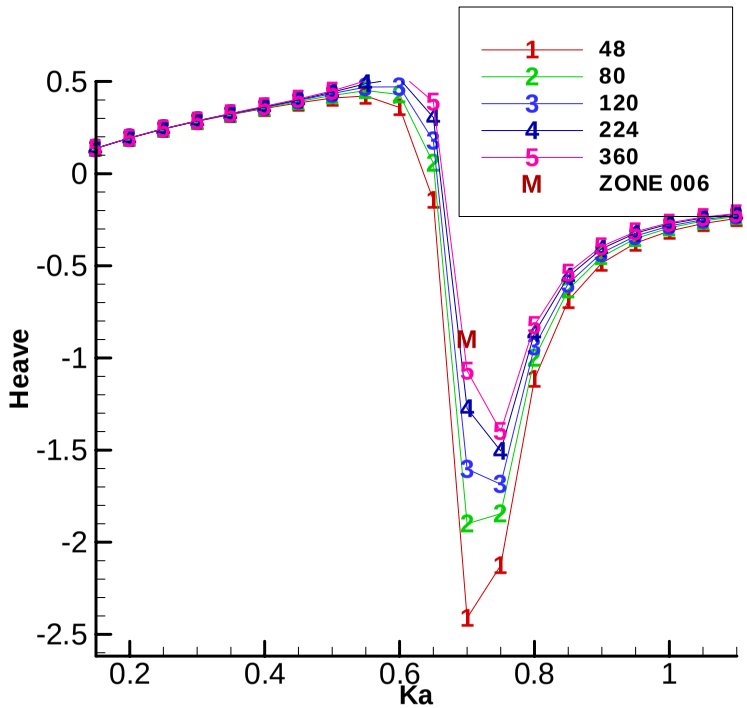

Analytic derivative

M by momentum conservation

Summary

- A method evaluating hyper-singular integral is extended for non-uniform mapping for dipole patches
- The fluid velocity is calculated using the same method. The mean force on cylinders indicates the fluid velocity calculated this way is close to the analytic derivatives.
- This method can be used for the points near the boundary of patches.

Comparison of Iterative methods – ITRCC and GMRES - for the linear systems in the higher-order method

a) Experience indicates the higher-order method is slowly convergent than the low-order. The diagonal dominance is lost when the over-determined system is converted into square system. (By **Galerkin method** or **Normal equation**). How slow?

b) Comparison: **GMRES** which is considered as a standard iterative method and WAMIT subroutine **ITRCC** which is based on accelerated Gauss-Seidel method

- 4 different cases

1. ITRCC for low-order
2. ITRCC for higher-order (Galerkin)
3. GMRES for higher-order (Galerkin)
4. GMRES for higher-order (Normal Equation)

1) Cylinder in Test 11, 2) TLP in Test 14A, 3) Spa in Test 17 and 4) arrays of 20 cylinders, 100 cylinders and a 3 x 100 cylinders are used to check convergence of the iterative methods

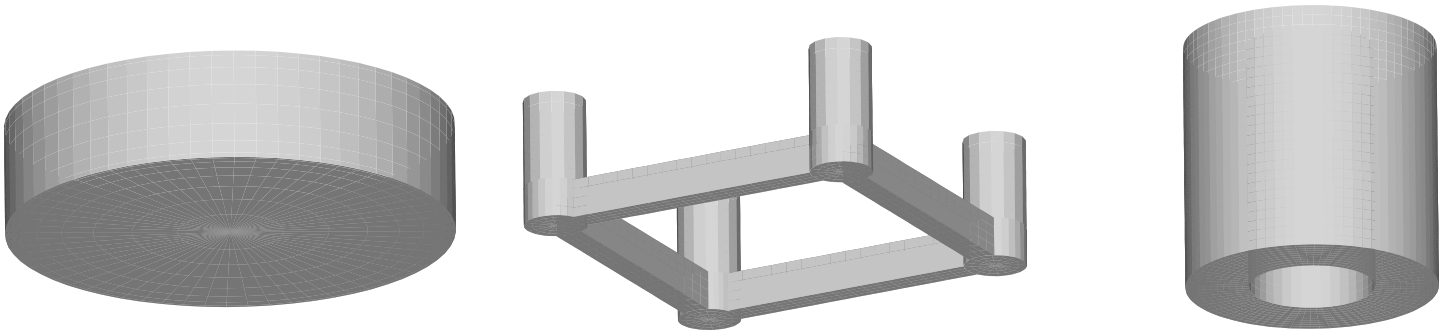

Left figure: diffraction solution symmetric in x and y. (heave force)
Right figure: diffraction solution anti-symmetric in x(surge force)

Cylinder for infinite depth wave number Ka=1.

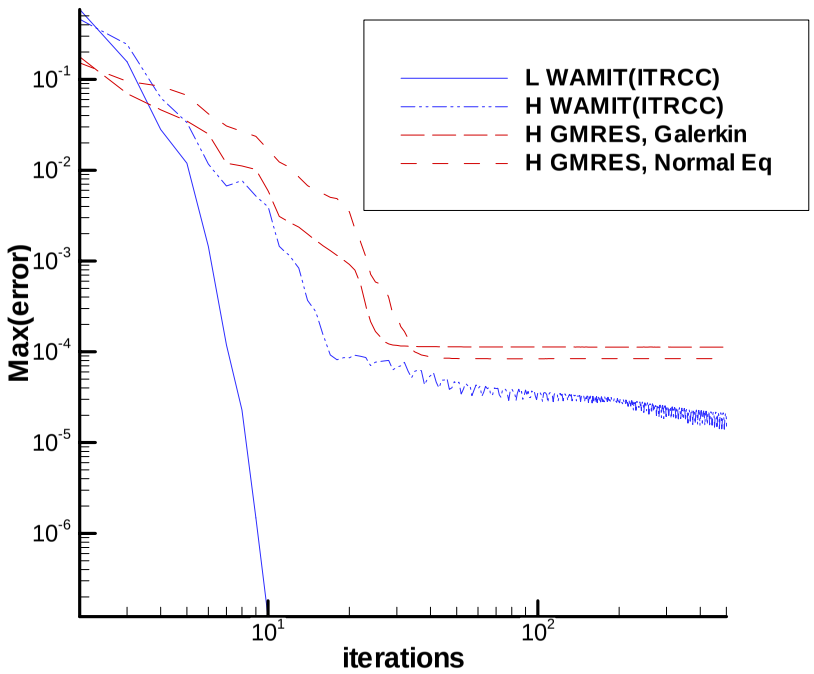

Heave

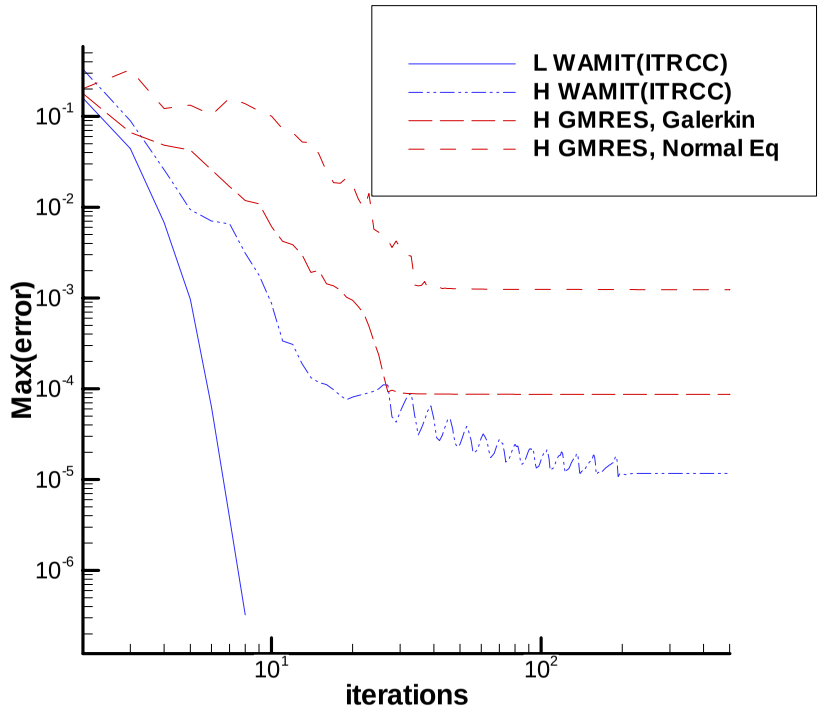

Surge

TLP for period = 3.14 sec

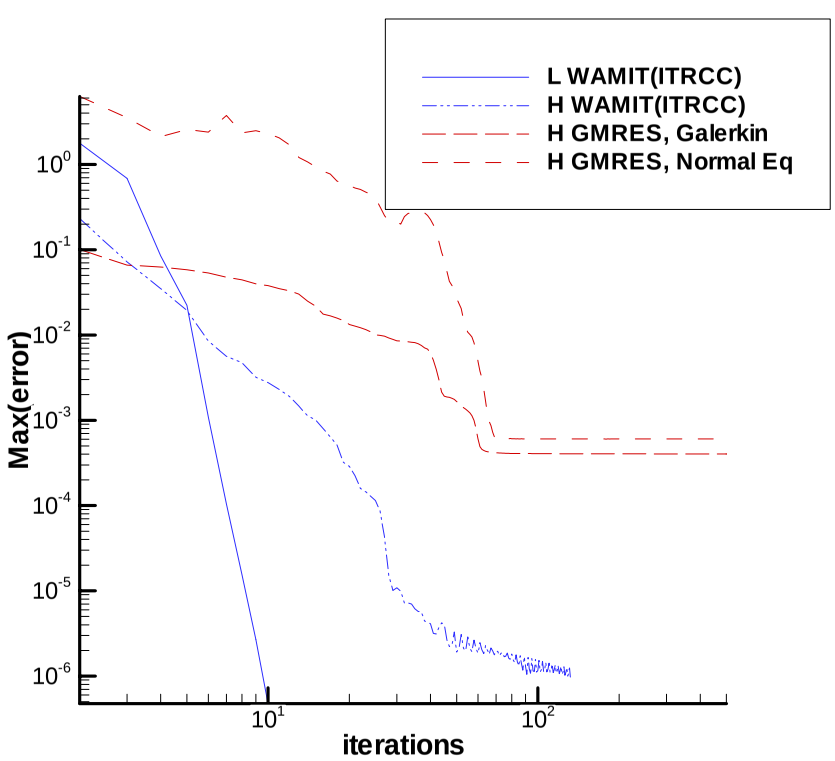

Heave

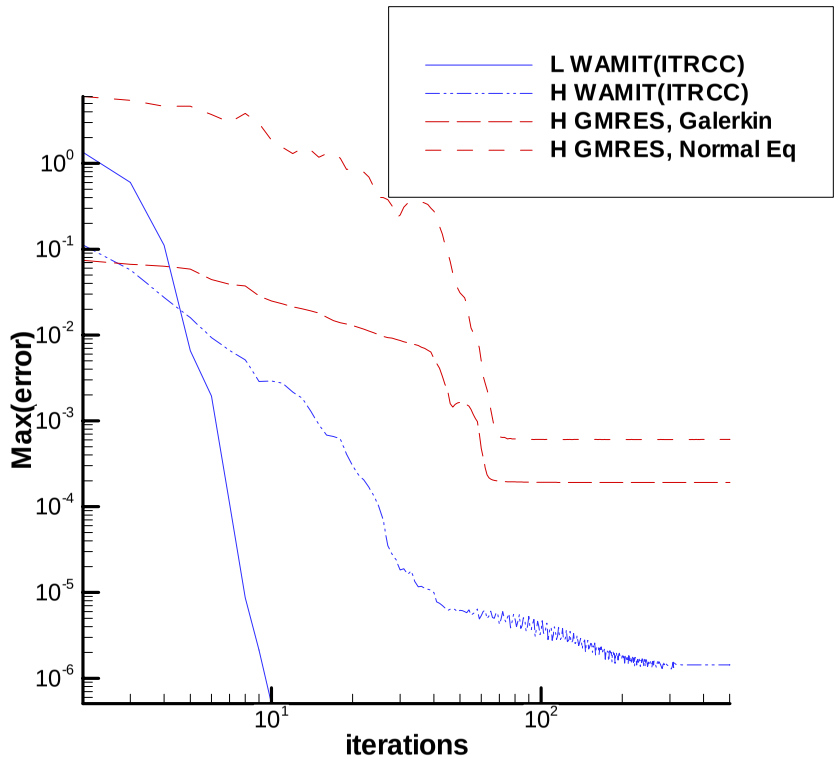

Surge

Spar for moonpool resonance

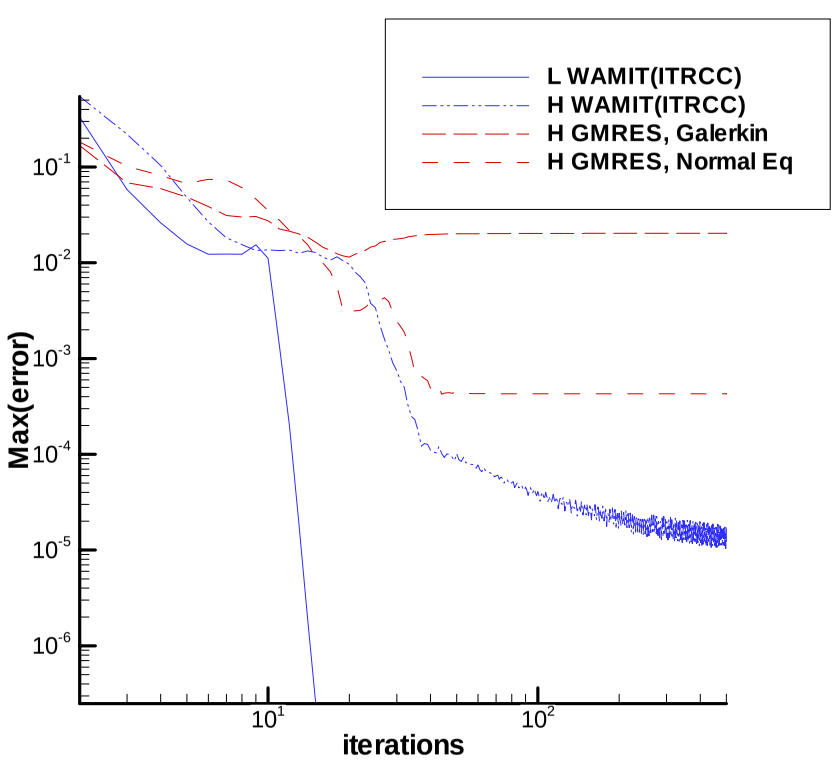

Heave

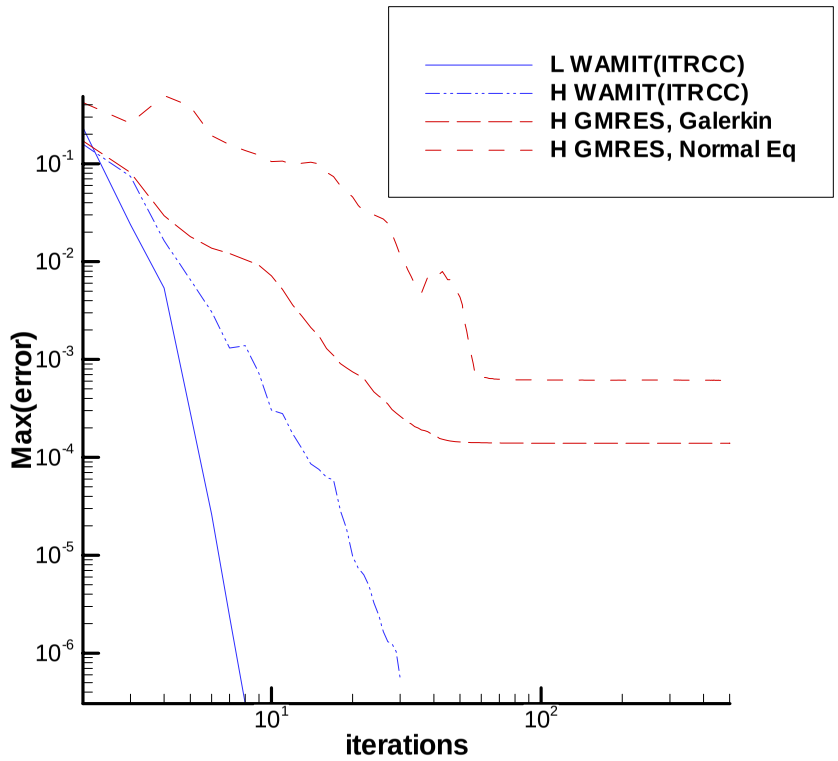

Surge

An array of 20 cylinders

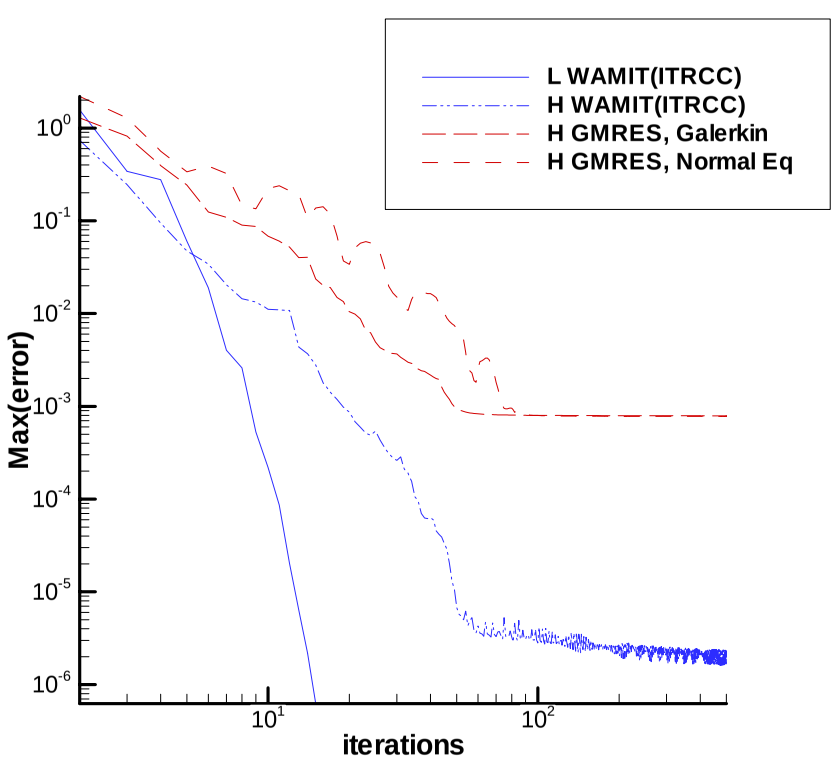

Heave

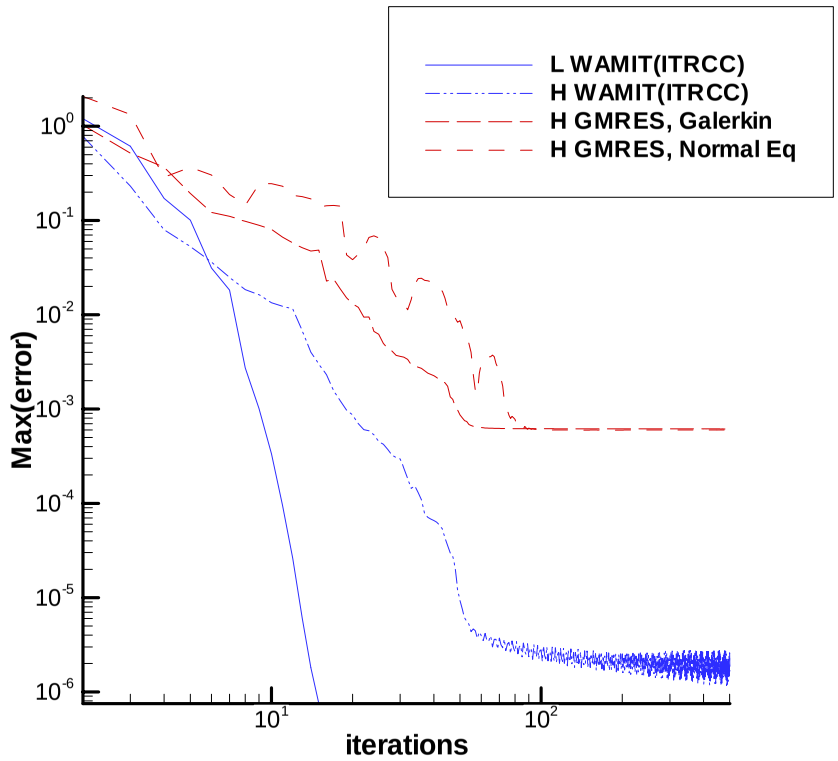

Surge

An array of 100 cylinders

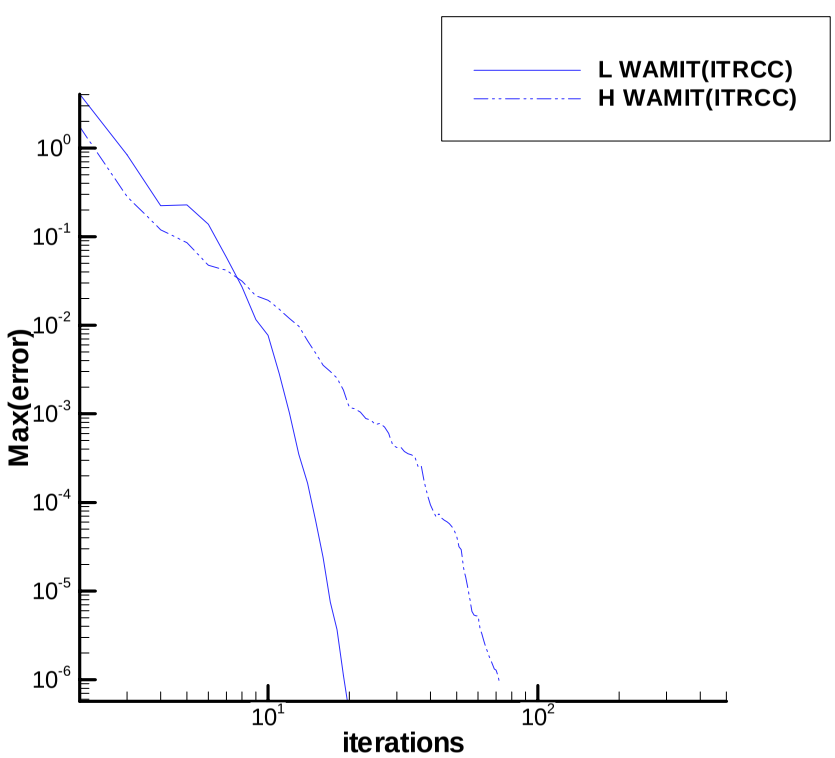

Heave

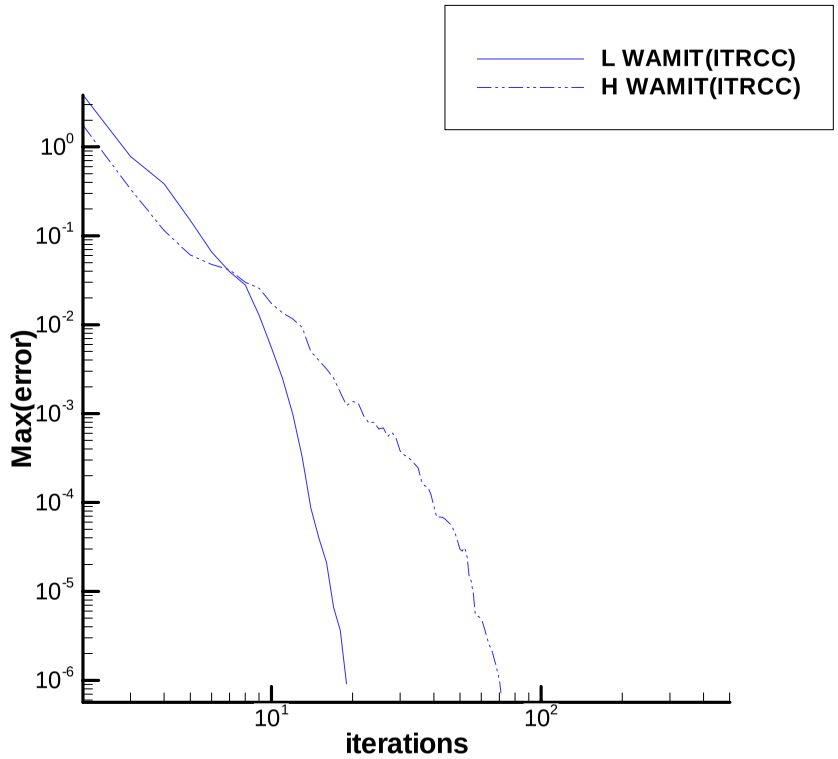

Surge

An array of 300 cylinders

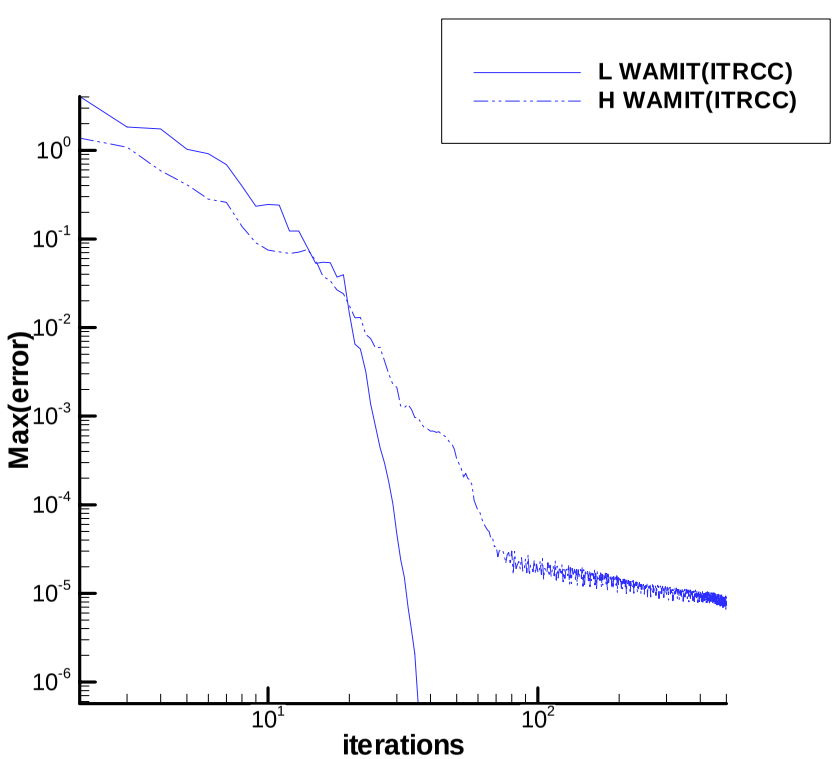

Heave

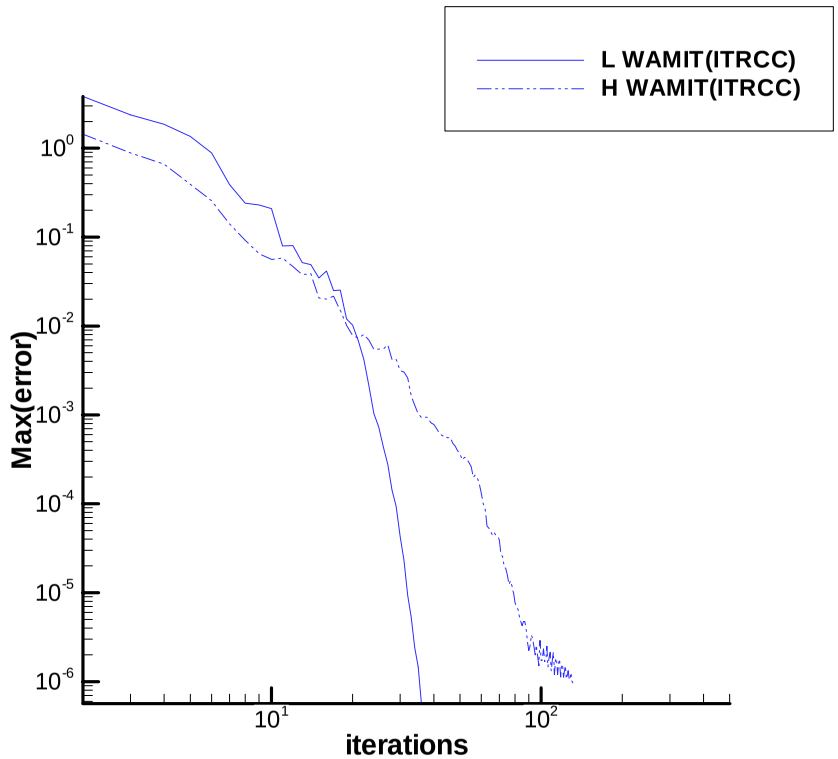

Surge

Current Participants

Chevron

Conoco

Norsk Hydro

OTRC

Petrobras/
USP

Shell

Statoil

Marcos Ferreira
Petrobras
Cenpes-Diprex-Sedem
Cidade Universitaria Quadra 7
21949-900 Ilha do Fundao
Rio de Janeiro, Brazil
marcos@cenpes.petrobras.com.br

Tim Finnigan
ChevronTexaco Energe Co.
6001 Bollinger Canyon Road
Room L-4296
San Ramon, CA 94583-2324
TimFinnigan@ChevronTexaco.com

George Gu
ConocoPhillips
OF 1004, 1E & PM
600 North Dairy Ashford
Houston, TX 77079
george.z.gu@conocophillips.com

Kjell Herford
Norsk Hydro ASA
PO Box 7190
N-5020 Bergen, Norway
Street Address
Sandsliveien 90
N-5254 Sandsli, Norway
Kjell.Herfjord@hydro.com

Kazuo Nishimoto
University of Sao Paulo
Department of Naval Architecture and Ocean Engineering
2231, Av. Prof. Mello Moraes
Cidade Universitaria
Sao Paulo, SP, Brazil CEPO05508-900
knishimo@usp.br

Stergios Liapis
Shell Oil Company
Offshore Structures
3737 Bellaire Blvd.
Houston, TX 77025
stergios.liapis@Shell.Com

Rick Mercier
Offshore Technology Research Center
1200 Mariner Drive
College Station, TX 77845-3400
rsmercier@tamu.edu

John Niedzwecki
Offshore Technology Research Center
1200 Mariner Drive
College Station, TX 77845-3400
j-Niedzwecki@.tamu.edu

Per Teigen
STATOIL
Postuttak
N 7005 Trondheim
Norway
pte@statoil.com

Street Address
Ark, Ebbels v.10
Rotvoll
Trondheim, Norway

John Letcher
AeroHydro
54 Herrick Road/PO Box 684
Southwest Harbor, ME 04679-0684
jletcher@aerohydro.com

Michael Shook
AeroHydro
54 Herrick Road/PO Box 684
Southwest Harbor, ME 04679-0684
mshook@aerohydro.com

Michael Graham
Dept. of Aeronautics
Imperial College
London, SW7 2BY
United Kingdom
m.graham@imperial.ac.uk

Nick Newman
WAMIT
1 Bowditch Road
Woods Hole, MA 02543
jnn@mit.edu

Chang-Ho Lee
WAMIT
822 Boylston Street, Suite 202
Chestnut Hill, MA 02467
chlee@wamit.com

Appendices

Second-order diffraction in short waves

by J. N. Newman
<jnn@mit.edu>

(19th Workshop on Water Waves and Floating Bodies – Cortona, Italy – 28-31 March 2004)

1 Introduction

Second-order wave loads are significant for various types of offshore structures. Many analytical studies have been performed, based on the assumption of potential flow and using perturbation expansions including all contributions of second order. Most results are for monochromatic incident waves, where the second-order effects include a second-harmonic and a time-independent component. Additional biharmonic effects must be considered in a spectrum, including both sums and differences of the first-order frequencies. Analytical studies are restricted either to two dimensions or to axisymmetric three-dimensional structures. Several numerical codes have been developed based on the panel method, to predict the second-order wave effects on more general structures in three dimensions.

When the incident waves are short, or the frequency ω is large, the first-order wave field is confined to a thin layer near the free surface. The first-order loads are asymptotically small, and can be analyzed by the method of geometric optics or ray theory. Little is known regarding second-order effects in this regime except for a few specific bodies. In general the second-order loads do not tend to zero (when normalized in the usual manner based on the square of the incident-wave amplitude). The simplest example is the oscillatory 'runup' at the waterline, which causes a concentrated pressure force equal to $\frac{1}{2}\rho g\zeta^2$, where ρ is the fluid density, g is the gravitational acceleration, and ζ is the first-order local free-surface elevation.

The pressure due to the second-order component of the potential is a more complicated cause of second-harmonic loads. Unlike the first-order diffraction field, the second-order potential persists at large depths below the free surface even when the first-order waves are very short (Newman, 1990). For specific bodies it has been shown that the second-harmonic force increases without bound, in proportion to the wavenumber ω^2/g in two dimensions (Wu & Eatock Taylor, 1989; McIver, 1994) and in proportion to the frequency ω for a vertical cylinder in three dimensions (Newman, 1996). Less is known regarding the behavior of the sum- and difference-frequency components in short biharmonic waves.

Our objective here is to derive asymptotic results for the second-order potential and loads in the short-wavelength regime. A simplified problem is considered, where waves are incident upon a two-dimensional (cylindrical) body which intersects the free surface. Both oblique and normal incidence are considered. For three-dimensional applications the results can be applied to elongated vessels using a strip-theory synthesis, and also to compact bodies where the radius of curvature along the waterline is large compared to the wavelength. Since the body motions are small in short waves, it is reasonable to consider only the diffraction problem where the body is fixed in position. The fluid depth is assumed to be infinite.

2 Formulation

The horizontal coordinates x, y are in the plane of the free surface and the z-axis is positive upward. The body is cylindrical with its generators parallel to the y-axis. The sides intersect the free surface vertically along the waterlines $x = \pm b$. Two incident waves ($i = 1, 2$) are considered, with complex amplitudes A_i, frequencies ω_i, wavenumbers $k_i = \omega_i^2/g$ and incidence angles β_i relative to the positive x-axis. The (x, y) components of the wavenumber vector are $u_i = k_i \cos\beta_i$ and $v_i = k_i \sin\beta_i$. Subscripts are used to denote the frequency components, and superscripts for the perturbation orders.

The total potential, correct to second order, is $\phi = \phi^{(1)} + \phi^{(2)}$. The first- and second-order potentials are given by the real parts of

$$\phi^{(1)} = A_1\phi_1 \mathrm{e}^{\mathrm{i}\omega_1 t} + A_2\phi_2 \mathrm{e}^{\mathrm{i}\omega_2 t}\,, \tag{1}$$

$$\phi^{(2)} = A_1^2\phi_{11}^{+}\mathrm{e}^{2\mathrm{i}\omega_1 t} + A_2^2\phi_{22}^{+}\mathrm{e}^{2\mathrm{i}\omega_2 t} + 2A_1A_2\phi_{12}^{+}\mathrm{e}^{\mathrm{i}(\omega_1+\omega_2)t} + 2A_1A_2^{*}\phi_{12}^{-}\mathrm{e}^{\mathrm{i}(\omega_1-\omega_2)t}\,. \tag{2}$$

The incident waves propagate toward the body in the domain $x < 0$, thus $|\beta_i| < \pi/2$ and $u_i > 0$. Since the wavelength is short relative to the dimensions of the body, complete reflection is assumed for the first-order solution at the waterline $x = -b$. Thus, in the domain $x \le -b$,

$$\phi_i \simeq \frac{2g}{\omega_i}\cos\left(u_i(x+b)\right)\mathrm{e}^{k_i z + \mathrm{i}u_i b - \mathrm{i}v_i y}\,. \tag{3}$$

The first-order solution vanishes to leading order for $x \ge b$ and in the region below the body.

3 The second-order free-surface condition

The potential $\phi^{(2)}$ satisfies the homogeneous condition $\phi_n^{(2)} = 0$ on the submerged surface of the body, and the inhomogeneous free-surface condition

$$\phi_{tt}^{(2)} + g\phi_z^{(2)} = -\frac{\partial}{\partial t}\left(\nabla\phi^{(1)}\right)^2 \quad \text{on} \quad z = 0 \quad \text{and} \quad |x| > b\,. \tag{4}$$

The right-hand side of (4) is simplified since the first-order potentials are of the form (3).

Since the second-harmonic terms involving $\mathrm{e}^{2\mathrm{i}\omega_i t}$ can be recovered from the sum-frequency term as special cases, we consider only the last two terms in (2). After substituting (3) in (4) and performing some reduction the second-order free-surface condition takes the form

$$\begin{aligned} -(\omega_1 \pm \omega_2)^2\phi_{12}^{(\pm)} + g\phi_{12z}^{(\pm)} = -\mathrm{i}H(-x)(\omega_1 \pm \omega_2)\frac{g^2}{\omega_1\omega_2}\mathrm{e}^{-\mathrm{i}(v_1 \pm v_2)y + \mathrm{i}(u_1 \pm u_2)b} \\ \Big[(k_1k_2 \mp v_1v_2 - u_1u_2)\cos((u_1+u_2)(x+b)) \\ +(k_1k_2 \mp v_1v_2 + u_1u_2)\cos((u_1-u_2)(x+b))\Big]\,. \end{aligned} \tag{5}$$

Here $H(-x)$ is the Heaviside unit function, which vanishes for $x > 0$. In general there are two components of the forcing function on the right side of (5) which are oscillatory in the x-direction with the wavenumbers $u_1 \pm u_2$. These two wavenumbers are present for both the sum- and difference-frequency cases. In special cases, where the factor $(k_1k_2 \mp v_1v_2 - u_1u_2) = 0$, only one component exists with the 'slow' wavenumber $u_1 - u_2$. This follows in all cases of normal incidence, where $v_i = 0$ and $u_i = k_i$, and also for the sum-frequency case in oblique monochromatic waves. The slow component is particularly important when $u_1 - u_2 \to 0$ since the forcing is nearly constant, extending to infinity, and this results in a second-order solution which persists to large depths in the fluid.

4 Particular solutions of the free-surface condition

Solutions of the free-surface condition (5) can be decomposed into components which are solutions of

$$-\nu\varphi + \varphi_z = H(-x)\mathrm{e}^{-\mathrm{i}ux-\mathrm{i}vy} \quad \text{on} \quad z = 0\,. \tag{6}$$

Particular solutions which satisfy (6) can be combined so that the remaining components of the second-order potential satisfy either homogeneous boundary conditions on the free surface or inhomogeneous conditions where the forcing functions on the right-hand-side tend to zero away from the body.

Solutions of (6) can be constructed from the potential for a pressure distribution on the free surface (Wehausen & Laitone, 1960, equation 21.3). The forcing function on the right side of (6) is first restricted to a finite rectangular domain ($-M < x < 0,\ -M < y < +M$), and the limit as $M \to \infty$ is evaluated. This gives the solution in the form

$$\varphi = \frac{\mathrm{i}}{2\pi}\mathrm{e}^{-\mathrm{i}vy}\int_C \frac{\mathrm{e}^{kz+\mathrm{i}rx}\,dr}{(k-\nu)(r+u)}\,, \tag{7}$$

where $k = \sqrt{r^2+v^2}$ and C is an appropriate contour of integration between $\mp\infty$. The pole at $r = -u$ is associated with the 'locked waves', which propagate with the same phase as the forcing function in (6). Defining the contour C to pass above this pole ensures that the integration from $-M$ to 0 tends to a finite limit as $M \to \infty$. Two other poles are associated with the 'free waves', where $k = \nu$ and $r = \pm\sqrt{\nu^2-v^2} \equiv \pm\mu$. The radiation condition requires that $\mathrm{Im}(k) > 0$, and thus when μ is real the contour C passes above the pole $r = +\mu$ and below the pole $r = -\mu$. Except for these three poles, and branch points at $r = \pm\mathrm{i}v$ associated with the function $k = \sqrt{r^2+v^2}$, the integrand of (7) is analytic in the complex r-plane. Branch cuts are established extending from $\pm\mathrm{i}|v|$ to $\pm\mathrm{i}\infty$ on the imaginary axes, and k is continued into the cut plane with the convention that $k > 0$ on the real axis.

For $x \gtrless 0$ the contour C in (7) can be replaced by a contour around the upper or lower branch cut, respectively. It follows from residue theory that

$$\varphi = \left[\pm\frac{1}{2\pi}\,I(\pm u) + \frac{\nu(u\pm\mu)}{\mu(\kappa^2-\nu^2)}\mathrm{e}^{\nu z-\mathrm{i}\mu|x|} + H(-x)\frac{\mathrm{e}^{\kappa z-\mathrm{i}ux}}{\kappa-\nu}\right]\mathrm{e}^{-\mathrm{i}vy}\,, \tag{8}$$

where the sign ($\pm$) corresponds to the domain $x \gtrless 0$ and

$$I(u) = \int_{|v|}^{\infty}\frac{\mathrm{e}^{-t|x|}}{t-\mathrm{i}u}\left[\frac{\mathrm{e}^{\mathrm{i}wz}}{w+\mathrm{i}\nu} + \frac{\mathrm{e}^{-\mathrm{i}wz}}{w-\mathrm{i}\nu}\right]dt\,. \tag{9}$$

Here $\kappa = \sqrt{u^2+v^2}$ and $w = \sqrt{t^2-v^2}$. When $u = 0$ and $v = 0$, corresponding to the limit where the oscillatory part of the forcing function on the right side of (6) is constant, (9) reduces to the integral representation derived in a different manner by Miao & Liu (1989, equation 14).

For large values of $|\nu x|$ and $|\kappa x|$ I tends to zero, exponentially for $|v| > 0$ and in proportion to $|x|^{-2}$ when $v = 0$. In these cases the first term in (8) is evanescent. However when $\kappa = \sqrt{u^2+v^2} = 0$, the combination of the first and third terms is vortex-like in the far field, as shown in the next Section. This is the dominant cause of the second-order force in short wavelengths. The second term in (8) represents radiating free waves on both sides of $x = 0$. The locked waves represented by the third term exist only in $x < 0$.

For the sum-frequency case, where $\nu = (\omega_1+\omega_2)^2/g$, it is easy to show that $\nu^2 > (u^2+v^2)$; thus $(\mu^2-u^2) = (\nu^2-\kappa^2) > 0$, and μ is real. For the difference-frequency case, $\nu = (\omega_1-\omega_2)^2/g$, regimes exist where $\nu^2 < v^2$ and μ is imaginary. In these regimes the poles at $r = \pm\mu$ are on the imaginary axis, and the first exponential in (8) is replaced by $\mathrm{e}^{\nu z-|\mu x|}$; thus the free waves are trapped, with exponential attenuation in both the $\pm x$-directions.

5 Normal incidence

For normal incidence, where $v_i = 0$ and $u_i = k_i$,

$$I(u) = \frac{\mathrm{i}}{\nu^2 - u^2}\Big\{(\nu - u)\left[\mathrm{e}^{\mathrm{i}\nu\zeta^*}E_1(\mathrm{i}\nu\zeta^*) - \mathrm{e}^{-\mathrm{i}u\zeta^*}E_1(-\mathrm{i}u\zeta^*)\right] \\ -(\nu + u)\left[\mathrm{e}^{-\mathrm{i}\nu\zeta}E_1(-\mathrm{i}\nu\zeta) - \mathrm{e}^{-\mathrm{i}u\zeta}E_1(-\mathrm{i}u\zeta)\right]\Big\}. \qquad (10)$$

Here E_1 denotes the exponential integral and $\zeta = |x| + \mathrm{i}z$. For monochromatic waves $|u| = |u_1 - u_2| \to 0$, and the limiting value of (8) is

$$\varphi(0) = -\frac{\pi - 2\theta}{2\pi\nu} + \frac{\mathrm{sgn}(x)}{2\pi\mathrm{i}\nu}\left\{\mathrm{e}^{-\mathrm{i}\nu\zeta}E_1(-\mathrm{i}\nu\zeta) - \mathrm{e}^{\mathrm{i}\nu\zeta^*}E_1(\mathrm{i}\nu\zeta^*)\right\} - \frac{\mathrm{sgn}(x)}{\nu}\mathrm{e}^{\nu z - \mathrm{i}\nu|x|}, \qquad (11)$$

where $\theta = \tan^{-1}(x/|z|)$.

An interesting connection exists between the particular solution (11) and the 'line vortex potential' λ derived by McIver (1994, equation 24). Both are harmonic functions which satisfy the same free-surface condition, and thus they differ by a homogeneous solution of the free-surface condition. Using relations given by Wehausen & Laitone (1960, equations 13.28-31), it can be shown that (11) is equivalent to the potential of a point vortex at $x = 0$, $z = 0$, and the difference between (11) and McIver's λ is a horizontal dipole at the same point.

6 Applications

Results will be shown comparing the second-order forces obtained from these approximate solutions with computations for three-dimensional bodies carried out using the second-order extension of the panel code WAMIT. In some cases the agreement is sufficiently good to provide a useful quantitative estimate. In other cases the practical value of the approximation is only qualitative.

REFERENCES

McIver, M., 1994 Second-order wave diffraction in two dimensions, *Applied Ocean Research* **16**, 19–25.

Miao, G.P. & Liu, Y.Z., 1989 A theoretical study on second-order wave forces for two-dimensional bodies, *J. Offshore Mechanics and Arctic Engineering* **111**, 37–42.

Newman, J.N., 1990 Second-harmonic wave diffraction at large depths, *J. Fluid Mech.* **213**, 59–70.

Newman, J.N., 1996 The second-order wave force on a vertical cylinder, *J. Fluid Mech.* **320**, 417–443.

Wehausen, J.V. and Laitone, E.V., 1960 Surface Waves. *Handbuch der Physik*, **9**, pp. 446-778. (Available for download from `www.coe.berkeley.edu/SurfaceWaves`)

Wu, G.X. & Eatock Taylor, R., 1989 Second order diffraction forces on horizontal cylinders, *J. Hydrodynamics* **2**, 55–65.

Wave effects on vessels with internal tanks

by: J. N. Newman

September 29, 2004

1 Introduction

The motions of fluid in internal tanks have important effects on the dynamic response of vessels in waves, particularly when the tanks are partially filled. This topic is of special interest for LNG tankers and FPSO vessels.

Recent studies of coupled tank/ship motions have been made by Kim (2001) and Rognebakke & Faltinsen (2001, 2003), who couple nonlinear analyses of the tanks with linear analyses of the flow exterior to the vessel, and by Molin *et al* (2002) and Malenica *et al* (2003) who use linear analyses for both the tanks and the exterior flow. In these works the tank dynamics are analysed separately from the vessel's exterior flow, and the corresponding forces are combined in the equations of motion.

In the present work a more unified approach is adopted, based on the three-dimensional linear panel code WAMIT. In this and similar radiation/diffraction codes, the exterior flow is analysed by the panel method, either by using a simple source distribution on the boundary surface or a combined distribution of sources and normal dipoles (cf. Lee and Newman, 2004). In the usual approach for linearized free-surface problems, the Green function (source potential) satisfies the boundary conditions on the free surface, bottom boundary, and a radiation condition in the far field. It follows that the source strength or dipole moment is the solution of an integral equation on the exterior wetted surface of the body. Numerical solutions are achieved by discretization of the wetted surface and reduction of the integral equation to a linear system of algebraic equations. From a physical standpoint the kernel of the integral equation, or the coefficient matrix of the linear system, can be interpreted as the influence at one field point on the surface from a singularity at another source point.

Here the internal surfaces of the tanks are represented in the same manner as the exterior wetted surface of the hull, in essence by combining all of the appropriate tank and hull surfaces to form one large global wetted surface which forms the boundary between the fluid domains and the vessel. The only fundamental modification required is to impose the condition that the separate fluid domains are independent. This is achieved trivially, by setting equal to zero all elements of the coefficient matrix where the source and field points are in different domains. From the standpoint of linear system algebra, this is equivalent to forming separate sets of linear

equations for each domain, and concatenating these into one larger system in a block-diagonal manner.

The principal advantage of this approach is that the exterior panel code can be extended to include internal tanks, with relatively few modifications, and all of the hydrodynamic parameters can be evaluated in a similar manner as for one or more vessels without tanks. Typical parameters of interest include the radiation force coefficients (added mass and damping), exciting forces, response-amplitude-operators (RAO's) for motions of the body, fluid pressures and velocities, and mean second-order drift forces and moments. Another advantage is that the geometry of the tanks can be described in the same manner, and with the same generality, as the exterior hull surface. Disadvantages include the larger size of the linear system, which implies some loss of computational efficiency, and the need to re-run the complete interior/exterior analysis in situations where only one or the other is changed, e.g. when the tank depths are modified.

Four applications are shown here to illustrate the coupled motions of vessels with internal tanks. The first example is the barge model studied previously by Molin *et al* (2002), where experimental data are available for comparison. The other examples are intended to show typical results for an FPSO ship of length 300m and beam 50m, with four internal tanks. Three different hull shapes are used, including a spheroid, a generic FPSO, and a prototype FPSO. Each of these is described separately below. In all cases the higher-order method is used for the analysis. For the practical FPSO the geometry is defined by the CAD program MultiSurf. For the other applications the geometry is defined analytically. Results are shown for the response-amplitude operators (RAO's), added mass, free-surface elevations in the tanks, and the mean drift forces. For the last three examples results are shown for three relative densities of the tank fluid, 0, 0.5 and 1.0. The total displacement and waterline plane are fixed as the tank density is varied. The results with zero tank density are equivalent to the results where there are no internal tanks. The results presented for the drift forces are based on momentum conservation, and comparisons are noted between the drift forces based on momentum and direct pressure integration. All results are normalized by the exterior fluid density, gravity, wave amplitude, and a characteristic length scale of 1m.

2 Barge model

Molin *et al* (2002) present computational and experimental results for a rectangular barge of length 3m, beam 1m, and draft 0.108m in beam seas. Two rectangular tanks are mounted with the tank bottoms 0.192m above the exterior free surface. The tanks are symmetrically located fore-and-aft, about the midship section. The tanks are 0.25m long, and 0.8m wide. The center-of-gravity is 0.132m above the exterior free surface (VCG), and the roll radius of gyration k_x=0.414m.

Results are shown here in Figures 1-3 for the case where the tanks are both filled to the same depth 0.19m, corresponding to Molin *et al* Figures 2, 4, and 5, and in Figures 4-6 for the case where the tanks are filled to different depths, 0.19m and 0.39m, corresponding to Molin *et al* Figures 8, 9, 10. For these computations a constant roll damping coefficient $B_{44} = 0.06$ is used for the WAMIT computations, whereas Molin *et al* use stochastic linearization to determine the

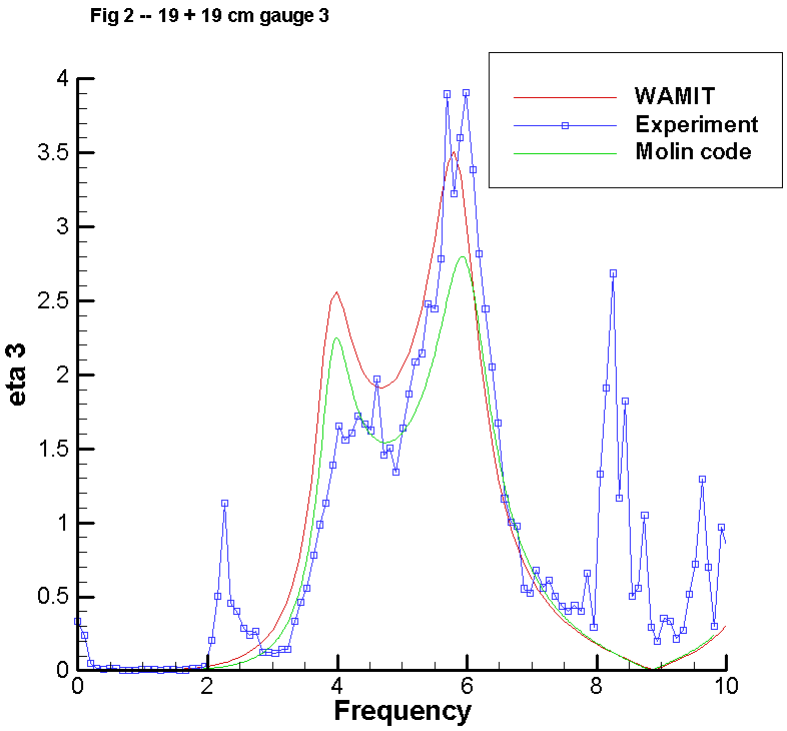

Figure 1: Comparison of results for the free-surface elevation in one tank 25mm from the upwave wall. These results correspond to Figure 2 of Molin *et al* (2002). Both tank depths are equal to 0.19m.

roll damping. The parameter Panel_Size=0.25 is used for the present computations. Limited convergence tests have been performed with Panel_Size=0.125, to verify the accuracy of the results.

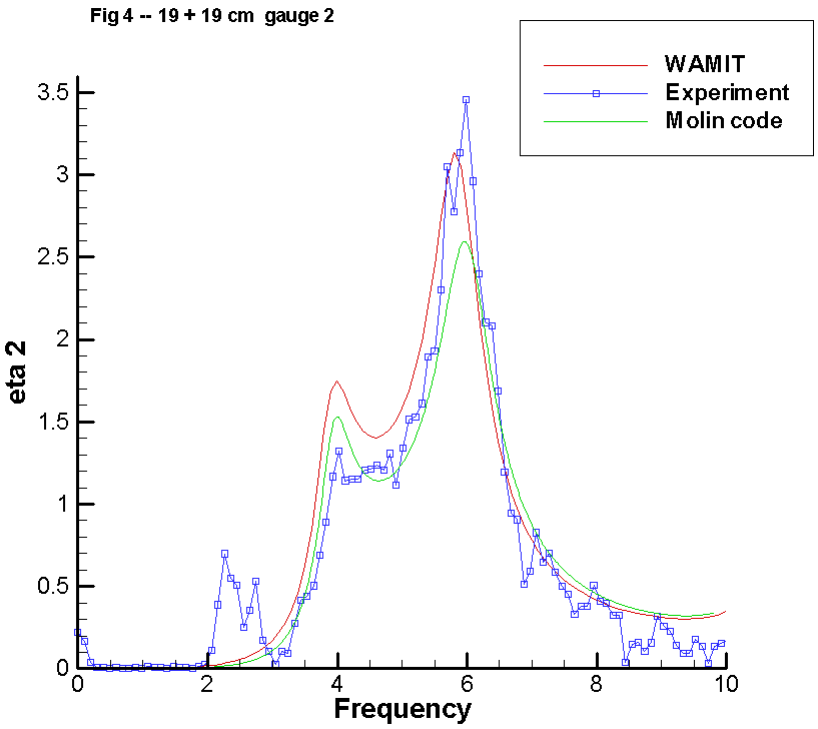

Figure 2: Comparison of results for the free-surface elevation in one tank 180mm from the upwave wall. These results correspond to Figure 4 of Molin *et al* (2002). Both tank depths are equal to 0.19m.

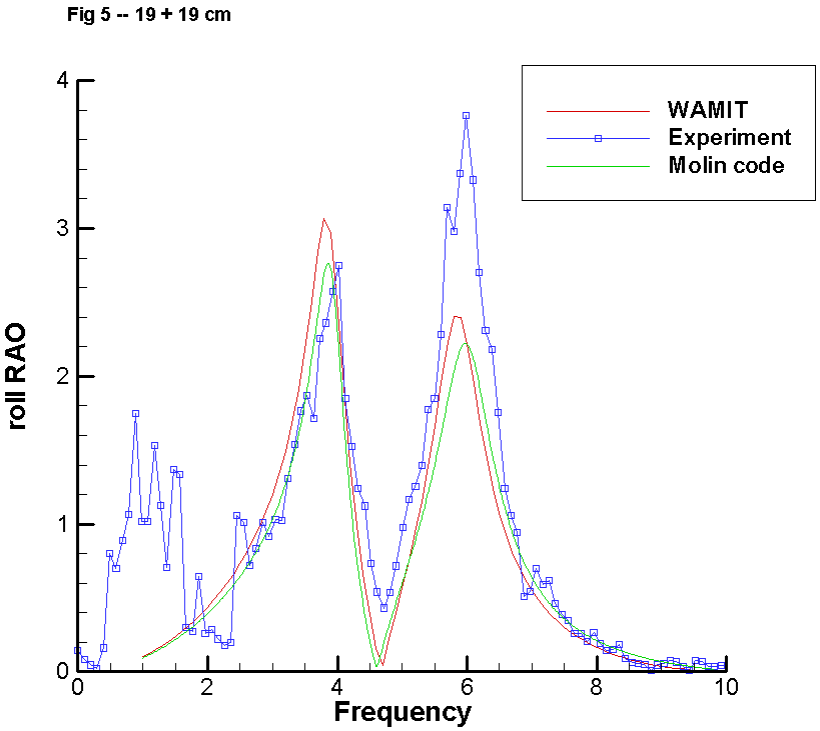

Figure 3: Comparison of results for the roll RAO. These results correspond to Figure 5 of Molin *et al* (2002). Both tank depths are equal to 0.19m.

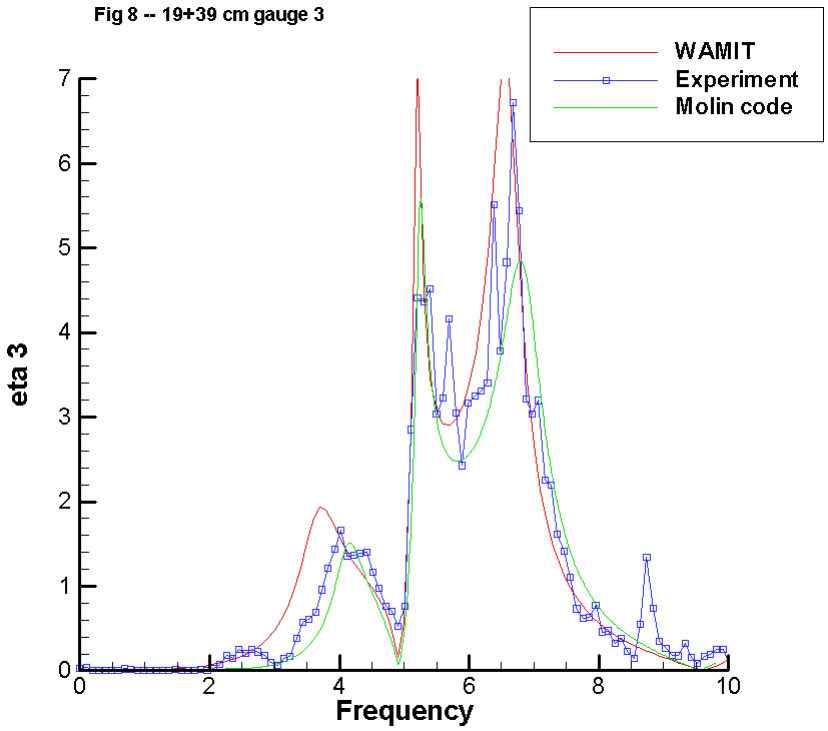

Figure 4: Comparison of results for the free-surface elevation in the deeper tank 25mm from the upwave wall. These results correspond to Figure 8 of Molin *et al* (2002). The tank depths are equal to 0.19m and 0.39m.

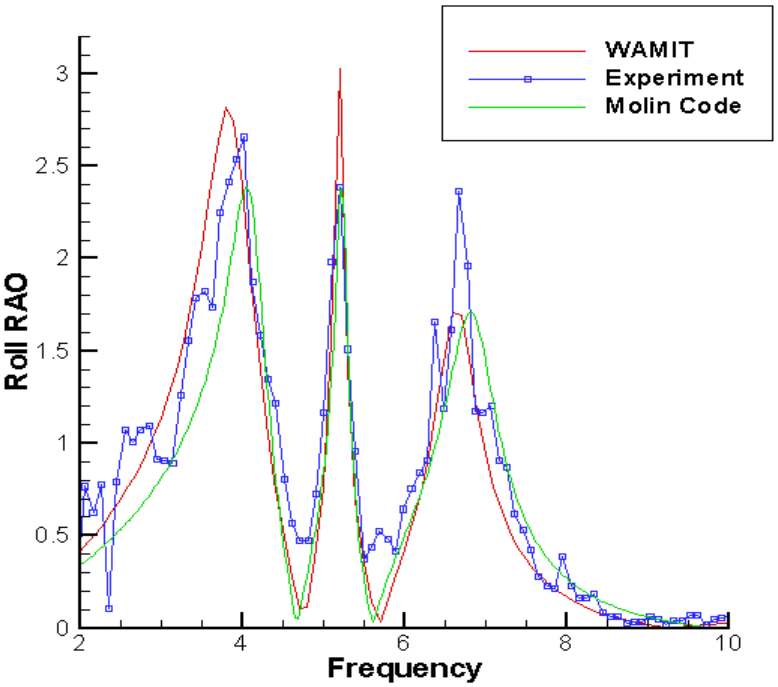

Figure 5: Comparison of results for the roll RAO. These results correspond to Figure 9 of Molin *et al* (2002). The tank depths are equal to 0.19m and 0.39m.

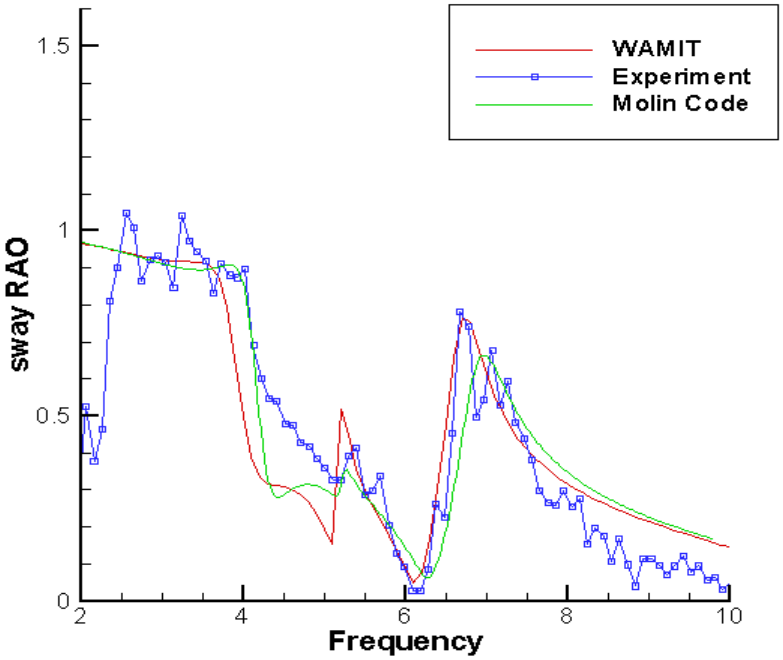

Figure 6: Comparison of results for the sway RAO. These results correspond to Figure 10 of Molin *et al* (2002). The tank depths are equal to 0.19m and 0.39m.

3 Spheroid

This hull shape was chosen for initial testing of the drift forces since the surface has continuous slope, ensuring good convergence of the pressure drift force. Only the results for the momentum drift forces are shown; the results for the pressure drift force are the same within graphical precision. The parameter Panel_Size=10 was used, and convergence was assumed based on the good agreement between the momentum and pressure drift forces.

The multiple peaks in the sway response and sway drift force are due to the presence of tanks with three different widths, thus there are three distinct sloshing frequencies in the transverse direction. This is confirmed by Figure 12, which shows the surge and sway added mass, for the tank densities $\rho = 0$ and 1. For $\rho = 1$, the peak periods of the RAO's correspond closely to the periods where the sum of the added mass and displaced mass is equal to zero, indicated by the points where the red curves cross the dashed black lines in Figure 12. (The actual peak periods are slightly smaller, due to coupling with other modes.)

Another point to note is that the roll response is zero for the case of zero tank density, since the body is axisymmetric, but when tanks are present these induce nonzero rolling moments.

For these computations VCG=0.0, k_x=15m, and $k_y = k_z$=75m.

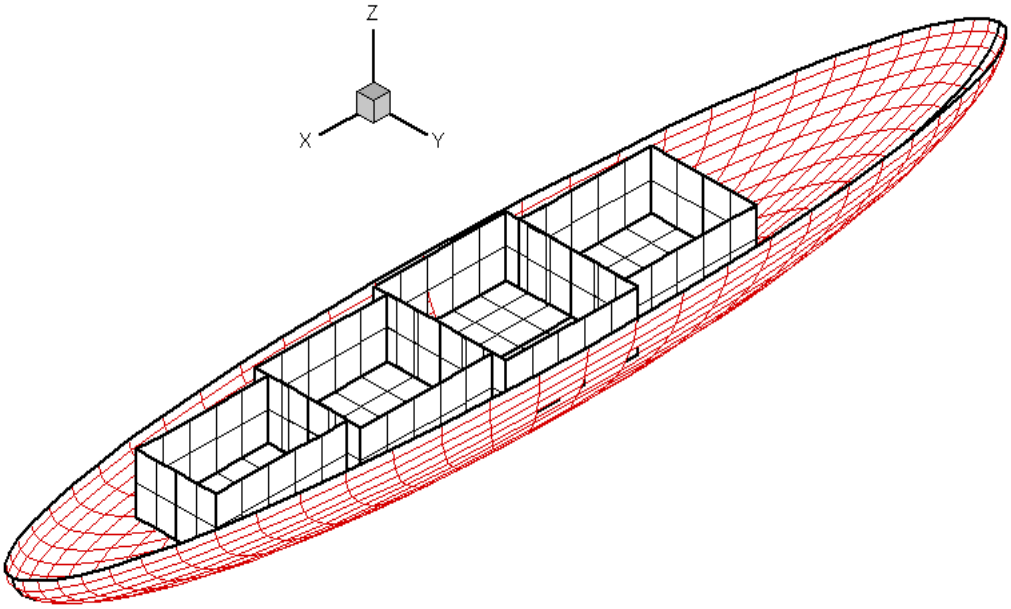

Figure 7: Perspective view of the spheroidal hull with four internal tanks. The length of the hull is 300m and the midship section is a semi-circle of radius 25m. Each tank is 40m long, and 15m deep, with the free surface 3m above the exterior free surface and the tank bottom 12m below the exterior free surface. The tank widths are 24m, 32m, 40m, and 32m, progressing from x=+100m to x=-60m.

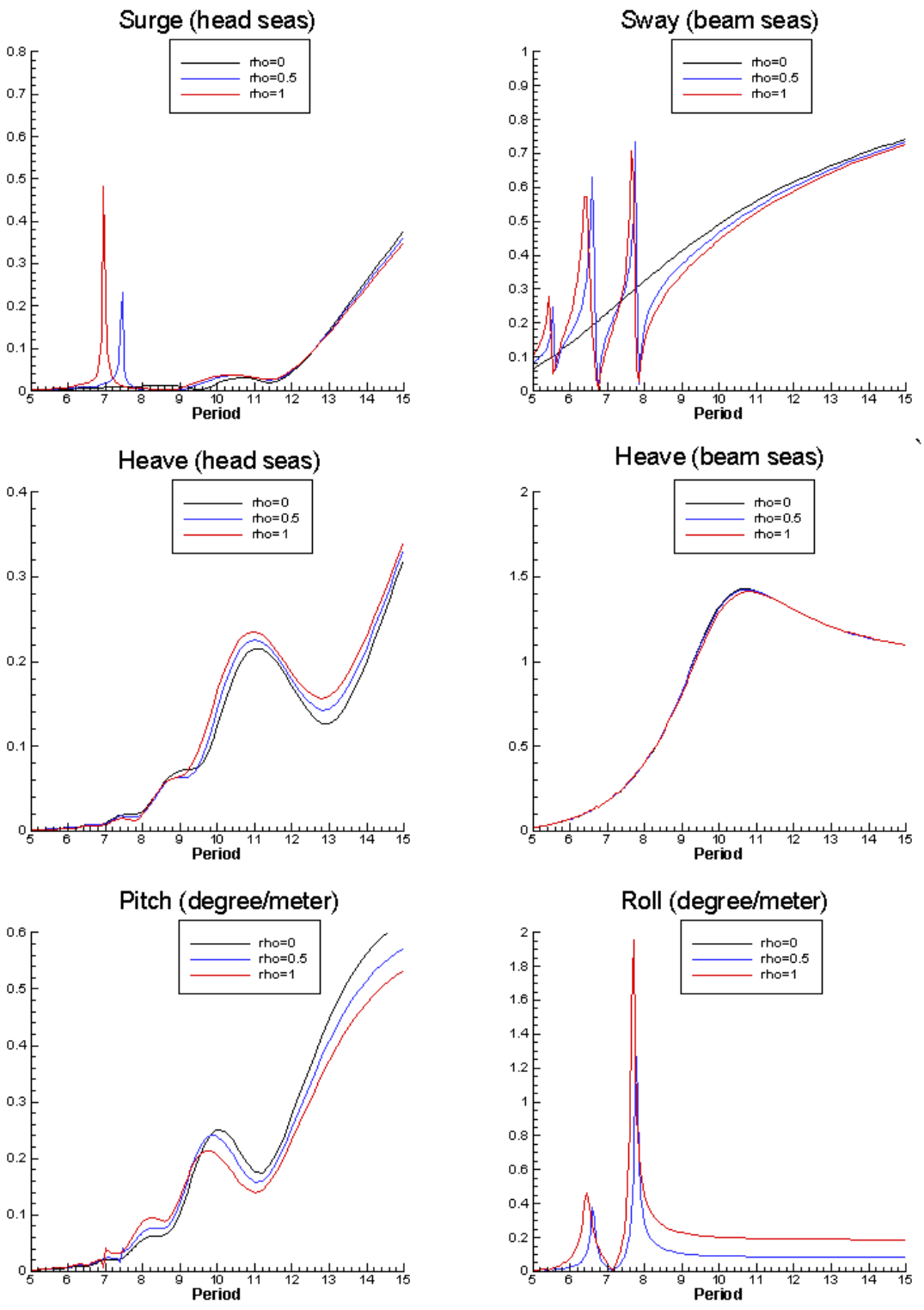

Figure 8: RAO's of the spheroidal hull in head waves (left) and beam waves (right).

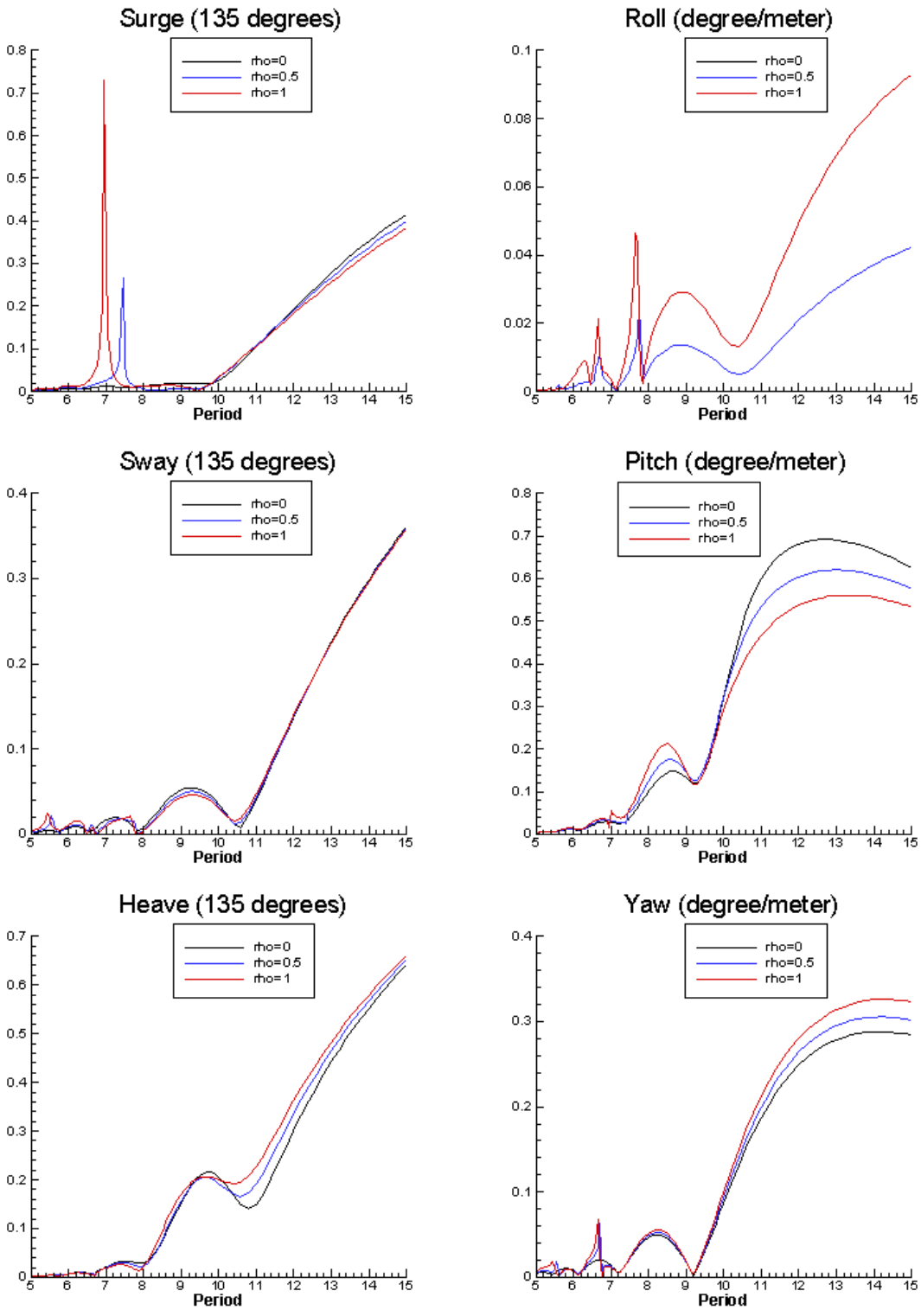

Figure 9: RAO's of the spheroidal hull in bow waves ($\beta = 135^o$).

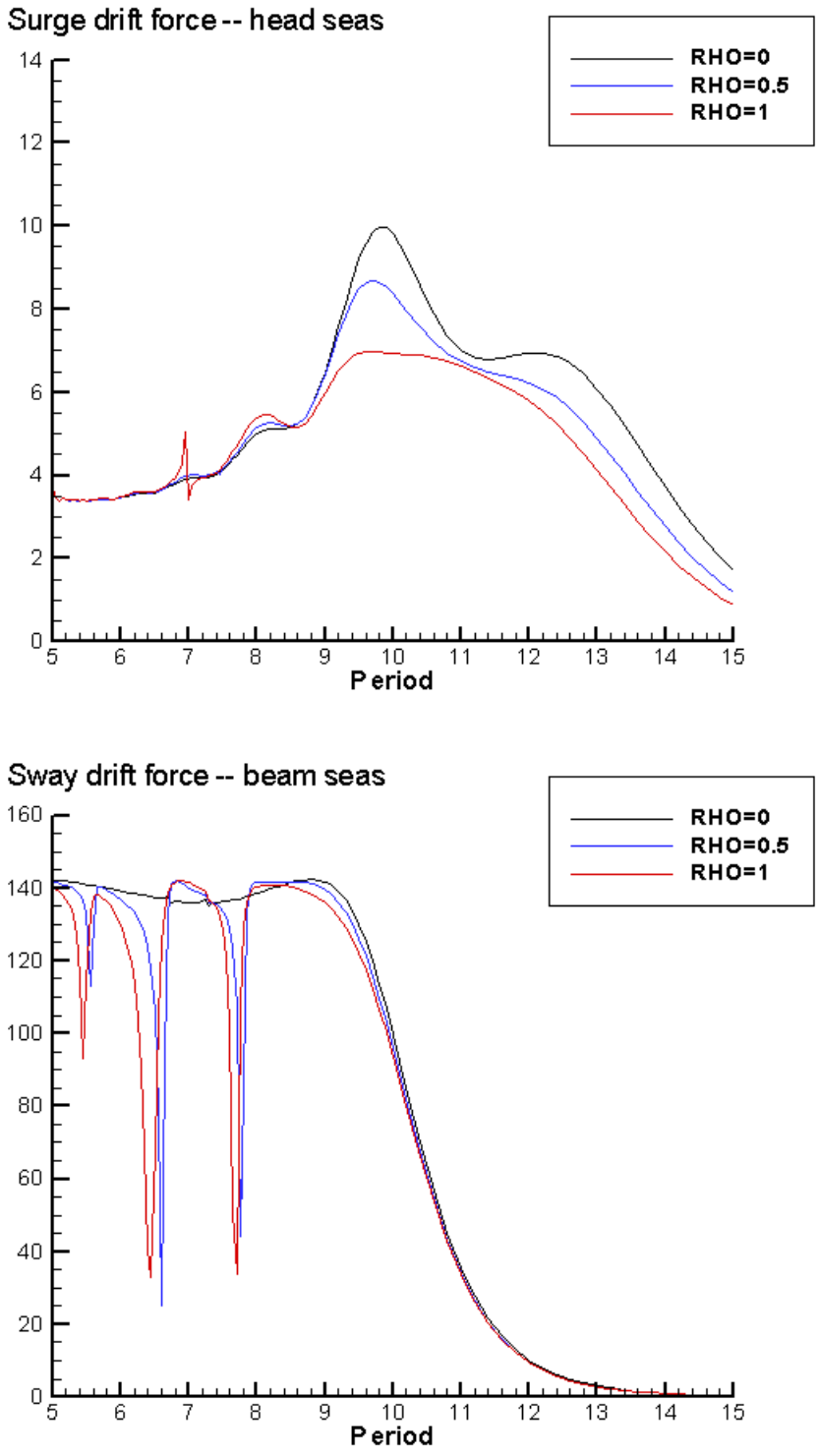

Figure 10: Drift forces of the spheroidal hull in head waves (top) and beam waves (bottom).

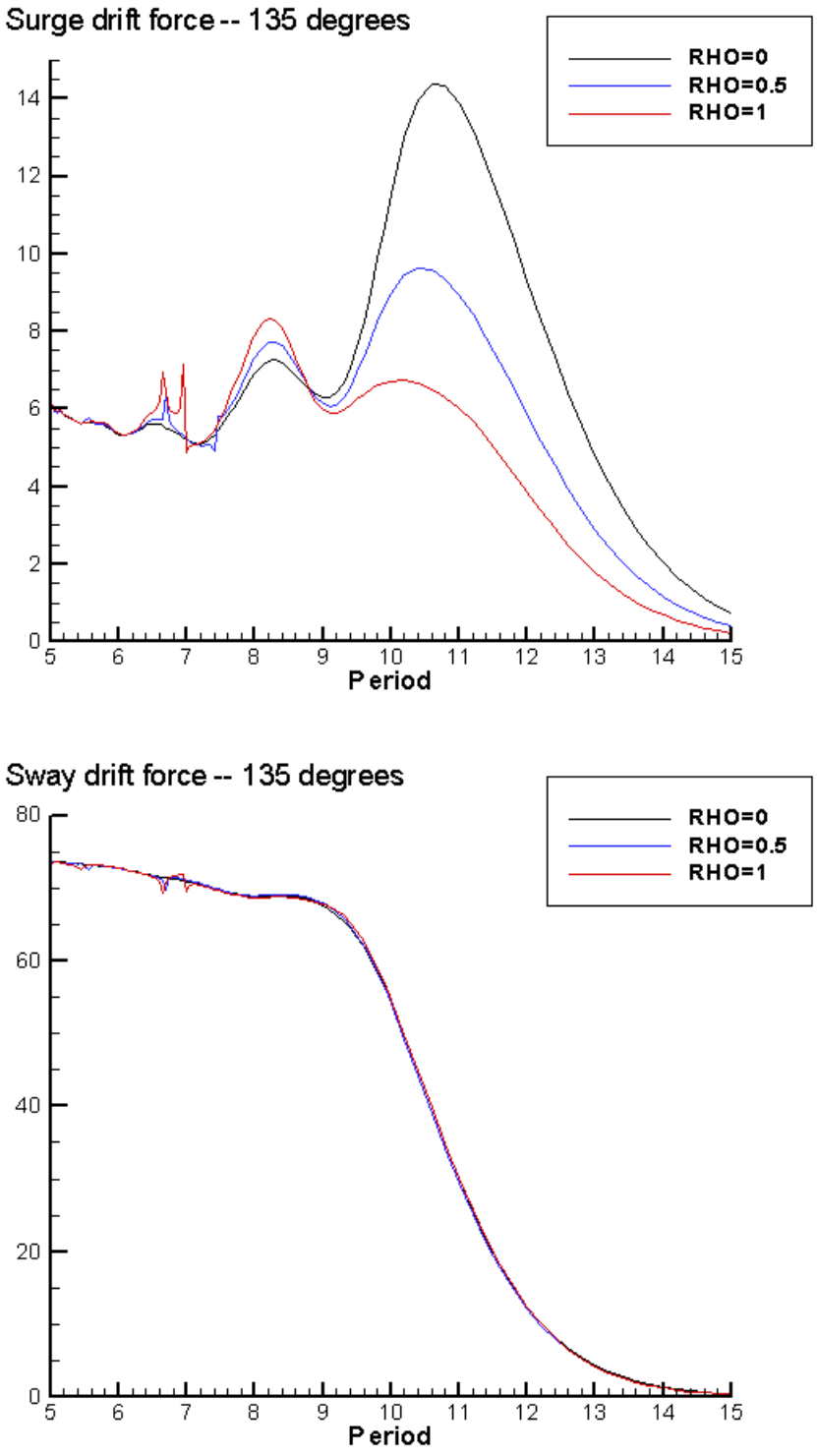

Figure 11: Drift forces of the spheroidal hull in bow waves ($\beta = 135^o$).

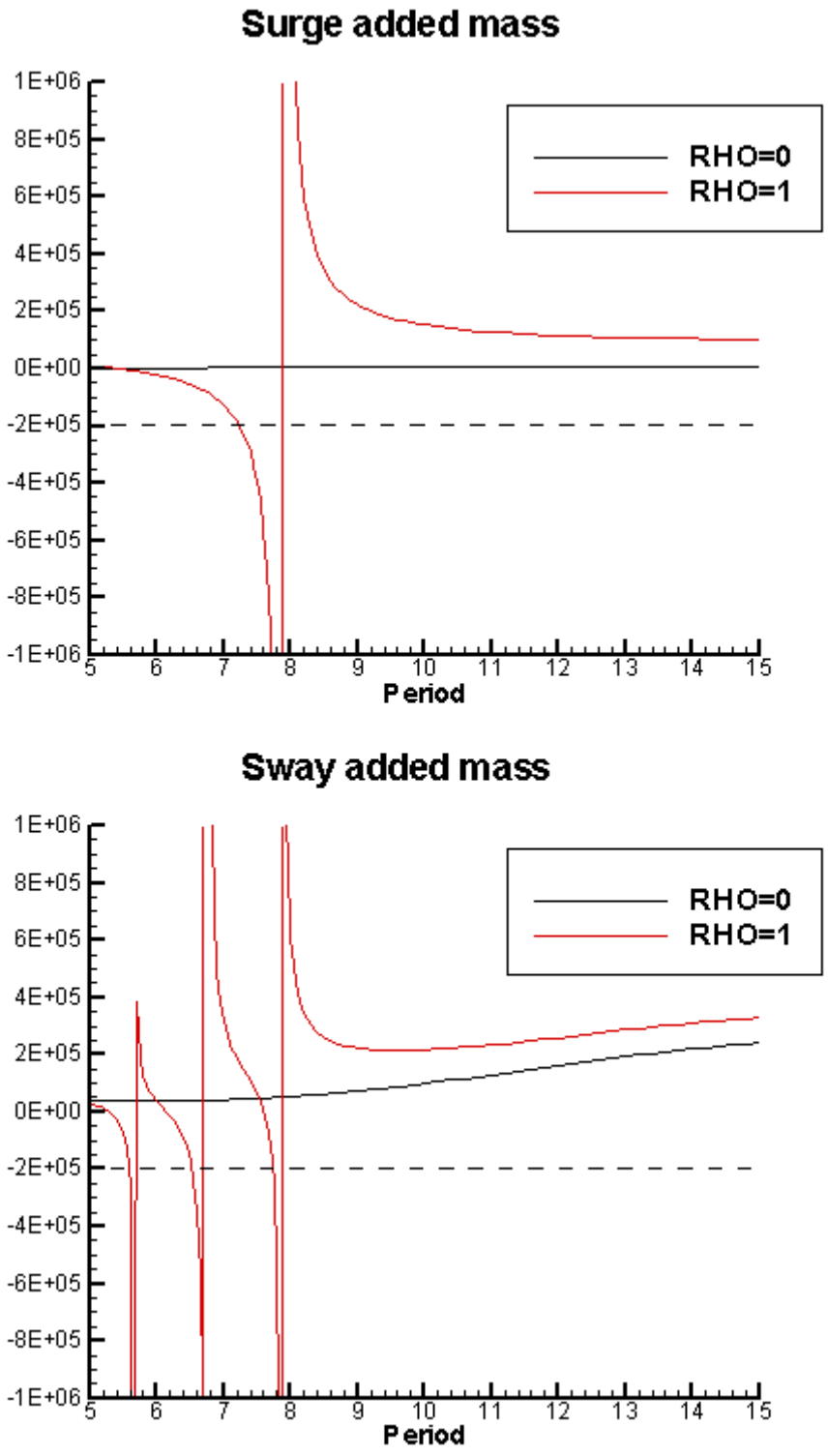

Figure 12: Added mass of the spheroidal hull in surge (top figure) and sway (bottom figure). The dashed line is the negative of the displaced mass. The vertical red lines joining the negative and positive branches of the added mass are plotting anomalies, and the points where these intersect the dashed lines are not physically relevant.

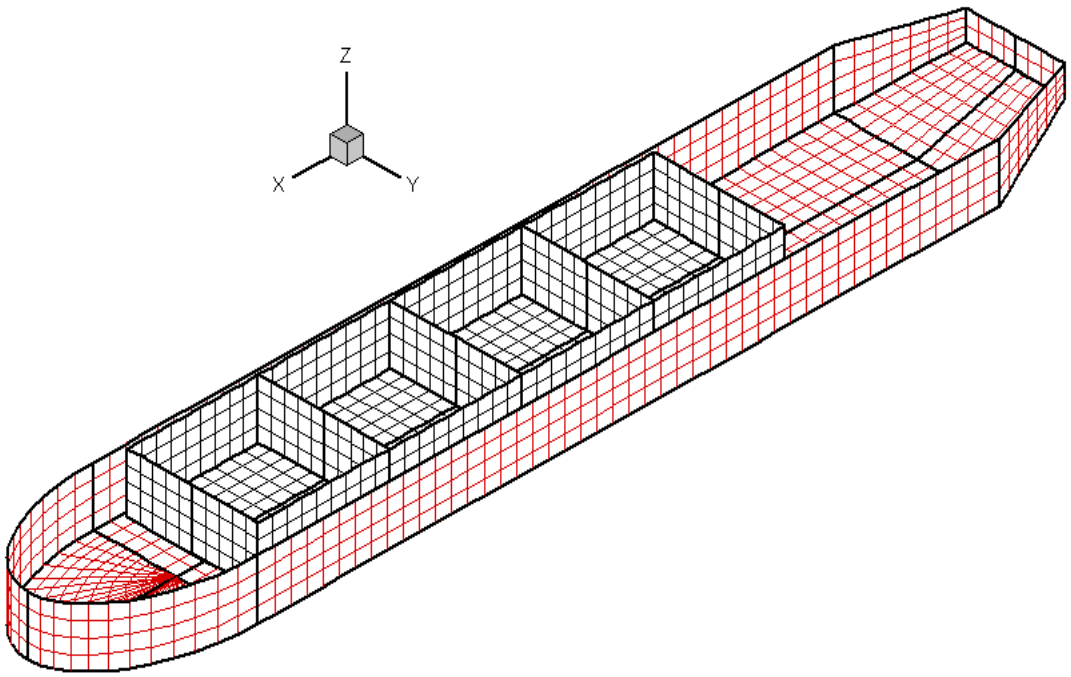

Figure 13: Perspective view of the generic FPSO hull with four internal tanks. The principal dimensions of the hull are 300m long, 50m beam, and 15m draft. Each tank is 40m long, 40m width, and 15m deep, with the free surface 3m above the exterior free surface and the tank bottom 12m below the exterior free surface. The tanks are located between x=+100m to x=-60m.

4 Generic FPSO

This hull form is generated using an extended version of the GEOMXACT subroutine FPSO to define the tank geometry by flat rectangular patches. The parameter Panel_Size=5 is used, and convergence has been verified by performing computations at a limited set of wave periods with Panel_Size=2.5. For the momentum drift forces the two sets of results are graphically identical. However the agreement between the momentum and pressure drift forces was only fair, with the pressure forces somewhat larger than the momentum forces at the longer wave periods. At shorter periods the two agreed well. Presumably the difference is due to the sharp corner at the bilge, which is not so important in shorter wavelengths.

For these computations VCG=0.0, k_x=15m, and $k_y = k_z$=75m.

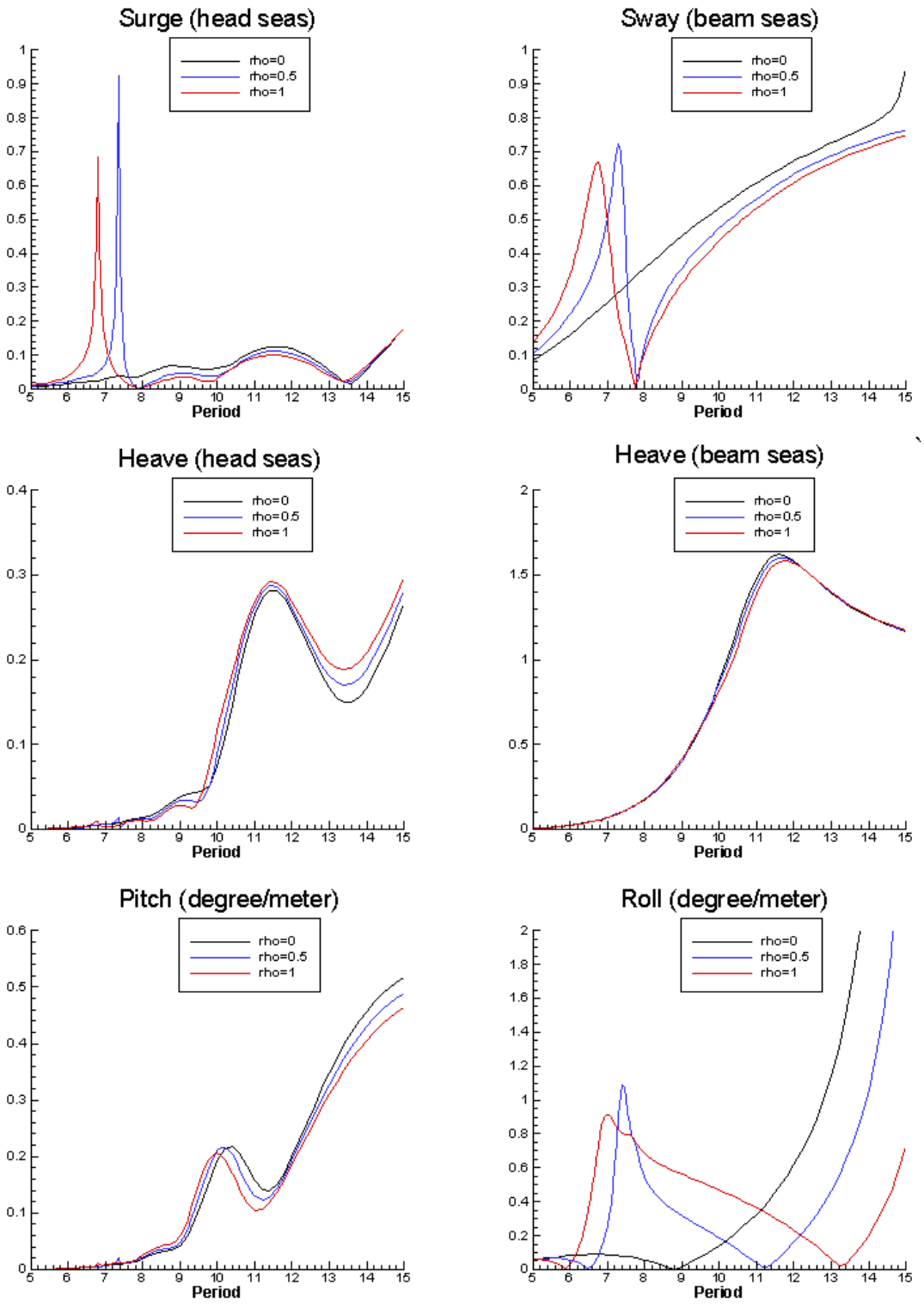

Figure 14: RAO's of the generic FPSO hull in head waves (left) and beam waves (right).

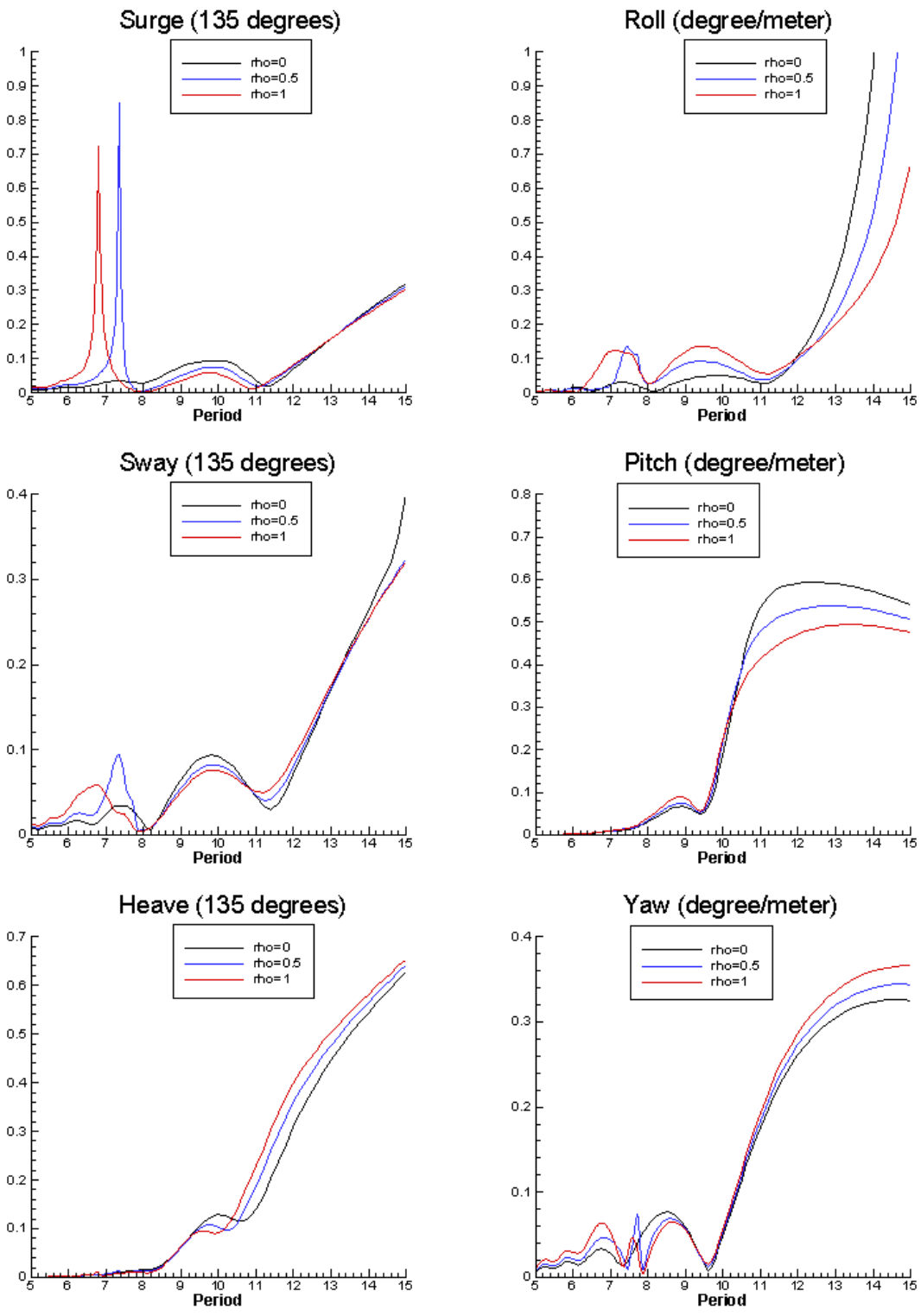

Figure 15: RAO's of the generic FPSO hull in bow waves ($\beta = 135^o$).

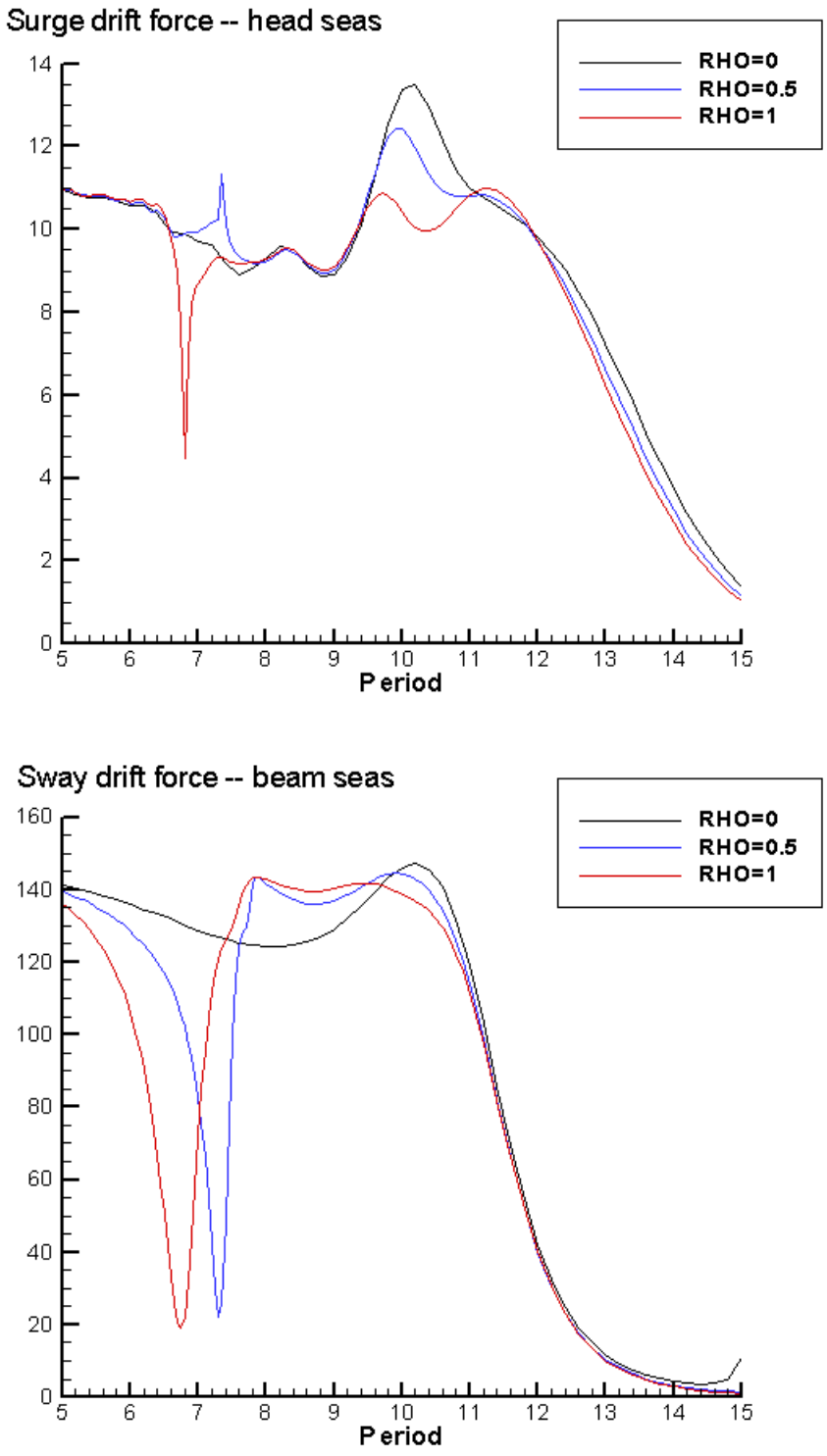

Figure 16: Drift forces of the generic FPSO hull in head waves (top) and beam waves (bottom).

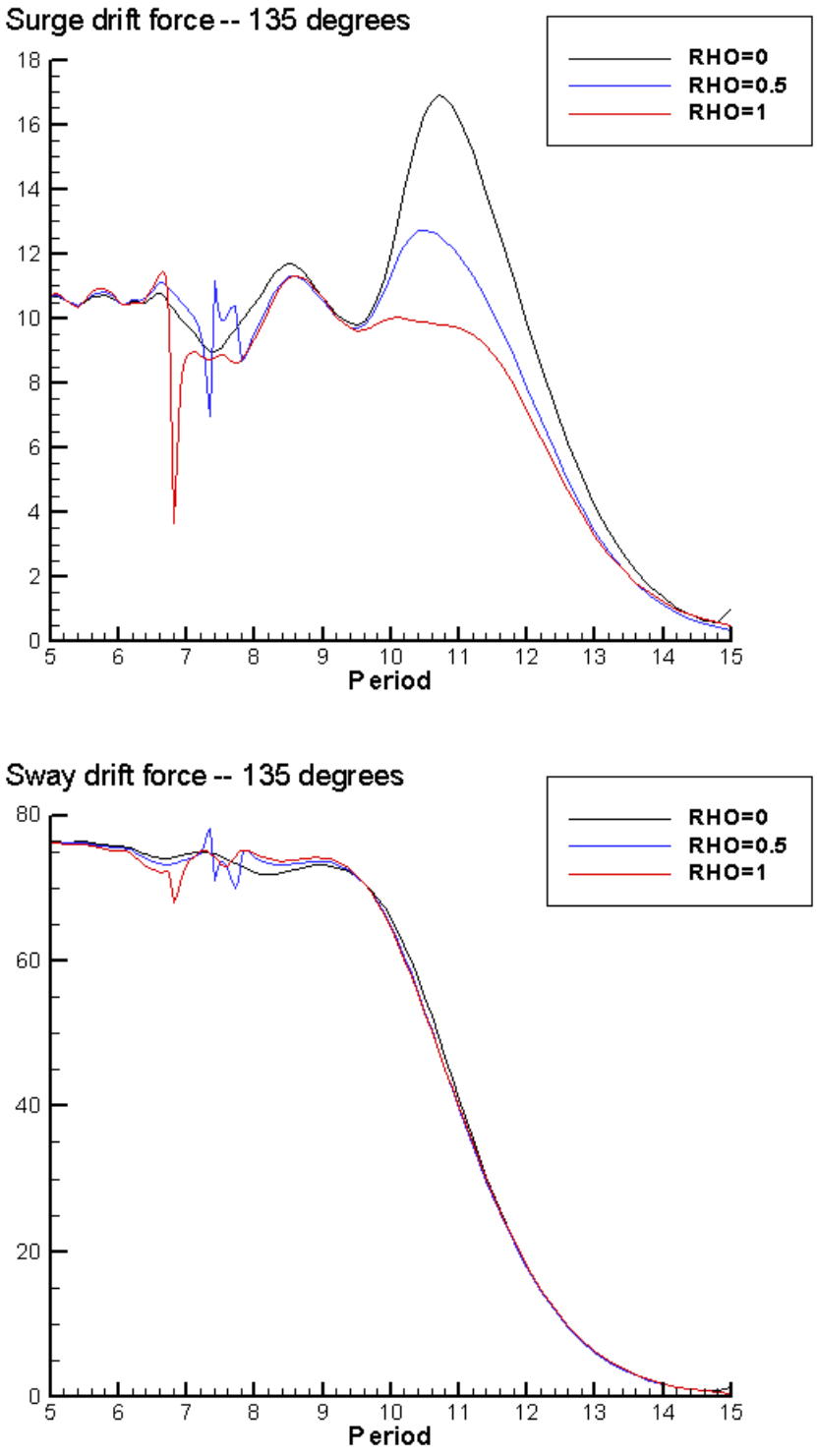

Figure 17: Drift forces of the generic FPSO hull in bow waves ($\beta = 135^o$).

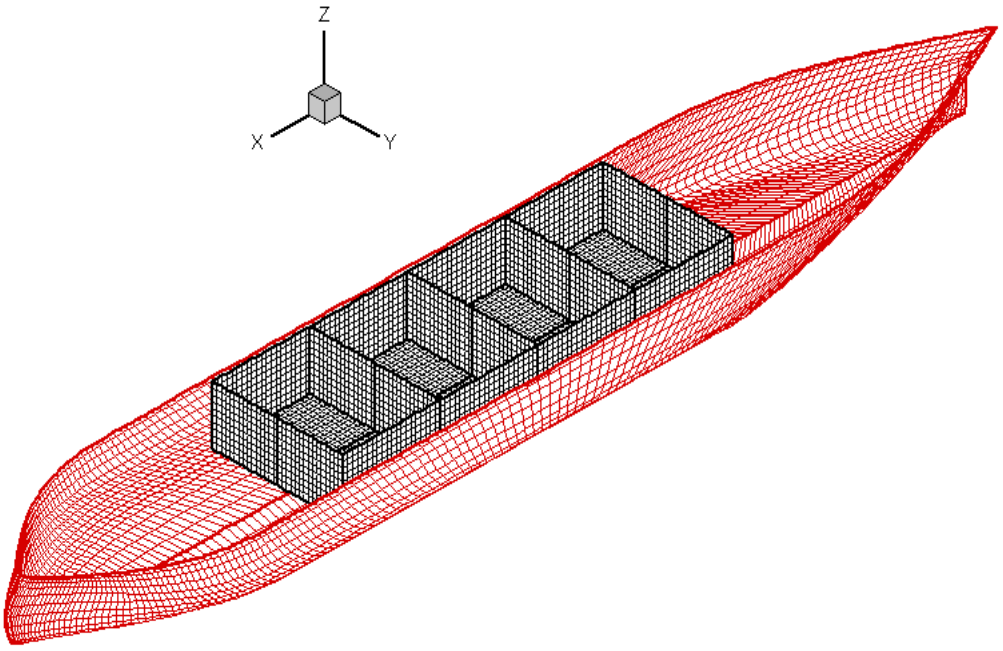

Figure 18: Perspective view of the prototype FPSO hull with four internal tanks. The principal dimensions of the hull are 300m long, 50m beam, and 15m draft. Each tank is 30m long, 40m width, and 15m deep, with the free surface 3m above the exterior free surface and the tank bottom 12m below the exterior free surface. The tanks are located between x=+75m to x=-45m, where x=±150 are the coordinates of the bow and stern, respectively.

‘

5 Prototype FPSO

This hull form is generated using the MultiSurf interface with WAMIT. The original MultiSurf model for the hull was developed by Dr. John Letcher of AeroHydro, Inc. The tanks were added to this model. The parameter Panel_Size=5 was used, and convergence was verified by performing computations at a limited set of wave periods with Panel_Size=2.5 . For the momentum drift forces the two sets of results are graphically identical. For the sway drift force the momentum and pressure drift forces are practically identical, but for the surge drift force there are substantial differences, with the pressure forces smaller than the momentum forces at all wave periods. This may be associated with the flared stern of this vessel.

For these computations VCG=4.0m, k_x=15m, and $k_y = k_z$=75m.

REFERENCES

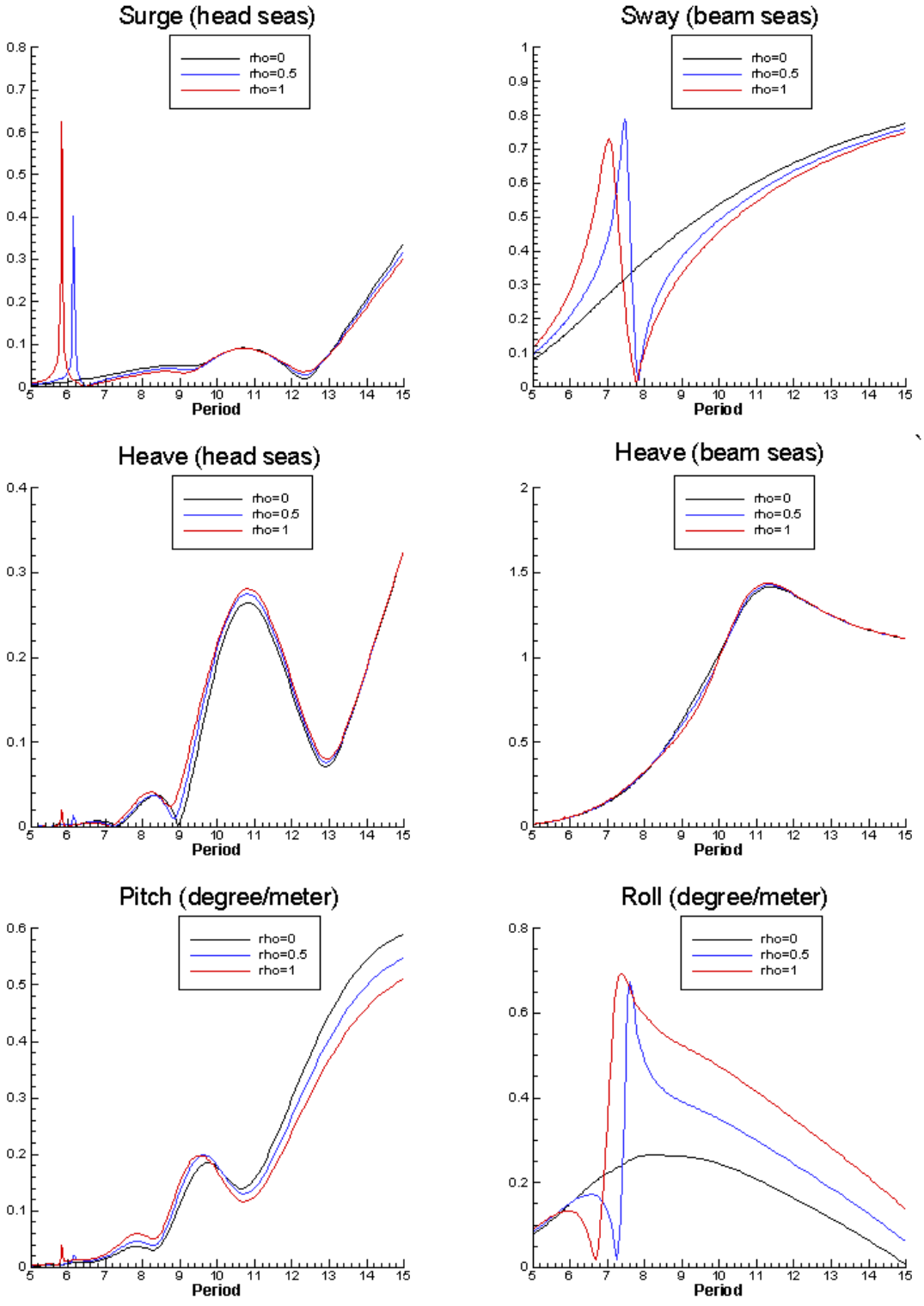

Figure 19: RAO's of the prototype FPSO hull in head waves (left) and beam waves (right).

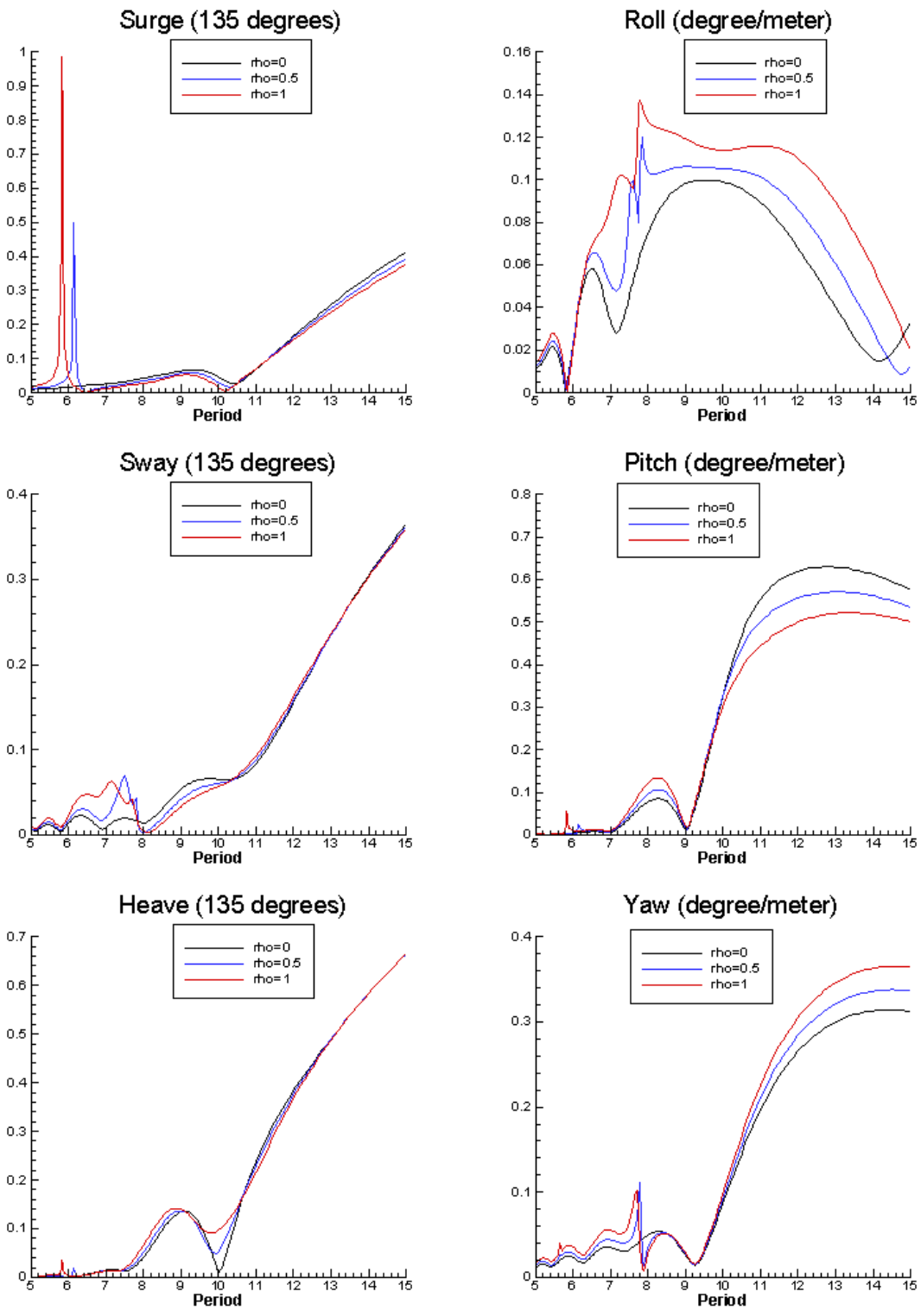

Figure 20: RAO's of the prototype FPSO hull in bow waves ($\beta = 135^o$).

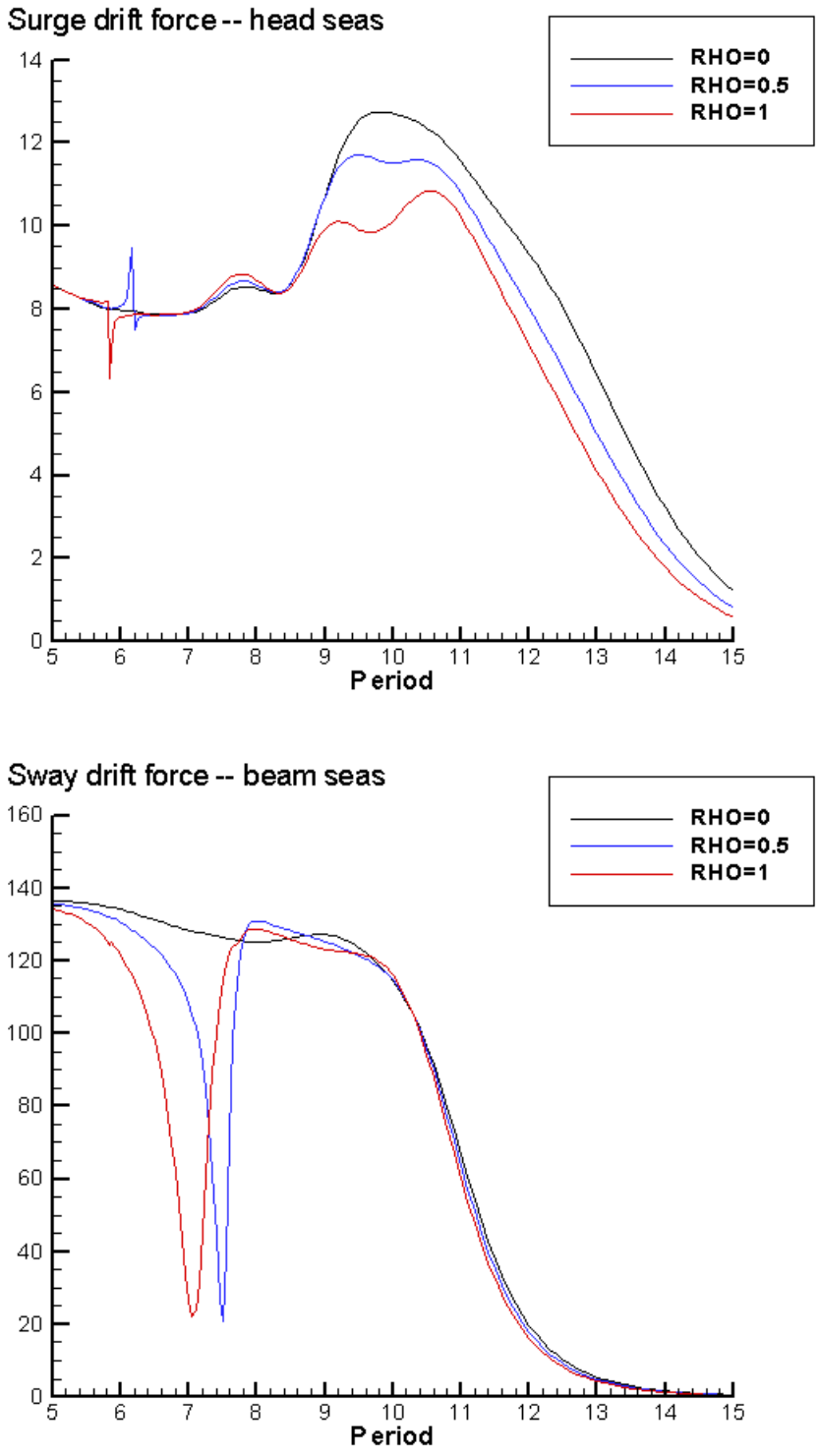

Figure 21: Drift forces of the prototype FPSO hull in head waves (top) and beam waves (bottom).

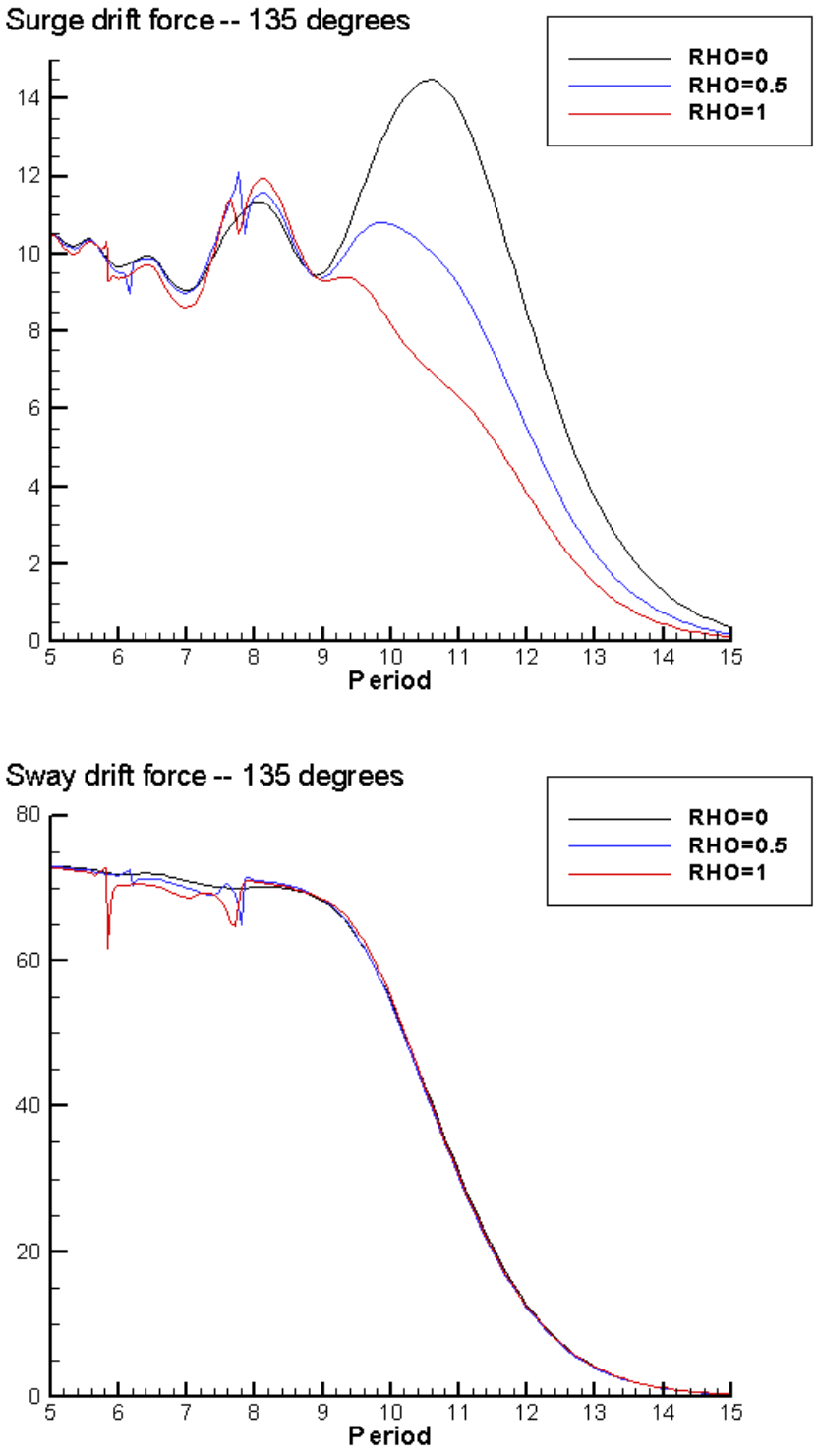

Figure 22: Drift forces of the prototype FPSO hull in bow waves ($\beta = 135^o$).

Kim, Y., 2001, 'Coupled analysis of ship motions and sloshing flows,' 16th International Workshop on Waves and Floating Bodies (IWWWFB), Hiroshima, Japan (downloadable from *http://www.rina.org.uk/showarticle.pl?id=6330&n=560*)

Lee, C.-H. & Newman, J. N., 2004, 'Computation of wave effects using the panel method,' to be published in *Numerical Modeling in Fluid-Structure Interaction,* Edited by Subrata Chakrabarti, WIT Press (downloadable from <http://www.wamit.com>)

Malenica, Ŝ., Zalar, M. & Chen, X. B. 2003, 'Dynamic coupling of seakeeping and sloshing,' Paper No. 2003-JSC-267, ISOPE.

Molin, B., Remy, F., Rigaud, S., & de Jouette, Ch., 2002, 'LNG-FPSO's: frequency domain, coupled analysis of support and liquid cargo motions,' Proceedings IMAM Converence, Rethymnon, Greece.

Rognebakke, O. F. & Faltinsen, O. M., 2001, 'Effect of sloshing on ship motions,' 16th International Workshop on Waves and Floating Bodies (IWWWFB), Hiroshima, Japan (downloadable from <http://www.rina.org.uk/showarticle.pl?id=6330&n=560>)

Rognebakke, O. F. & Faltinsen, O. M., 2003, 'Coupling of sloshing and ship motions,' *J. Ship Research,* **47**, 3, 208-221.

OMAE 2004, Vancouver

Progress in wave load computations on offshore structures

by J. N. Newman

jnn@mit.edu

Computational methods for predicting wave effects have obvious importance for the design and operation of offshore structures. The available tools range from simplified theories, and codes with restricted applications, to cutting-edge Navier-Stokes solvers which seek to account for all relevant viscous and nonlinear effects. It would be most valuable to survey this entire field, but given the restrictions of time and my own experience, I cannot do that in this lecture.

Instead I will focus on the use of the panel method, sometimes known as the boundary integral equation method or boundary element method. This occupies a central position in the prediction of wave effects on large offshore structures, since it can be applied to a wide variety of practical applications, with sufficient confidence that it can be used by practitioners, not just by researchers. On the other hand we must keep in mind that panel methods are generally restricted by the assumptions of linear potential flow, although I will show some examples where we can take one or two steps beyond these strict limits.

3D linear computations

1970-1980

- Panel methods (after Hess and Smith) Halkyard/Milgram, Garrison, Hogben/Standing, v.Oertmerssen, Faltinsen/Michelsen
- FEM Bai,Yue/Chen/Mei/Aranha, EatockTaylor/Wu

This list includes some of the pioneers on the computation of wave loads. The 3D panel method was first developed by Hess and Smith at the Douglas Aircraft Company. The name came from their representing the body surface by a large number of small flat quadrilateral `panels'. This approach was extended by several groups to include free surface effects. The early programs were very slow, and some attention was also given to finite-element methods where the entire fluid domain was discretized, but subsequent refinements of the panel method have largely superseded the FEM activity.

The TLP challenge

1979-1991

- 2nd order (Molin, Lighthill, Kim/Yue)
- Improved 1st order (linear) panel method Fast Green function algorithms, iterative solvers (Korsmeyer et al, OMAE `88)
- 2nd-order codes (Chau/Eatock Taylor, Chen et al (BV), C-H Lee et al (MIT)

TLP's presented a number of challenges, regarding more efficient computation of linear solutions and the need to consider second-order nonlinearities. This led to many advances, so that by the early 1990's the use of panel methods was more universal and useful.

recent developments

- higher-order panel methods
- exact geometry
- CAD coupling
- Accelerated solver O(N log N)
- Viscous post-processor

Recent developments which I will discuss include higher-order panel methods, and more exact and convenient representations of the geometry. Also the development of accelerated solvers which are essential for extremely large complex structures, and coupled solutions of the potential and viscous problems.

Examples of Applications and Results

- Spar with strakes and moonpool
- Drill ship with three moonpools
- Damping of gap resonance between hulls
- Linear coupling with internal tanks
- VLFS (Mat structure and cylinder array)
- Slowly-varying 2^{nd} order drift force
- Navier-Stokes post-processor (VISCOR)

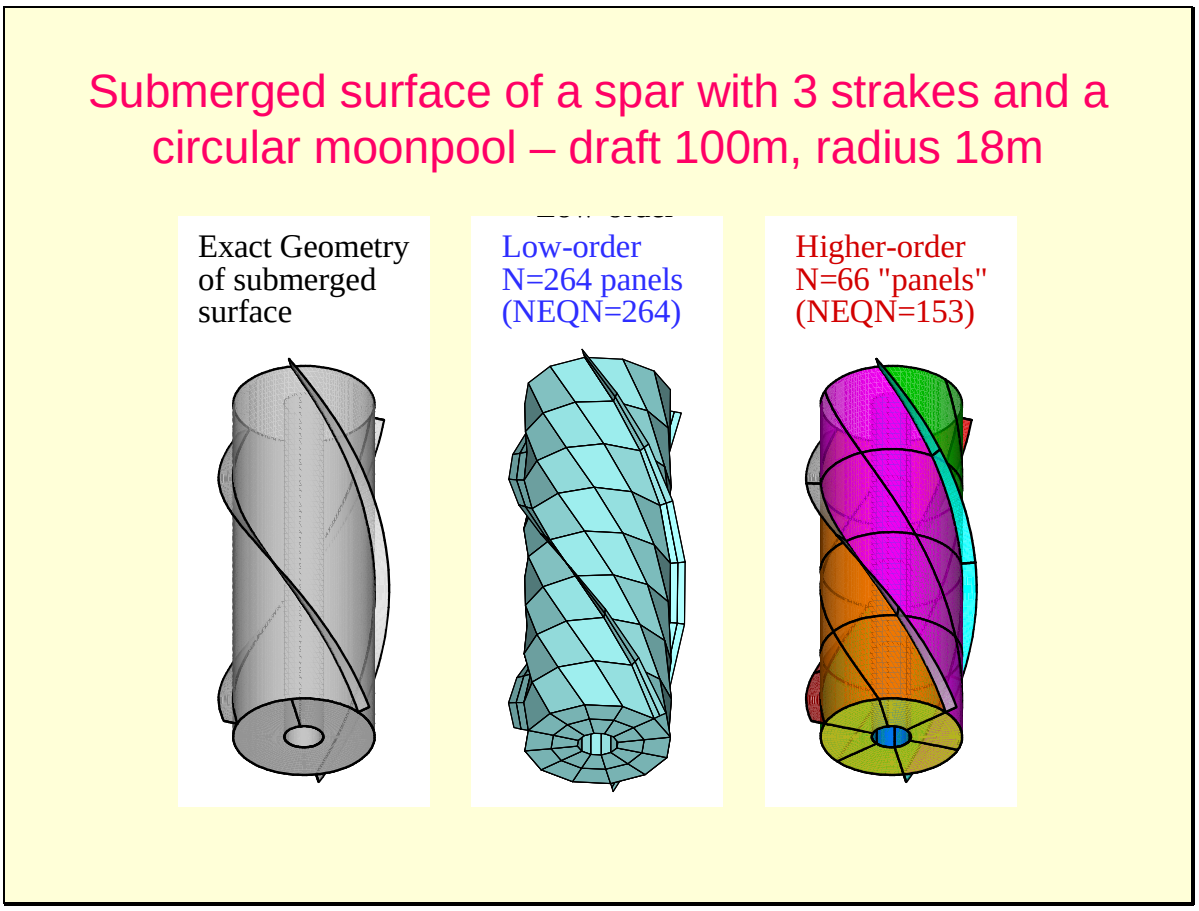

This figure shows the submerged portion of a spar, consisting of a cylindrical hull with a concentric moonpool and 3 helical strakes. The left figure shows the exact geometry. The middle figure illustrates its representation in the low-order panel method, where the surface is approximated by quadrilateral flat panels and the solution for the potential or source strength is constant on each panel. The right-hand figure illustrates the higher-order method, where the surface is subdivided into eight `patches', indicated here by different colors. The basic requirement is that the surface should be smooth and continuous on each separate patch. The geometry on each patch is mapped onto a rectangular parametric surface. In most practical applications this mapping is effectively exact, so there is no approximation of the geometry. The velocity potential is represented in each parametric space by continuous basis functions with unknown coefficients, and the solution for these coefficients is computed in a manner which is fundamentally similar to the low-order method. To control the accuracy of the solution, the parametric coordinates can be subdivided, as indicated by the black lines in the right figure. We use B-splines to represent the solution, and increasing the number of subdivisions is equivalent to adding knots and control points to the B-splines.

The principal advantages of the higher-order method are that it gives a more accurate and efficient representation of the solution, and the only significant numerical approximation is in the solution itself, which can be controlled by increasing the number of subdivisions in the parametric space. This approach also circumvents the work of discretizing or panelling the body.

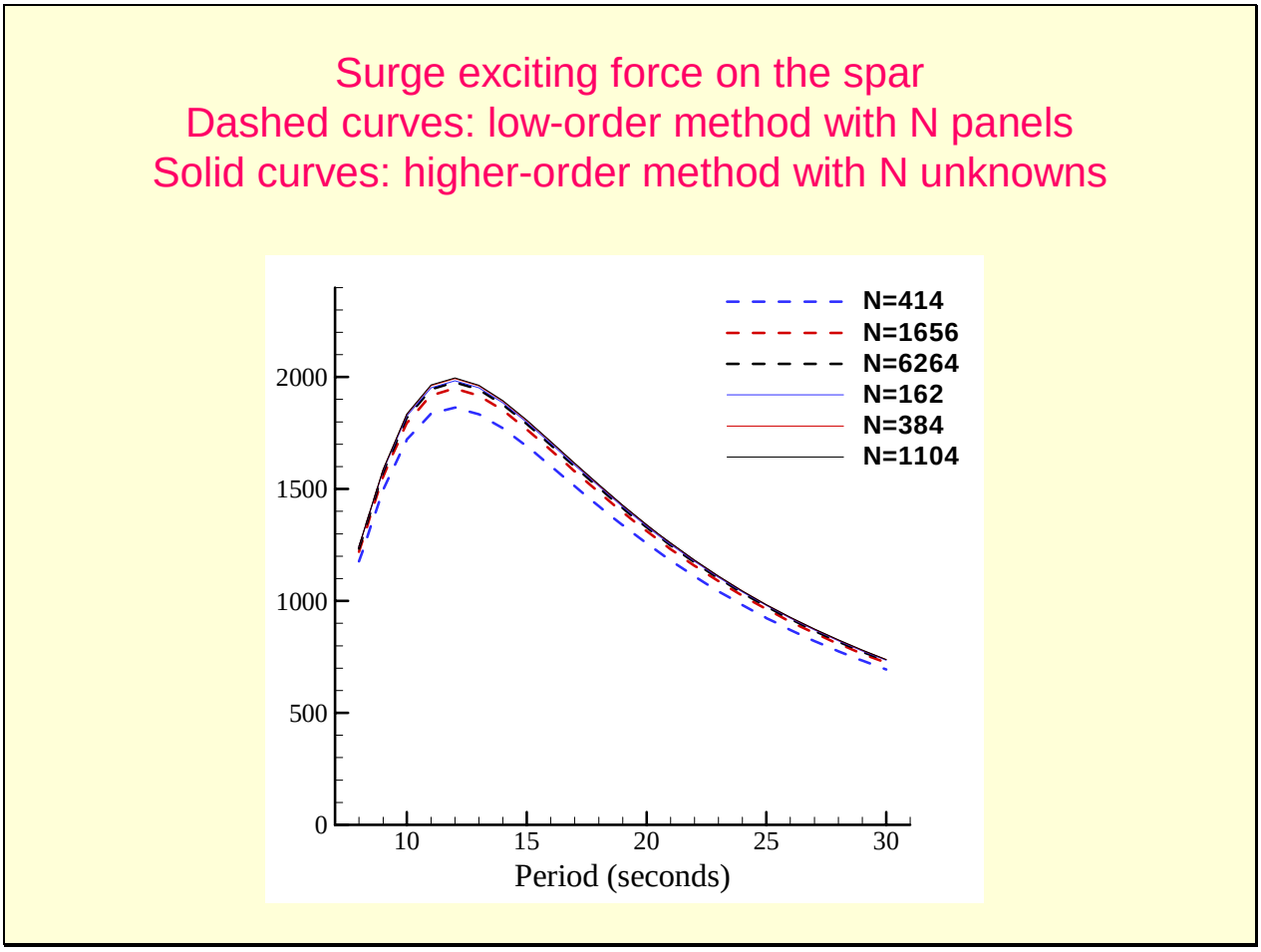

This figure shows the surge exciting force on the spar, plotted against the wave period. Results using both the low-order and higher-order methods are shown, with increasing numbers of unknowns to refine the accuracy. The convergence is apparent as the number of unknowns is increased, and the accuracy of both results can be judged by the extent to which they change with increasingly fine discretizations. Note that the accuracy of the coarsest higher-order discretization, with N=162, is comparable to the accuracy of the finest low-order discretization, with N=6264.

Yaw exciting moment on the spar
Dashed curves: low-order method with N panels
Solid curves: higher-order method with N unknowns

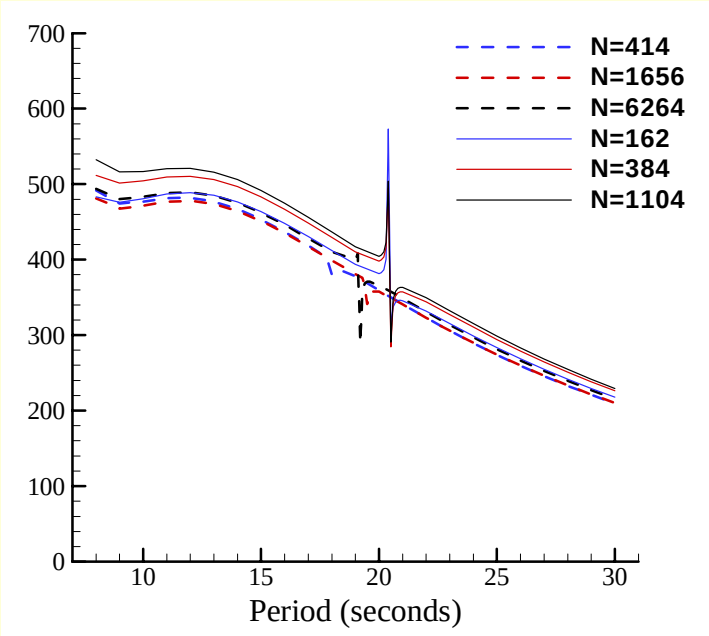

This figure shows the yaw moment, which is relatively small, since the strakes are the only surfaces which contribute. The singular feature near 20 seconds is due to the moonpool pumping mode resonance, which causes a large axisymmetric flux in and out of the moonpool. This has no noticeable effect on the surge force, but the induced exterior flow past the strakes produces a yaw moment.

Linear damping of the pumping mode using a `lid' (heaving piston) in place of the moonpool free surface with an added damping force D applied to the lid

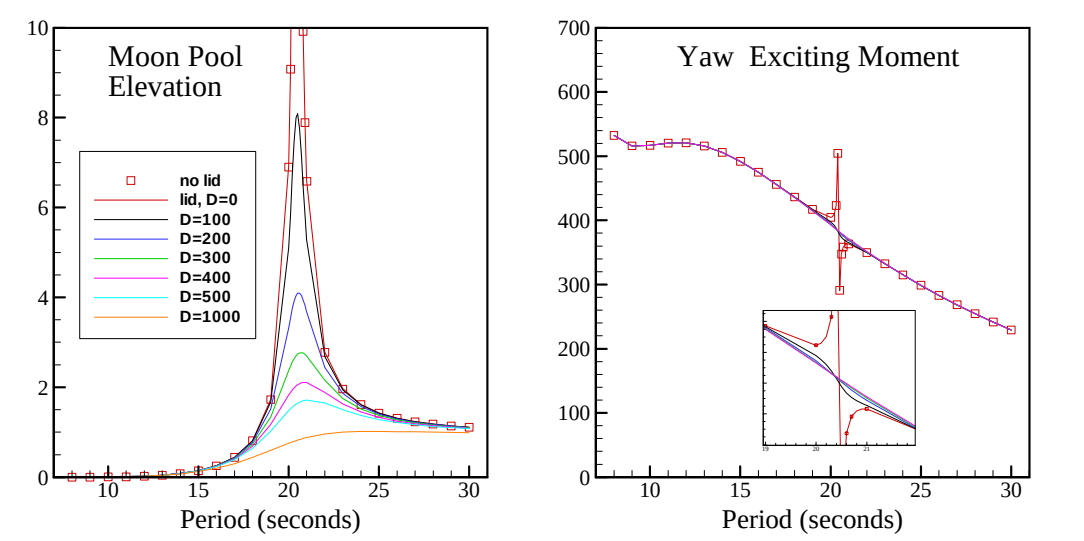

We have adopted a technique for adding fictitious damping by replacing the physical free surface of the moonpool by a lid, or heaving piston. If the lid is free to heave, without external restraints, it acts just like the free surface. The left figure shows the moonpool elevation, normalized by the incident-wave amplitude. The linear solution with a free surface in the moonpool is shown by the square symbols, and the red line shows separate computations where the free surface is replaced by a heaving lid. The response is unrealistically large near the resonant period, where damping associated with viscous flow and separation is important. Adding a fictitious linear damping coefficient D on the lid gives the curves shown with lower resonant amplitudes. An appropriate value of the damping coefficient can be estimated from experimental or full-scale observations of the peak elevation in the moonpool. The corresponding results for the yaw moment are shown in the right figure, where even a small amount of damping is sufficient to attenuate the singularity.

Representing the free surface by a simple heaving lid with only one degree of freedom is feasible here because the moonpool cross-section is small, and only the pumping mode is relevant within the indicated range of wave periods. Additional degrees of freedom can be included when `sloshing' modes are relevant.

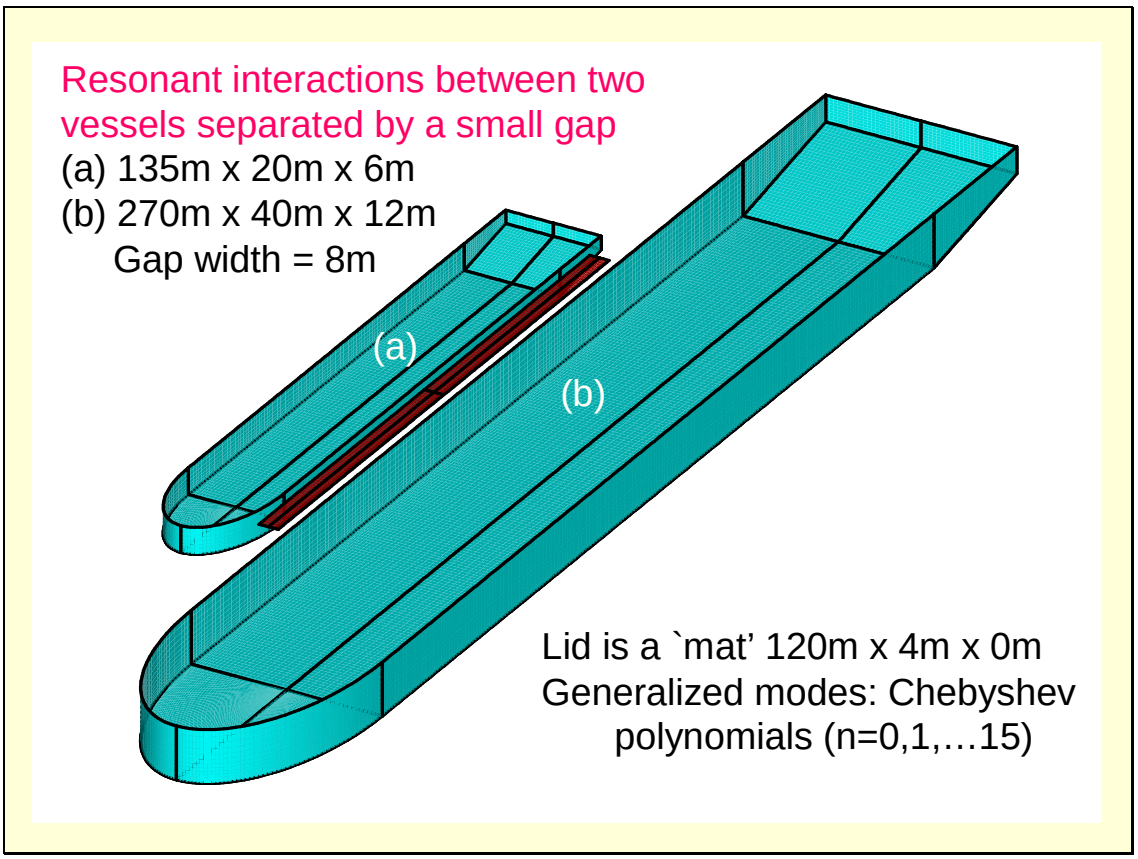

The panel method can be used for multiple bodies with complete analysis of their interactions, in effect by considering their separate surfaces to be sub-portions of one larger surface, and by increasing the number of degrees of freedom. In this case, with two independent vessels, there are a total of 12 degrees of rigid-body motion. One interesting complication is the occurrence of resonances of the free surface elevation in the gap. These are similar to the moonpool pumping resonance, but with wavelike longitudinal oscillations along the gap. As in the case of the moonpool, the gap resonances magnify the forces acting on the two vessels, and it is necessary to simulate the additional damping due to viscous effects and separation. In this example a flexible lid has been added in the gap, shown by the red patch on the free surface. It is not necessary for the lid to cover the entire gap, only a sufficient portion so that it is physically able to damp the relevant resonant modes. Thus a simple rectangular lid can be used even when the gap width is variable, and the positions of the fore and aft ends of the lid are somewhat arbitrary.

The vertical motion of the lid can be represented by an appropriate set of basis functions. For this example we have used 16 orthogonal Chebyshev polynomials. Thus there are a total of 28 degrees of freedom, 6 for each vessel and 16 for the lid modes.

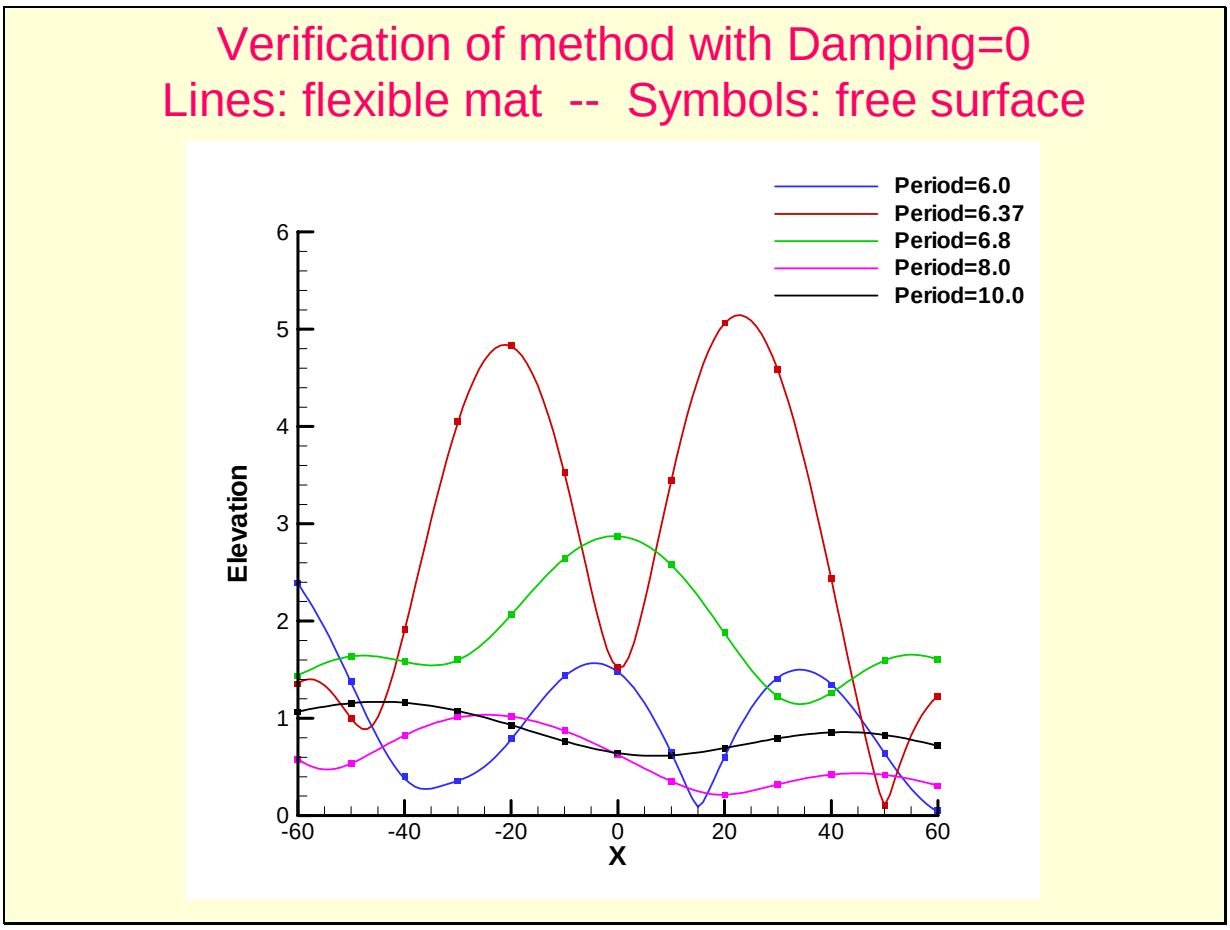

Here the use of the flexible lid is verified. The curves show the deflection of the lid, without damping, as a function of the longitudinal position X. The symbols show the more conventional computations of the free-surface elevation in the gap, without a lid. The computed results are practically identical. Five wave periods are shown, ranging from 6 to 10 seconds. The largest amplitude occurs at 6.37 seconds, represented by the red curve, with peak values about 5 times the incident-wave amplitude.

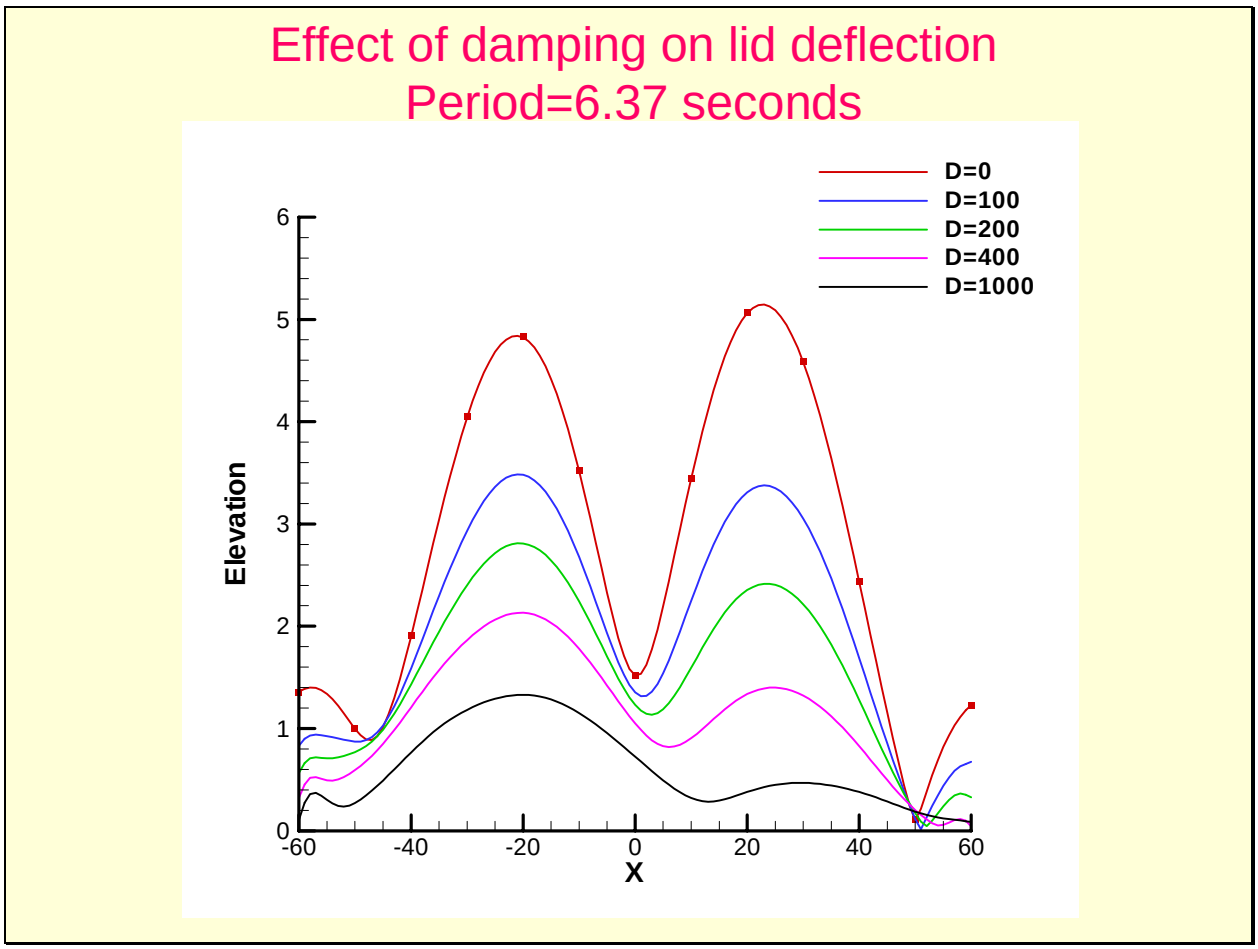

This shows the results for the peak period of the gap resonance, for a range of increasing damping coefficients. The elevations at the longer wave periods are not affected significantly.

Navis Explorer I with 3 moonpools
Geometry definition from MultiSurf/RGKernel interface (higher-order method)

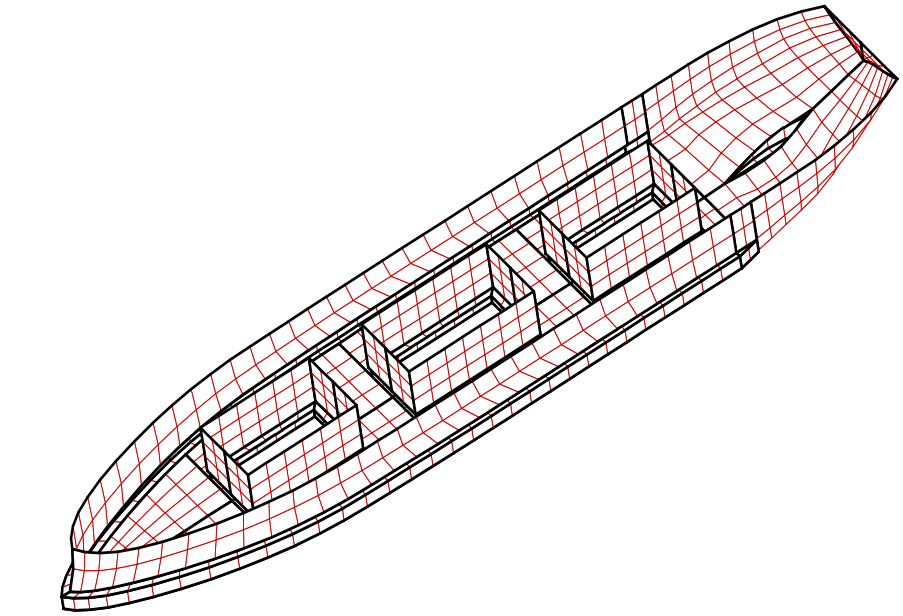

In regard to the geometry, one can either describe this analytically, with appropriate equations, as was done for the two previous examples, or one can use a CAD program. In our paper two years ago at the Oslo OMAE I described in some detail how we have interfaced the CAD program MultiSurf with the higher-order solution in WAMIT, so that there is no need for an intermediate geometry file to be prepared by the user. That approach is illustrated here for a drillship which has 3 large moonpools.

Moonpool elevations compared to experiments
Red curves are computations with damped lids
Black curves are experiments (MARINTEK)
Hs=Significant Wave Height in meters

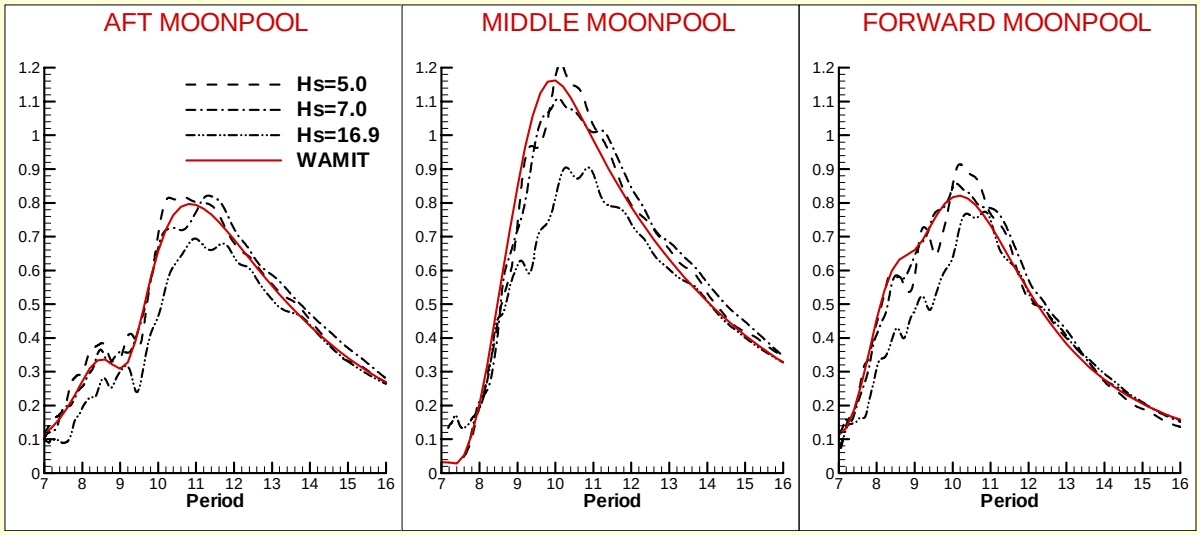

This shows the comparison between experimental data and computations for the moonpool elevations, with damped lids used for the computations. The elevations are normalized by the incident-wave amplitude. A single constant damping coefficient for the lids was selected to match the peaks.

Three different sea states were used in the experiments, including the severe case with significant wave height 16.9m. Nonlinear effects are evident here, with smaller relative elevations in the highest sea state. Improved comparisons would probably result from the use of a stochastic linearization of the damping, so that larger lid damping coefficients are applied in the more severe sea states.

Heave and Pitch RAO's, compared to experiments (MARINTEK)

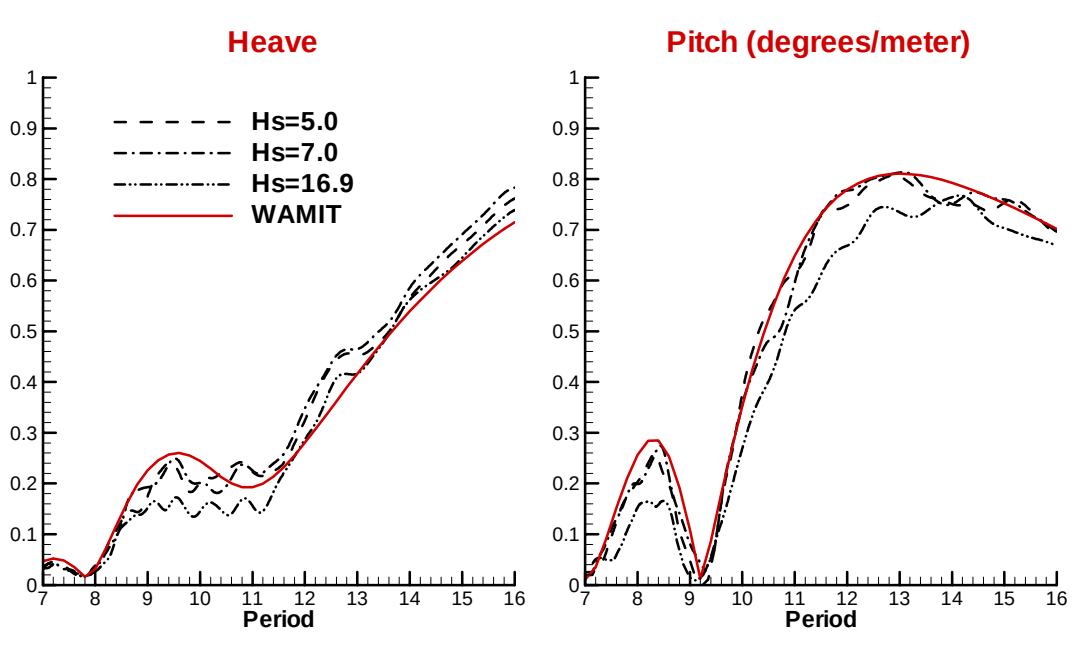

This shows the comparison between experimental data and computations, for the heave and pitch. The same damped lids are used for the computations. There is remarkably little difference between the RAO's in different sea states, indicating that nonlinear effects are not so important for the heave and pitch motions of the vessel.

Coupled motions of an FPSO with four internal tanks

FPSO 300 x 50 x 15m
tanks 30 x 40 x 15m

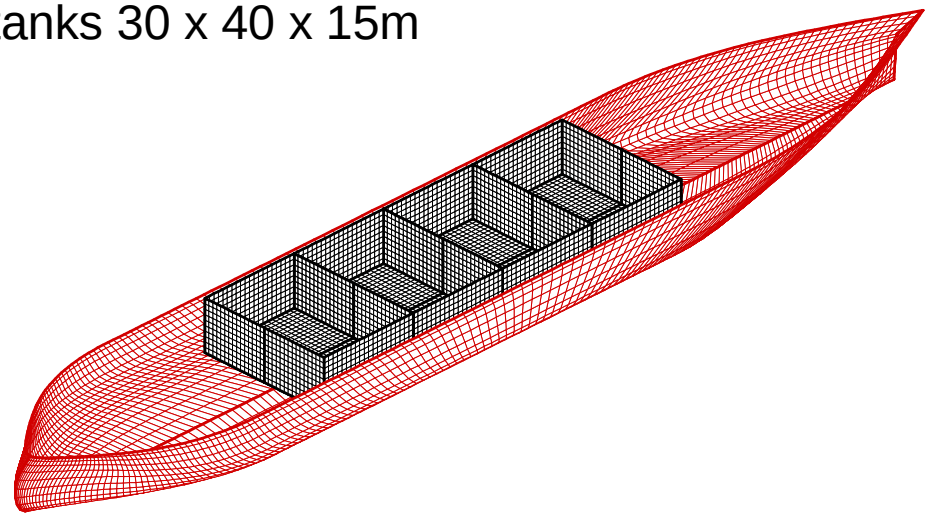

This slide shows an FPSO with four internal tanks. The objective is to compute the coupled motions of the vessel, including a linear analysis of the dynamic effects of the fluid in the tanks.

For this application the geometry was generated using MultiSurf, including both the exterior wetted surface of the hull (red) and the interior wetted surfaces of the four tanks (black). Each tank has a free surface, level with the top edge of its wetted surface. The elevation of each free surface can be different.

For this application we use the panel method to compute one simultaneous solution of all five fluid regimes, with the interior tank surfaces added to the exterior hull surface. The principal modification required for the tanks is to enforce the condition that there is no hydrodynamic interaction between each tank and the exterior domain, or between different tanks. One advantage of this approach is that all of the various hydrodynamic output parameters, such as free-surface elevations and drift forces, can be computed in the same way as in the conventional analysis of vessels without tanks.

Free-surface elevation in tanks near forward corner
Solid lines: head seas – Dashed lines: beam seas
Arrows: natural periods of 1st sloshing modes in tanks

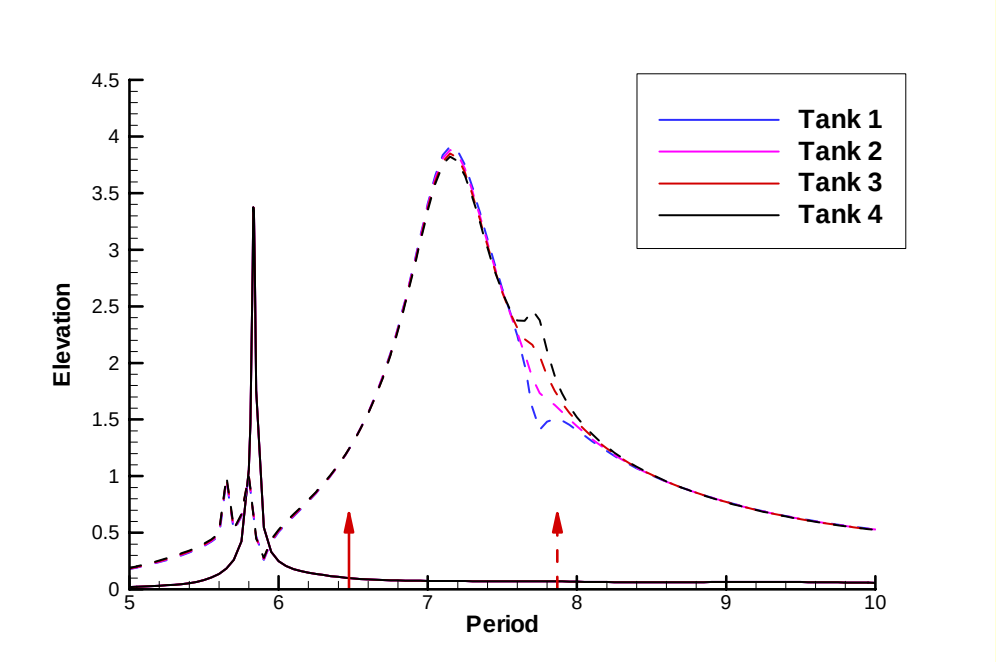

This shows the free-surface elevations in the four tanks, in head seas and in beam seas. The elevations are practically the same for all four tanks. The peaks occur at a period just below 6 seconds for surge motion of the ship, and above 7 seconds for sway and roll. The corresponding natural periods for standing-wave resonance in the tanks are indicated by the vertical red arrows. The downshift of the peak periods by about half a second is due to the coupling between the tanks and the dynamics of the vessel. The smaller peaks in beam seas at 5.6 – 5.8 seconds correspond to the 1st sloshing mode which is antisymmetric in both x and y, and may be associated with small yawing motions of the ship.

Sway/Roll RAO's in beam seas

rho = relative density of fluid in tanks

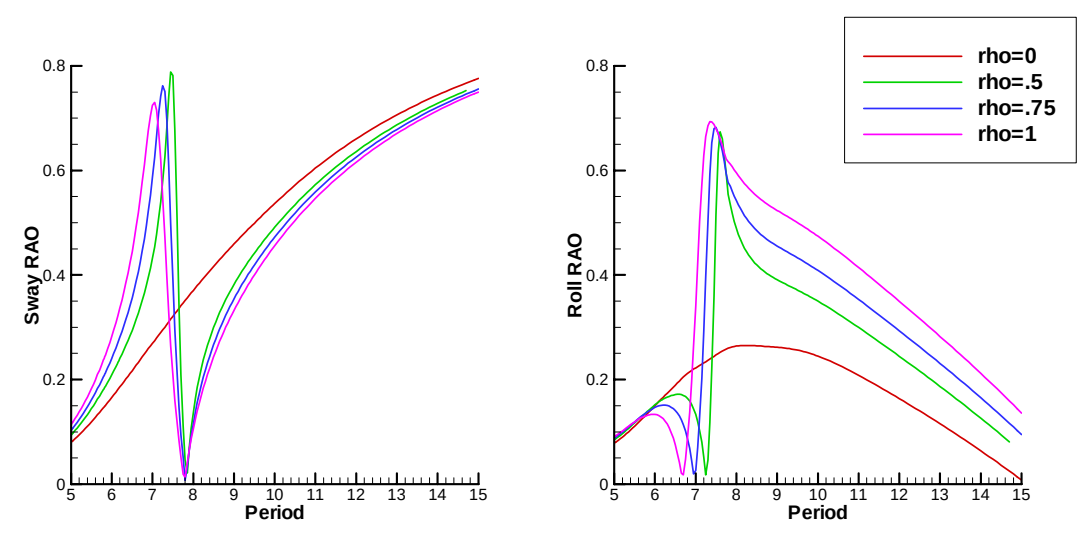

Here we see the sway and roll response of the FPSO in beam seas, for several different densities of the tank fluid. The total displacement is the same in all cases. The red curves, for zero density, are equivalent to the case where there are no tanks. Rapid variations occur near the sloshing resonance, and to account correctly for this regime it would be necessary to perform a nonlinear analysis of the tank dynamics, but even this linearized analysis demonstrates the strong influence of the tanks on the global response of the vessel.

Experimental validation for a barge with two internal tanks

Barge 3m x 1m x .108m, tanks .25 x .8 x 19cm, 39cm deep

Experiments and Computations by Molin et al, IMAM 2002

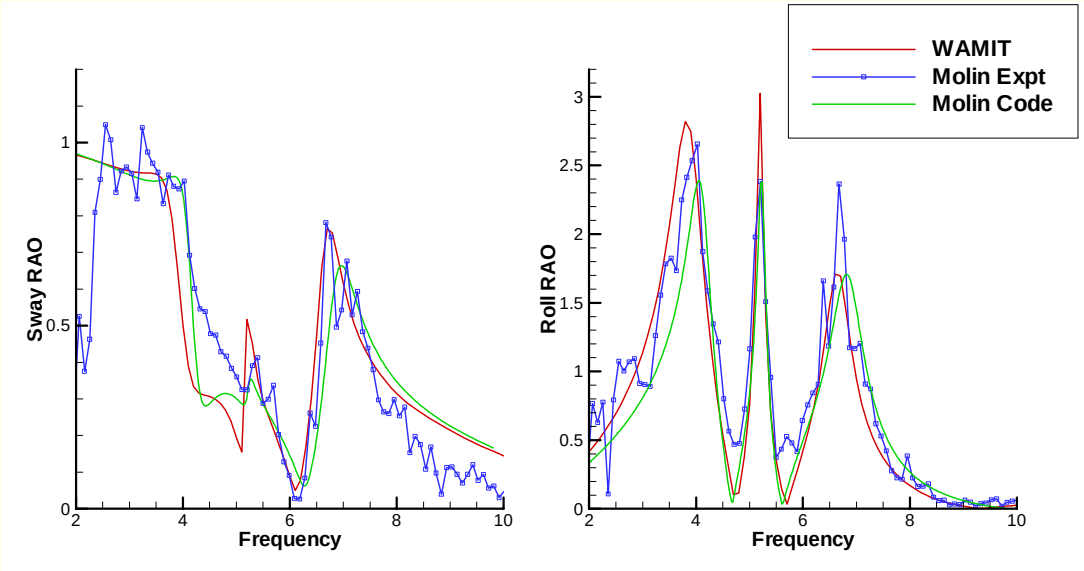

In this slide a comparison is made with the experiments and computations reported by Molin et al (IMAM, 2002), for a rectangular barge with two tanks. For the case shown here the tank depths are quite different, and thus there are two distinct sloshing resonances which are most evident in the right figure for the roll response. The blue symbols denote the experimental data, the green curves are Molin's computations where the tank and vessel dynamics are analysed separately and superposed in the equations of motion, and the red curves are our computations carried out as I described earlier. The principal difference between the two computations is that we have used a constant linear added damping coefficient in roll, whereas Molin et al used a statistical linearization procedure. Similar computational results have also been reported by Malenica et al (ISOPE 2003) using separate analysis of the tanks and vessel.

Very Large Floating Structures (VLFS/MOB)

Example 1 -- Mat-type barge, 4km x 1km x 5m draft

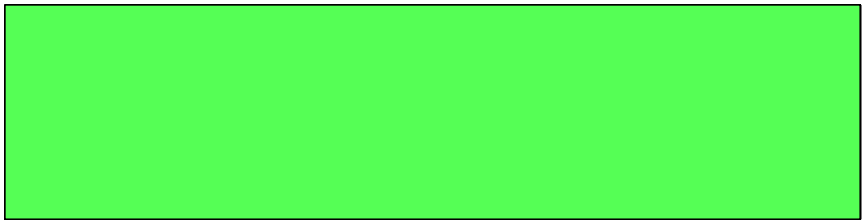

Example 2 -- Array of 100 x 25 = 2500 circular cylinders
Radius=11.5m, Draft=20m, Axial spacing = 40m

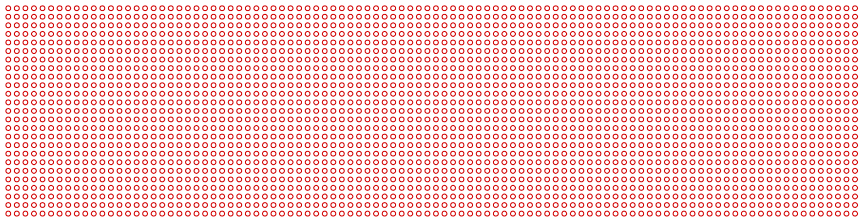

One of the most challenging applications of wave-body computations is in the very large floating structures (VLFS), including Mobile Offshore Bases (MOB), and floating airports. Two different types have been studied, as shown here in planform views. The mat type shown in green is like a rectangular barge with very shallow draft. The alternative configuration shown in red is an array of 2500 circular cylinders. In both cases the horizontal dimensions are 4km by 1km, and the total displacements are the same.

Example 1 -- Drift forces on the rectangular barge

Wave incidence angle 45^{o} -- Water depth = 50m

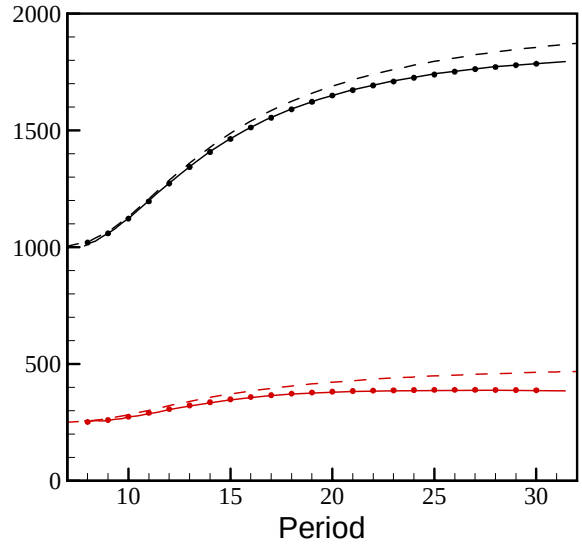

Red: Surge drift force
Black: Sway drift force
- higher- order method (727 unknowns)

Solid lines: Accelerated pFFT method with 43,000 low-order panels
Both methods take about 0.4 hour/period on a 2GHz PC
Dashed lines: Asympototic approximation for short wavelengths

This shows the horizontal drift forces for the first example, in a water depth of 50m which is very shallow compared to the horizontal dimensions of the vessel. The solid curves are computed using the Accelerated pFFT method, with 43,000 low-order panels. The points are evaluated using the higher-order method. The computational cost is about the same for both methods, for this scale of problem. The dashed curves are based on simple short-wavelength approximations, assuming complete reflection along the end and side of the structure. For this type of structure that approximation is very useful.

Hydroelastic effects are important to consider. These can be analysed by adding a suitable number of bending modes to represent the vertical deflection of the barge, and solving the extended equations of motion including the linearized structural-response coefficients.

Example 2 -- Drift forces on the 100x25 Cylinder Array

Wave incidence angle 45^o -- Water depth = 50m

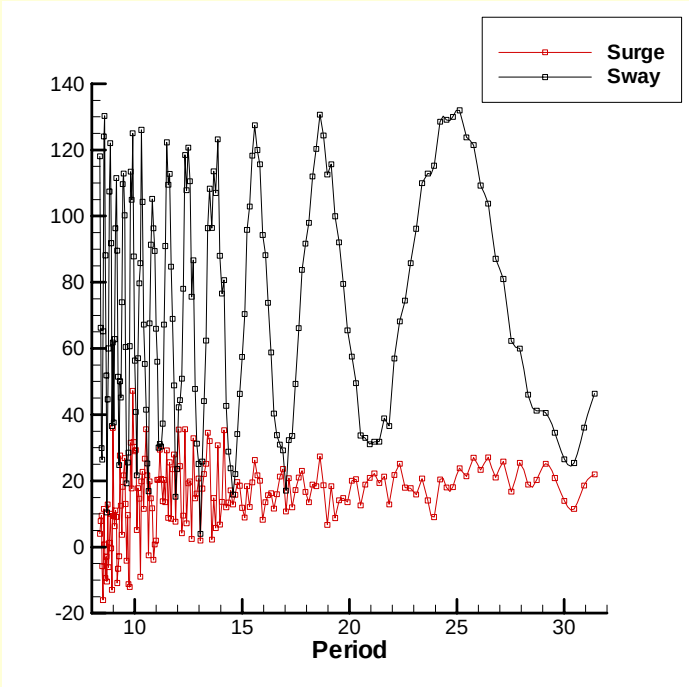

240,000 low-order panels were used here (96 on each cylinder).

These computations were performed on a 2.6GHz PC using the accelerated pFFT method (`precorrected Fast Fourier Transform'). The CPU time averaged about one hour per period.

The peak magnitudes are much larger below 8 seconds, where near-trapping occurs between adjacent cylinders.

This shows corresponding results for the array of 2500 cylinders, represented by 240,000 low-order panels. In this case the number of unknowns N is too large for the conventional approach, where the CPU time is proportional to N^2 or N^3. Instead we use the accelerated pFFT method, where the CPU time is proportional to (N log N). With this approach it is possible to solve problems of this complexity, even with a PC.

There is obviously a strong variation due to constructive and destructive wave interactions among the elements of the array. At shorter wave periods below eight seconds near-trapping occurs, with larger oscillations.

2nd order slowly-varying drift force on FPSO

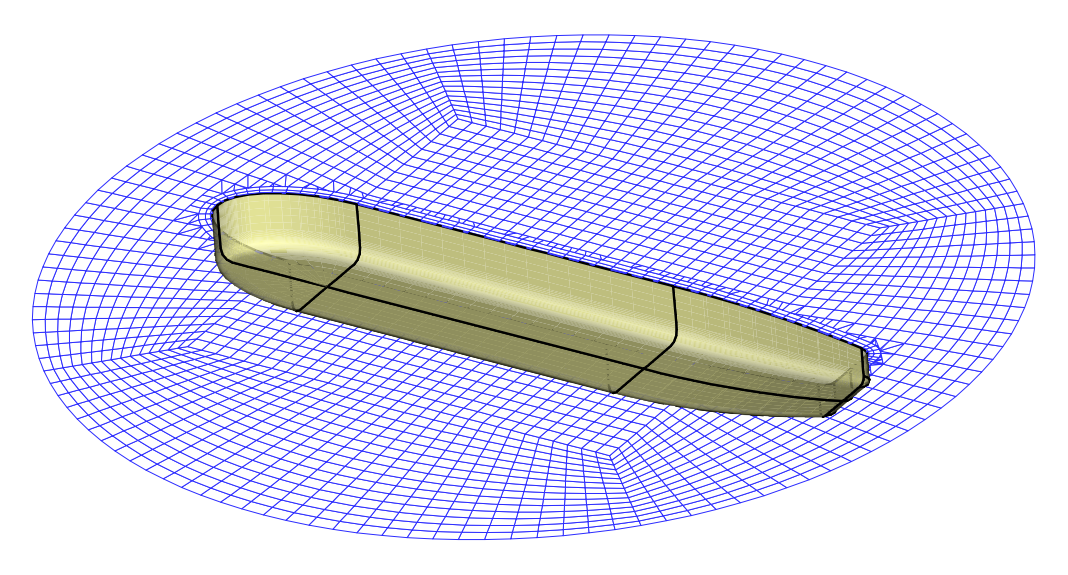

This application involves the slowly-varying drift force acting on an FPSO. To describe this phenomenon completely requires that we solve the second-order problem for the velocity potential. The complete solution is complicated by the fact that there is an inhomogeneous free surface boundary condition, corresponding to the forcing all over the free surface due to second-order wave interactions. Thus one must discretize not only the body surface, but also the free surface, over a very large computational domain. Further complicating this task is the fact that the computations must be repeated for all relevant combinations of the first-order wave frequencies and heading angles.

Slowly-varying 2nd order Sway Force on FPSO (including the complete 2nd order potential)

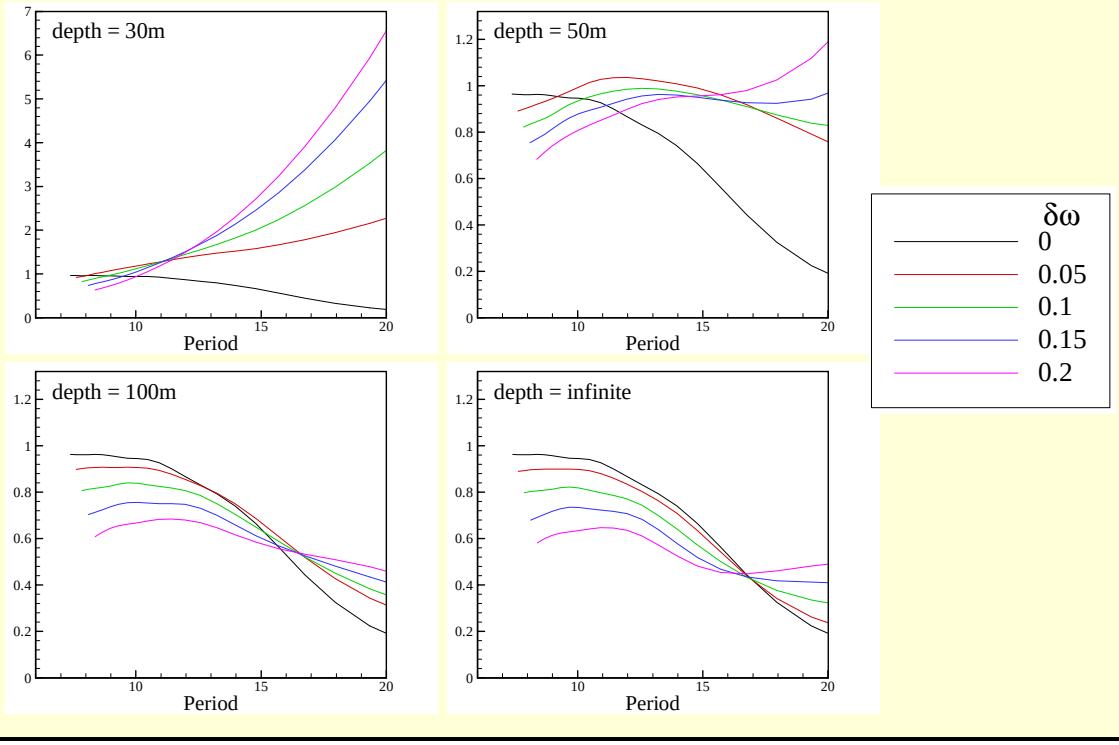

This shows the complete results, for the slowly-varying second-order sway force in beam seas. Four different depths are included since the effect of shallow water is especially important here. The plots show the amplitudes of the quadratic transfer functions, including only the difference-frequency components which contribute to low-frequency forcing. The horizontal scales are the mean wave periods, which are derived from the mean frequencies of the two incident wave components. The colored lines correspond to different values of the difference between the two frequencies, as shown in the legend on the right. The black curves are for zero difference-frequency, equivalent to the mean drift force in monochromatic waves. Note that the vertical scale is changed in the first plot, for a depth of 30m, and the slowly-varying forces in this case are much larger for wave periods above 10 seconds.

In the analysis of slowly-varying drift motions it is common to approximate the magnitudes of the quadratic transfer functions by the steady drift forces at the same mean frequencies. This greatly simplifies the analysis of low-frequency motions. This is relatively useful in deep water, as indicated by the close agreement between the black and red curves in the lower plots. However, as the depth is decreased below 100m, this approximation is poor. .

Slowly-varying 2nd order Sway Force on FPSO

Solid lines – complete, Dashed lines -- approximate

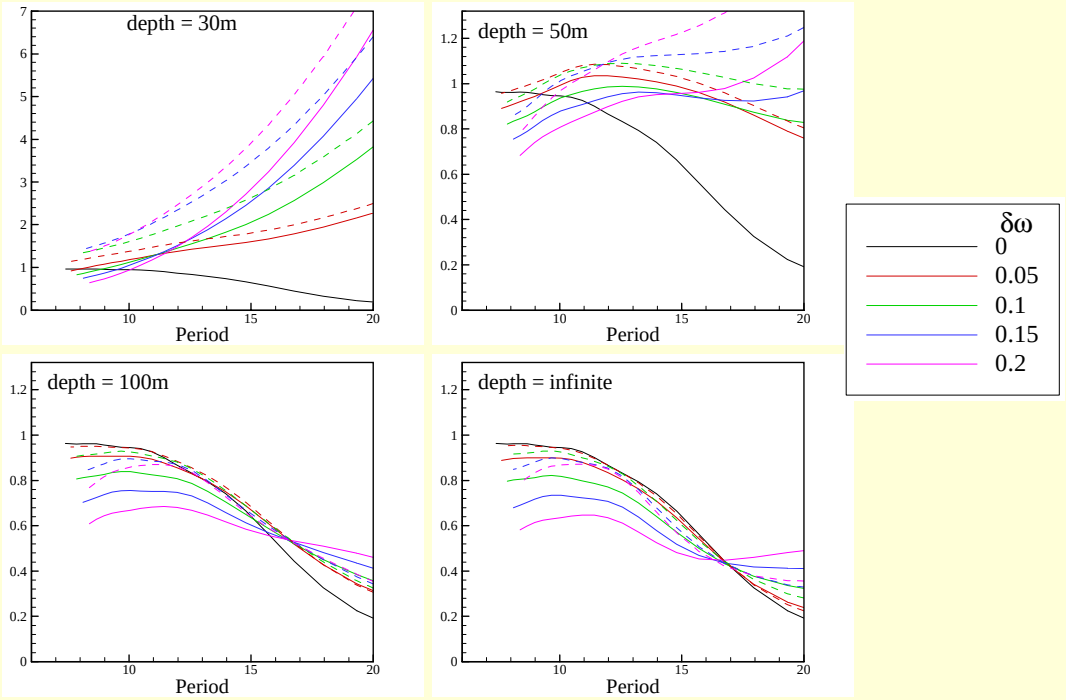

Fortunately, the most important component of the second-order potential in shallow water is associated with the incident waves, as shown here. The solid lines are the complete solution as in the previous slide. The dashed curves include the effects of the second-order incident wave potential, and its diffraction by the vessel, but not the more complicated potential resulting from the second-order forcing on the free surface. This gives much better results in shallow water, compared to the approximation based on the steady drift forces.

VISCOR (Viscous Correction)
A Navier-Stokes Extension to Potential Solutions
Tim Kendon, Imperial College, UK

- Total flow velocity: $v = \nabla\phi + v_R$
- Given potential input: $\nabla\phi$
- Solve for residual component: v_R

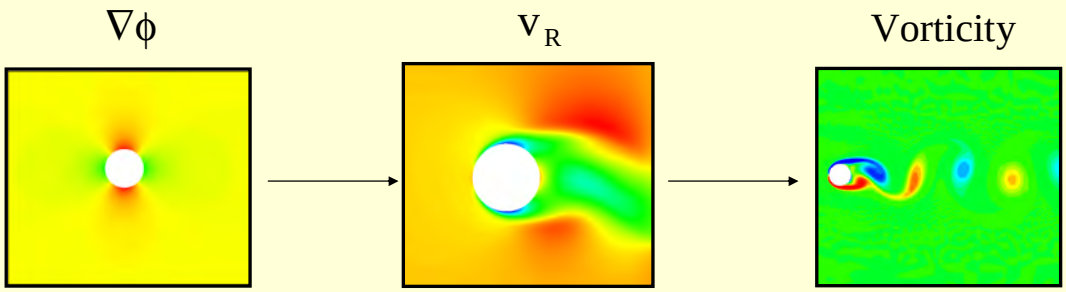

Finally I want to show some very recent results obtained at Imperial College, where a Navier-Stokes solver has been used as a post-processor. First the irrotational velocity field is computed at a large number of points near the body, using the higher-order panel method and including the linear free-surface effects. Then an additional rotational field is computed within this local domain using a Navier-Stokes solver,. This provides a rational procedure to account for important viscous effects such as roll damping.

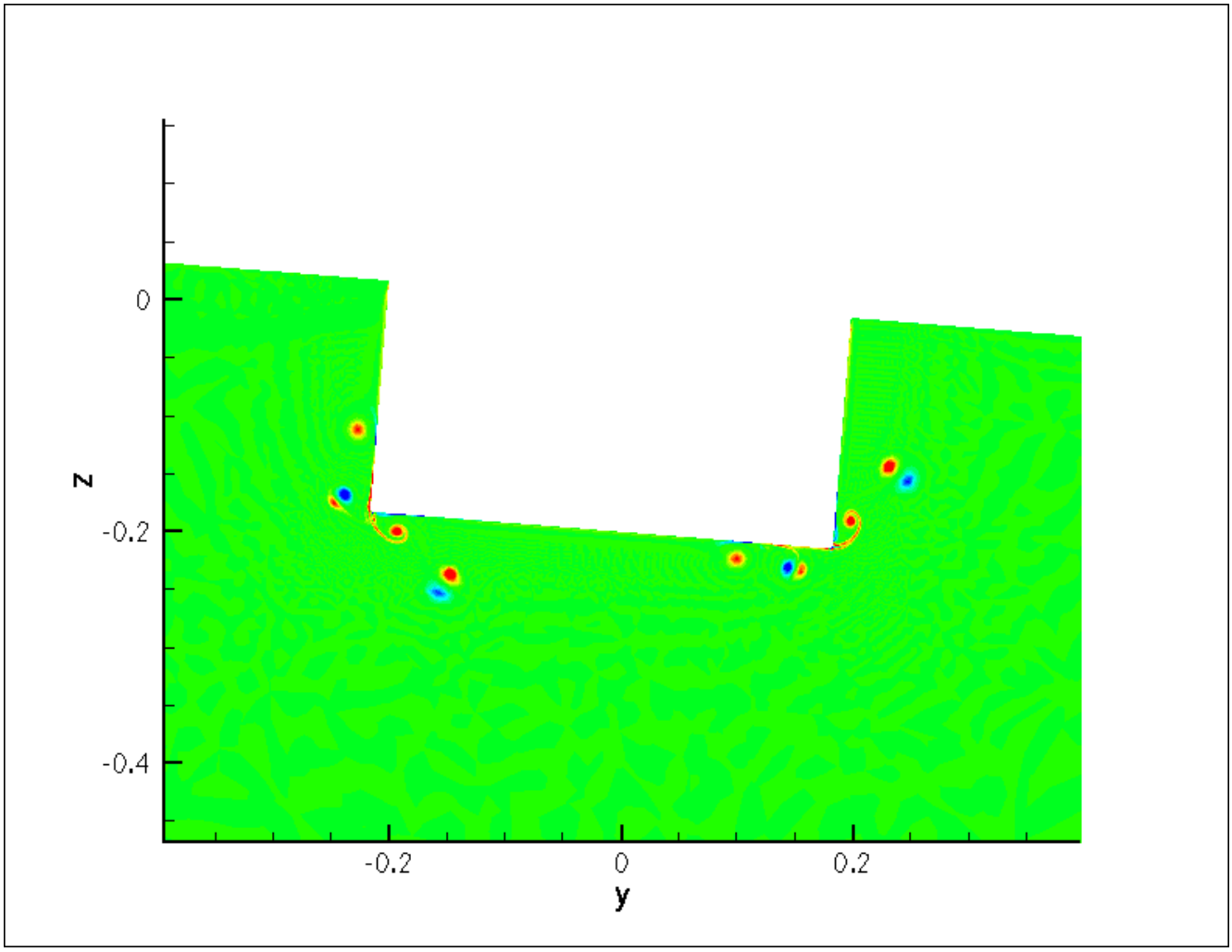

This is a cross-section of a rolling rectangular barge, showing the computational domain for the rotational flow and concentrated regions of shed vorticity.

Moments in plane for B/T=2, freq = 0.67Hz

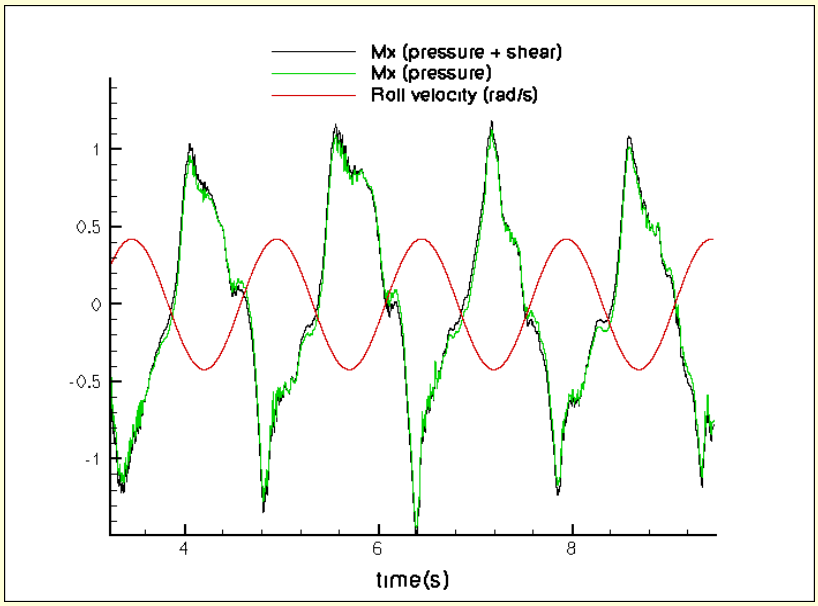

At a more quantitative level, this slide shows the time history of the roll moment, which attains its extreme values practically in phase with the maxima of the roll velocity. The roll moment is almost entirely due to the normal pressure, as opposed to the shear stress.

Roll Damping Coefficient against frequency (left;Vugts) and against roll amplitude (right;BMT)

Re = 5 times too small in both cases

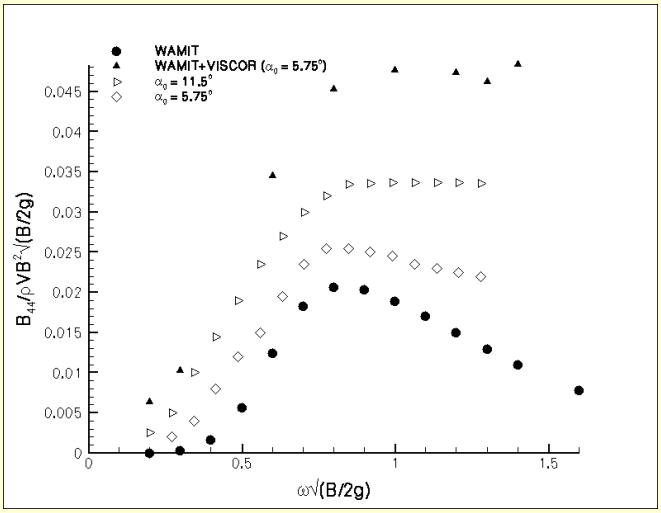

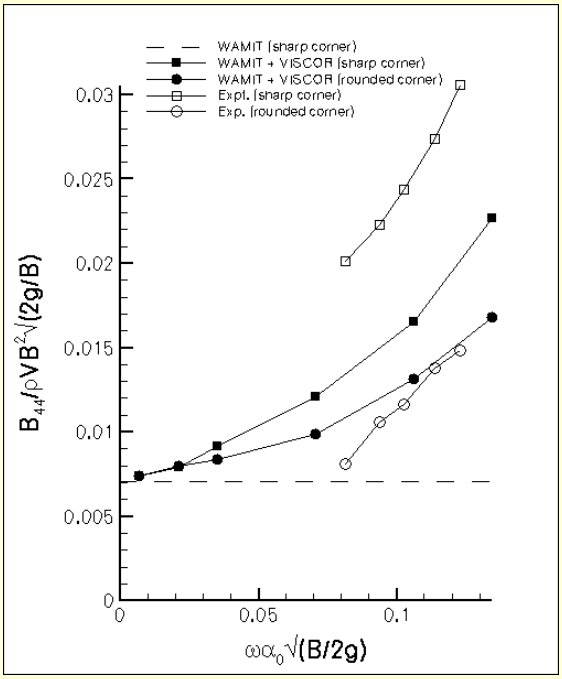

This slide compares computed values of the roll damping coefficient with two sets of experiments, and the results are qualitatively reasonable, but two caveats should be noted. First, the Reynolds number is about 5 times smaller in the computations as compared to the experiments, and secondly, while the potential-flow computations are fully three-dimensional, the viscous solution is two-dimensional.

I am indebted to Tim Kendon, a doctoral student working at Imperial College, for making these results available to show here. Additional information is available from his web page: http://www.ae.ic.ac.uk/staff/sherwin/html/tim_free.html

Conclusions

- There has been tremendous progress in the computation of wave loads (in ~40 years!)
- Advances in (a) theoretical methods,
  (b) computational resources (hardware), and
  (c) computational methods (software)
- Big challenges remain (nonlinear and viscous effects, complex structures, unique applications)

Further information:

- www.wamit.com → Publications

- "Computation of wave effects using the panel method," by C.-H. Lee and J. N. Newman, to be published in *Numerical Modeling in Fluid-Structure Interaction,* Edited by Subrata Chakrabarti, WIT Press, 2004

Note on the geometry of projection

Chang-Ho Lee

This note is concerned in finding appropriate geometric parameter such as derivatives and Jacobian on a region, made by the projection of a part of body surface, on the tangent plane .

Equation of a plane, $\mathbf{P}$, which passes $\mathbf{x}_o$ and perpendicular to $\mathbf{n}_o$ is

$$\mathbf{n}_o \cdot \mathbf{x} = \mathbf{n_o} \cdot \mathbf{x_o} = p$$

When $\mathbf{n}_o$ is the normal vector at $\mathbf{x}_o$ on a surface $\mathbf{S}$, the plane is tangent to $\mathbf{S}$ at $\mathbf{x}_o$.

The derivative at $\mathbf{x}_o$ of normal dipole distributed on $\mathbf{S}$ is too singular even after trianglarization. Thus the difference in the derivatives due to the normal dipoles on $\mathbf{S}$ and $\mathbf{P}$ are evaluated first and that of on $\mathbf{P}$ is added. The latter is evaluated from the line integral along the edge of the plane by applying Biot-Savart law. The extent of $\mathbf{P}$ can be calculated using the rate of change of $\mathbf{x}$, $\mathbf{x_u} = d\mathbf{x}/d\mathbf{u}$ at $\mathbf{x}_o$ on $\mathbf{S}$. But this may not be accurate when $\mathbf{x_u}$ change rapidly.

More general way to introduce the extent of the region on the tangent plane may be to use the projection of $\mathbf{S}$ on to $\mathbf{P}$. Let the point on $\mathbf{S}$ is $\mathbf{x}'$. A line $\mathbf{L}$ passes the point $\mathbf{x}'$ and perpenticular to $\mathbf{P}$, is

$$\mathbf{x} = \mathbf{x}' + t\mathbf{n}_o$$

where t is a scalar function of $\mathbf{u}$. If $\mathbf{L}$ intersects $\mathbf{P}$,

$$p = \mathbf{n}_o \cdot \mathbf{x} = \mathbf{n}_o \cdot (\mathbf{x}' + t\mathbf{n}_o)$$

from which we have

$$t = p - \mathbf{n}_o \cdot \mathbf{x}'.$$

Thus the position of the projected point and parametric derivatives on it can be evaluated from the following relation.

$$\mathbf{x} = \mathbf{x}' + (p - \mathbf{n}_o \cdot \mathbf{x}')\mathbf{n_o}$$

$$\mathbf{x}_u = \mathbf{x'}_u - (\mathbf{n}_o \cdot \mathbf{x'}_u)\mathbf{n}_o$$

$$\mathbf{x}_v = \mathbf{x'}_v - (\mathbf{n}_o \cdot \mathbf{x'}_v)\mathbf{n}_o$$

and the corresponding Jacobian is given in the form

$$J(\mathbf{x}) = |\mathbf{x}_u \times \mathbf{x}_v| = |J(\mathbf{x}_o) - (\mathbf{n}_o \cdot \mathbf{x'}_u)(\mathbf{n}_o \times \mathbf{x'}_v) + (\mathbf{n}_o \cdot \mathbf{x'}_v)(\mathbf{n}_o \times \mathbf{x'}_u)|$$

Since

$$\iint \nabla_{\mathbf{x}_o} \mathbf{n}_{\mathbf{x}} \cdot \nabla_{\mathbf{x}} (\frac{1}{R}) dS_{\mathbf{x}} = \int \mathbf{t}_{\mathbf{x}} \times \nabla_{\mathbf{x}_o} (\frac{1}{R}) dl_{\mathbf{x}},$$

the integral over $\mathbf{P}$ is evaluated as the line integral along the projected boundary. Here $\mathbf{t}$ is the vector along the boundary. The line integral is evaluated by successive subdivision.